Selective and enhanced fluorescence by biocompatible nanocoatings to monitor G-protein coupled receptor dynamics

***

Selektive und verstärkte Fluoreszenz durch biokompatible Nanobeschichtungen zur Untersuchung von G-protein gekoppelten Rezeptoren und ihrer Dynamik

Doctoral thesis for a doctoral degree
at the Graduate School of Life Sciences
Julius-Maximilians-Universität Würzburg,
Section Biomedicine

submitted by

Benjamin Schreiber

from Pirna, Germany

Würzburg 2018

Submitted on: 24.07.2018

Members of the *Promotionskomitee*:

Chairperson:	Prof. Dr. Peter Jakob
Primary Supervisor:	Prof. Dr. Katrin G. Heinze
Supervisor (Second):	Dr. Martin Kamp
Supervisor (Third):	Prof. Davide Calebiro (PhD)
Supervisor (Fourth):	Prof. Dr. Carsten Hoffmann

Date of Public Defence: 6.12.2018

Date of Receipt of Certificates:

Table of Contents

Summary

Fluorescence microscopy has become one of the most important techniques for the imaging of biological cells and tissue, since the technique allows for selective labeling with fluorescent molecules and is highly suitable for low-light applications down to the single molecule regime. The methodological requirements are well-defined for studying membrane receptors within a highly localized nanometer-thin membrane. For example, G-protein-coupled receptors (GPCRs) are an extensively studied class of membrane receptors that represent one of the most important pharmaceutical targets. Ligand binding and GPCR activation dynamics are suspected to take place at the millisecond scale and may even be far faster. Thus, techniques that are fast, selective, and live-cell compatible are required to monitor GPCR dynamics. Fluorescence resonance energy transfer (FRET) and total internal reflection fluorescence microscopy (TIRF-M) are methods of choice to monitor the dynamics of GPCRs selectively within the cell membrane.

Despite the remarkable success of these modalities, there are limitations. Most importantly, inhomogeneous illumination can induce imaging artifacts, rendering spectroscopic evaluation difficult. Background signal due to scattering processes or imperfect labeling can hamper the signal-to-noise, thus limiting image contrast and acquisition speed. Careful consideration of the internal physiology is required for FRET sensor design, so that ligand binding and cell compatibility are well-preserved despite the fluorescence labeling procedures. This limitation of labeling positions leads to very low signal changes in FRET-based GPCR analysis. In addition, microscopy of these systems becomes even more challenging in single molecule or low-light applications where the accuracy and temporal resolution may become dramatically low. Fluorescent labels should therefore be brighter, protected from photobleaching, and as small as possible to avoid interference with the binding kinetics. The development of new fluorescent molecules and labeling methods is an ongoing process. However, a complete characterization of new labels and sensors takes time. So far, the perfect dye system for GPCR studies has not been found, even though there is high demand.

Thus, this thesis explores and applies a different approach based on improved illumination schemes for TIRF-M as well as metal-coated coverslips to enhance fluorescence and FRET efficiency. First, it is demonstrated that a 360° illumination scheme reduces typical TIRF artifacts and produces a much more homogenously illuminated field of view. Second, membrane imaging and FRET spectroscopy are improved by metal coatings that are used to modulate the fluorescent properties of common fluorescent dyes. Computer simulation methods are used to understand the underlying photophysics and to design the coatings. Third, this thesis explores the operational regime and limitations of plasmonic approaches with high sectioning capabilities. The findings are summarized by three publications that are presented in the results section of this work. In addition, the theory of fluorescence and FRET is explained, with particular attention to its emission modulations in the vicinity of metal-dielectric layers. Details of the instrumentation, computer simulations, and cell culture are described in the method section. The work concludes with a discussion of the findings within the framework of recent technological developments as well as perspectives and suggestions for future approaches complete the presented work.

Zusammenfassung

Die Fluoreszenzmikroskopie ist zu einer der wichtigsten Techniken für die Bildgebung biologischer Zellen und Gewebe geworden, da die Technik eine selektive Markierung mit fluoreszierenden Molekülen ermöglicht und sich hervorragend für Anwendungen bei schwachem Licht bis hin zum Einzelmolekül-Regime eignet. Die methodischen Anforderungen sind gut definiert, um Membranrezeptoren innerhalb einer stark lokalisierten nanometerdünnen Membran zu untersuchen. Zum Beispiel sind G-Protein-gekoppelte Rezeptoren (GPCRs) eine ausführlich untersuchte Klasse von Membranrezeptoren, weil diese wichtige pharmazeutische Ziele darstellen. Es wird vermutet, dass die Ligandenbindungs- und GPCR-Aktivierungsdynamiken im Millisekundenbereich stattfinden und sogar viel schneller sein können. Daher sind Techniken erforderlich, die schnell, selektiv und lebend-Zell kompatibel sind, um die GPCR-Dynamik zu aufzunehmen. Fluoreszenzresonanzenergietransfer (FRET) und internale Totalreflexions-Fluoreszenzmikroskopie (TIRF-M) sind Methoden der Wahl, um die Dynamik von GPCRs selektiv innerhalb der Zellmembran zu untersuchen.

Trotz des bemerkenswerten Erfolgs dieser Modalitäten gibt es Einschränkungen. Am wichtigsten ist, dass eine inhomogene Beleuchtung Artefakte erzeugen kann, welche die spektroskopische Auswertung erschweren. Hintergrundsignale aufgrund von Streuprozessen oder unvollständiger Markierung können das Signal-Rausch-Verhältnis beeinträchtigen und somit den Bildkontrast und die Erfassungsgeschwindigkeit begrenzen. Eine sorgfältige Berücksichtigung der internen Physiologie ist für das Design der FRET-Sensoren ist erforderlich, so dass die Ligandenbindung und die Zellkompatibilität trotz der Fluoreszenzmarkierungsverfahren nicht gestört werden. Diese Einschränkung der Markierungspositionen führt zu sehr geringen Signalkontrast in der FRET-basierten GPCR-Analyse. Darüber hinaus wird die Mikroskopie dieser Systeme bei Einzelmolekül- oder Schwachlichtanwendungen, bei denen die Genauigkeit und die zeitliche Auflösung dramatisch niedrig werden können, noch schwieriger. Fluoreszierende Marker sollten daher heller, vor Photobleichung geschützt und so klein wie möglich sein, um Störungen mit der Rezeptorkinetik zu vermeiden. Die Entwicklung neuer fluoreszierender Moleküle und Markierungsmethoden ist ein fortlaufender Prozess. Eine vollständige Charakterisierung neuer Marker und Sensoren benötigt jedoch Zeit. Bis jetzt wurde das perfekte Farbstoffsystem für GPCR-Studien noch nicht gefunden, auch wenn es eine hohe Nachfrage dafür gibt.

Daher wird ein anderer Ansatz auf der Grundlage verbesserter Beleuchtungsschemata für TIRF-M sowie metallbeschichtete Deckgläser zur Verbesserung der Fluoreszenz- und FRET-Effizienz untersucht. Zunächst wird gezeigt, dass ein 360 ° Beleuchtung typische TIRF-Artefakte reduziert und ein wesentlich homogeneres Bildausleuchtung erzeugt. Zweitens wurde durch die Modulation der Fluoreszenzeigenschaften gängiger Fluoreszenzfarbstoffe die Membranbildgebung und FRET-Spektroskopie verbessert. Computersimulationsmethoden werden verwendet, um die zugrundeliegende Photophysik zu verstehen und zielgerichtet Beschichtungen zu entwerfen. Drittens wurden das operationelle Regime und die Grenzen von plasmonischen Ansätzen mit noch höheren Signalselektiverung untersucht. Die Ergebnisse sind in drei Publikationen zusammengefasst, die im Ergebnisteil dieser Arbeit vorgestellt werden. Darüber hinaus wird die Theorie der Fluoreszenz und des FRET unter besonderer Berücksichtigung ihrer Emissionsmodulationen in der Nähe von Metall-Dielektrikum-Schichten erläutert. Details der Instrumentierung, Computersimulationen und Zellkultur werden im Abschnitt Methoden beschrieben. Die Arbeit schließt mit einer Diskussion der Ergebnisse im Rahmen der jüngsten technologischen Entwicklungen sowie mit Perspektiven und Vorschlägen für zukünftige Ansätze, die die vorliegende Arbeit abrunden.

1 Introduction

1.1 Motivation and start of the art

The plasma membrane of a cell acts as a gatekeeper. The membrane controls the homeostasis of substances inside the cell by controlling the permissivity of certain substances and promotes interactions between cells through hundreds of different cell-surface receptor classes (membrane and transmembrane receptors) [1, 2]. An essential receptor class is represented by the G-protein-coupled receptors (GPCRs), which are the largest group of cell membrane receptors with more than a thousand different members. Specially engineered ligands allow selective control of GPCR-induced processes, which creates possibilities for curing or alleviating diseases. Today, around 30% of all drugs available on the market are pharmaceutical ligands that bind to GPCRs [3]. Thus, it is obvious that understanding GPCR mechanisms has an enormous impact on biomedical and clinical research.

The activation of GPCR is highly complex and is not yet fully understood. In a nutshell, upon ligand binding, the receptor is dynamically present in an active or an inactive state. However, it should be noted that it is not fully clear whether the receptor dynamically switches between two distinct states or if there are more structural intermediate states [4, 5]. Depending on the specific GPCR, different receptor activation times have been reported, ranging from 10 milliseconds to several hundreds of milliseconds [6], with typical dynamics in the range of 30 to 80 milliseconds [6].

Ligand-induced receptor activation can launch two different types of signaling cascades: G-protein-independent signaling and G-protein-dependent signaling [7]. Both signaling types are cyclic, meaning that signaling cascade has a starting phase, a signaling step, and a recycling step at the end that restores the initial state. The signaling cascades are very complex, and many different proteins in different chemical states are involved. For example, in a specific step of a G protein-independent signaling, the activated GPCR will induce internalization into the cell with a ball shaped vesicle which is formed using a part of the cell membrane [8, 9]. Through this process, which is called endocytosis, the cell absorbs the nutrition required by it and also regulates the receptor density on the cell membrane to control the ligand sensitivity of the cell [10]. The second signaling process type is G protein-dependent signaling. Here, the activated receptor activates a heterotrimeric G-protein which contains the subunits termed α, β and γ [7]. The activated G-protein dissociates into G_α and $G_{\beta\gamma}$ subunits. The $G_{\beta\gamma}$ subunit activates or inhibits downstream effector proteins, and it triggers membrane-bound ion channels, for example [11, 12]. There are different types of G_α subunits, which can typically be sorted into four main G_α families [12]. G_α subunits typically activate diverse types of enzymes like adenylyl cyclase and phosphodiesterase, which have key regulatory roles in cells [7, 13]. Since GPCR signaling is a cyclic process, the G protein reassembles after the signaling cascade [7].

Fluorescence-based microscopy and spectroscopy are commonly used approaches to render GPCRs and their dynamics observable [14]. A GPCR can be selectively labeled with the use of a fluorescent molecule [15]. The emission of the fluorescent marker makes the labeled GPCRs observable. The concept of fluorescence relies on the emission of light by the fluorophore in a different spectral region from the light that has been used to excite the molecule. This allows the spectral splitting of excitation and emission light, and therefore allows the detection of the marked GPCRs. Using different fluorescent labels for different GPCRs or GPCR parts, make the interaction dynamics visible. Such interactions can be between different GPCRs or structural changes in a GPCR that were induced by a ligand [16-18].

The fluorescence of a donor molecule excites an acceptor molecule by fluorescence resonance energy transfer (FRET). This only takes place if the distance between donor and acceptor is very small, usually smaller than 10 nanometers [19, 20]. A typical GPCR-FRET sensor contains donor and acceptor

molecules located at a nanometer distance on the protein. Fluorescence resonance energy transfer has been proven to be a suitable tool to study ligand-specific binding dynamics and ligand-induced structural changes in GPCRs (e.g., see Hoffmann et al. [21-24]).

Fluorescence imaging is highly suitable for the observation of the cell membrane [25, 26]. Epifluorescence-based methods are used for high signal collection and good signal-to-noise ratio [25, 26]. In epifluorescence, excitation and fluorescence pass the same objective lens, and imaging is usually performed through a microscopy coverslip that has the cell sample on it. Imaging of the relatively flat basal cell membrane of the adherent cells that are attached to the coverslip is mostly straight forward.

Suitable fluorescence techniques are often divided into confocal-based versus camera-based techniques. Confocal laser scanning microscopy (CLSM) allows imaging of a whole cell by scanning with a focused laser beam [27]. The collected fluorescence is spatially filtered by a pinhole before detection. This ensures that only the emission originating from the focal spot is recorded. Confocal imaging allows for high lateral and axial resolution, especially if high numerical aperture (NA) objective lenses are used. The so-called Abbe limit defines the maximal resolution power, which is proportional to $\lambda(2NA)^{-1}$ for the lateral and to $2\lambda(NA)^{-2}$ for the axial case. Form the Abbe-limit follows typical spatial and axial resolutions around 200 nm and 600 nm [28], respectively. The lateral signal distribution provides information on molecular distribution and oligomerization in the cell membrane, even if single molecules cannot be distinguished [29].

One way to reduce the observation volume and thus achieve super-resolution is stimulated emission and depletion (STED) [30]. This technique relies on the principle of blocking excited fluorescence by a donut-shaped depletion laser focus. Only fluorescence located in the hollowed laser spot remains bright and is detected. A confocal imaging that is far below standard confocal imaging can thereby be achieved [30, 31]. Unfortunately, STED has disadvantages due to the high laser power that is required [32]. Both, CLSM and STED can also be used in combination with fluorescence correlation spectroscopy (FCS) to study diffusion dynamics of GPCRs on a nanometer scale [33, 34]. The FCS method involves a laser spot being focused and “parked” on the cell membrane. Fluorescently marked GPCRs diffuse through the laser focus and fast point detectors collect the emitted photons. It is possible to observe GPCR diffusion and even faster processes like the dynamics of conformational changes upon activation through autocorrelation of the recorded fluorescence traces and knowledge of excitation volume [25, 35]. Since the laser scanning is time consuming compared to camera-based approaches this confocal-based techniques are not suitable for following single GPCRs over the cell membrane.

With camera-based microscopy techniques, the complete cell membrane is recorded at once, while the whole field of view (FOV) is simultaneously illuminated. If the signal is sufficiently strong, camera-based fluorescence imaging approaches enable high acquisition speeds, which will finally allow for the following of lateral GPCR movements. Total internal reflection fluorescence microscopy (TIRF-M) is a variation on wide-field imaging using overcritical oblique angle illumination [36]. With a TIRF illumination, only a nanometer-thick area above the coverslip is illuminated, leading to a very high signal-to-noise (SNR) ratio in basal cell membrane imaging [37]. Due to this membrane-selective imaging, low background, and fast camera recording, TIRF-M has become a key technique to study the dynamics of GPCRs on cell membranes. Important findings on GPCR diffusion dynamics and organization on the cell membrane have been found using TIRF-M (e.g., see Calebiro et al. [38, 39]). In addition, TIRF-M can be combined with super-resolution approaches like single molecule localization microscopy (SMLM), which allows for nanometer-precise investigation of membrane receptor localizations [40-43].

The combination of TIRF-M and FRET enables the study of various aspects of cell receptor activation, their ligand-induced organization, and structural changes [44, 45]. Both of these methods are well-established and are essential for GPCR research. Unfortunately, both techniques suffer from limitations and difficulties. In TIRF-M, an unevenly illuminated FOV may induce imaging artifacts, leading to a misinterpretation of the GPCR activation and lateral organization [46, 47]. In addition, changes of FRET efficiencies are often small and limit the precision in monitoring conformational changes of GPCRs [48, 49].

1.2 Aims of this study

The overall goal of this study is to provide a "toolbox" and "physics tweaks" to allow faster and more precise live-cell microscopy for enhanced fluorescence cell membrane imaging and spectroscopy. Studies of GPCRs dynamics in live-cells are particularly technically challenging. Three different approaches were taken to reach this goal.

The first approach is to improve the TIRF imaging, particularly the illumination field as it this is often the Achilles' heel in TIRF-M. One bottleneck is the commonly used one-sided laser illumination [46, 47]. Annular spinning-spot and ring illuminated TIRF-M have previously been demonstrated to be able to reduce such artifacts [46, 47]. Along these lines, it was clear that a flat-top illuminated image plane would be one suitable solution as it allows for quantitative analysis across the whole FOV. Following this idea, I decided to work on a new illumination scheme for TIRF-M that would provide such flat-top schemes to finally provide the essential prerequisite for improved TIRF-M.

The second approach is to increase the SNR in TIRF-M. An unwanted and out-of-focus fluorescence background reduces the SNR. A low SNR prevents fast acquisition speeds, since the collection of a sufficient signal for evaluable records is time-consuming. With this slow recording, it is hard to temporally resolve fast dynamics on the cell membrane. One way to increase the SNR in TIRF-M is to reduce fluorescence background. This background may be out-of-focus because of imperfect labeling or scattering effects inside the cell, which generate high fluorescence signals that are not excited by the evanescent TIRF field. Noble metal "plasmonic" nanocoated coverslips use surface plasmon-coupled emission (SPCE, [50]) to act as axial-selective fluorescence mediators and block the detection of out-of-focus fluorescence [51, 52]. Based on this idea, I decided to use plasmonic nanocoated microscopy coverslips for active suppression of unwanted fluorescence. I implemented plasmonic nanocoating into a home-built TIRF-M and characterized the SPCE effects, with the aim of high SNR membrane imaging in high fluorescent background environments.

The third approach is to enhance FRET spectroscopy to study GPCR activation dynamics in intact cell membranes. FRET sensors that are attached on GPCRs are essential for testing new pharmacological compounds, since ligand-induced GPCR activation processes can be monitored with FRET [21-24]. Unfortunately, many well-established FRET sensors only indicate low signal changes between inactive and active states. A recent study demonstrates enhanced FRET along fluorescently labeled DNA oligomers in high photonic environments that are generated by plasmonic nanostructures [53]. To increase the efficiency of GPCR FRET sensors in living cells, I decided to use plasmonic nanocoatings. Further, I investigated the beneficial effects of enhanced FRET efficiencies to study ligand-induced receptor activation dynamics.

2 Theory

2.1 Fluorescence and fluorescence resonance energy transfer (FRET)

Fluorescence is the phenomenon of electromagnetic radiation of a material after photon absorption. In this section, I introduce a basic photophysical concept of fluorescence and fluorescence resonance energy transfer (FRET) [54] between two fluorescent dyes.

Two-state system

A suitable model for understanding the concept of fluorescence for a molecule is the two-state quantum system [55]. The Jablonski diagram in figure 2-1(a) describes such a two-state system [56]. By light excitation, an electron from the ground state can absorb the photon energy, raising the electron to an excited state. Excited and ground state are broadened by vibration states. In case of a fluorescent system, the excited electron remains in the excited state band and relaxes to lower energy vibrational levels. After remaining inside the excited state (typical few ns for fluorescent molecules), the electron falls from the excited state to a lower energy level by radiation emission [56]. The lower energy level is (most likely) located in the electronic band of the ground state. The molecule is now unexcited and ready for the next excitation and emission process. The "golden rule" of quantum mechanics [57] describes the transition rates of electrons between two electronic states. The transition probability is maximized if the difference between the energy levels of the involved states matches the (excitation or emission) photon energy. Those effects, both the electron excitation and the fluorescence emission probabilities are dependent on the density distribution of the electronic states of the molecule. From these transition probabilities arise the emission and absorption spectra. An example of emission and excitation spectra of a fluorescent Alexa 488 [58] dye is shown in figure 2-1(b).

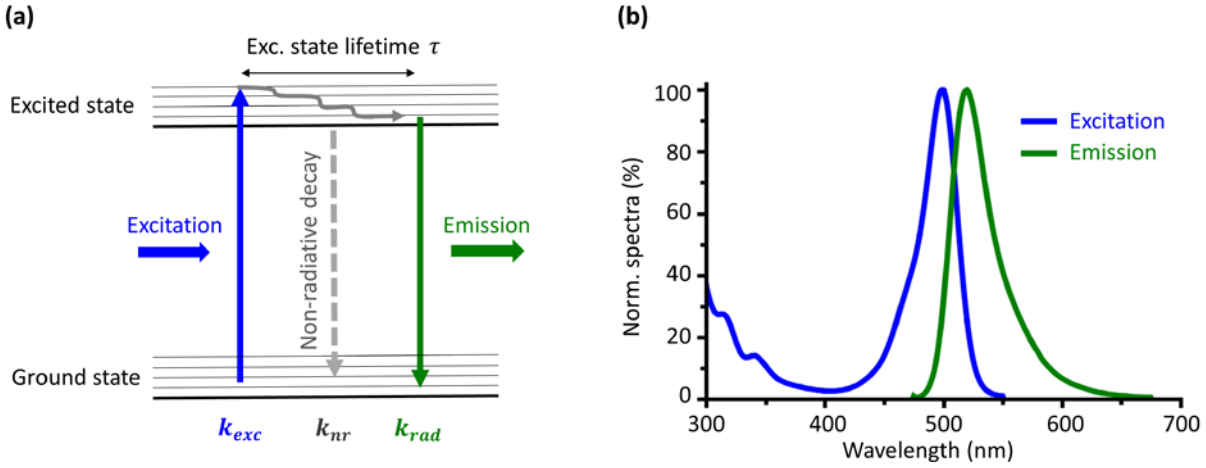

Figure 2-1. (a) Illustration of excitation and emission process of a fluorescent molecule. Excitation k_{exc}, radiative k_{rad}, non-radiate k_{nr} rates and the excitation state lifetime τ are indicated. (b) Excitation and emission spectra of a fluorescent Alexa 488 molecule [58].

The fluorescence lifetime describes the mean time that an electron keeps in the excited state before it rejects to the ground stage. The time decay of the number of electrons in the excited state $N_{exc}(t)$ follows an exponential law with the fluorescence lifetime τ as decay constant.

$$N_{exc}(t) = N_{exc}(0)e^{-t/\tau} \quad \text{(Eq. 2-1)}$$

All processes that depopulate the excited state reduce the lifetime. The sum of all deexcitation rates is the total rate k_{tot}.

$$\tau = \frac{1}{k_{tot}} \quad \text{(Eq. 2-2)}$$

For a single two-state system the total rate is given by the sum of the radiative and non-radiative rates $k_{tot} = k_{rad} + k_{nr}$. The quantum yield QY is defined as the ratio of the number of photons emitted to the number absorbed. Since both numbers of photons are respectively connected with k_{rad} and k_{tot} the quantum yield QY is expressible by the quotient of both [56].

$$QY = \frac{k_{rad}}{k_{tot}} = k_{rad}\tau \quad \text{(Eq. 2-3)}$$

The point dipole emitter

Since the electronic transition of the fluorescent system is introduced, we will now focus on the emission of the fluorophore. The radiation of the molecule is well described by a classic oscillating dipole [59]. A light emitting dipole is a charge distribution q and oscillates with a frequency ω along a vector $\vec{a}$ which can be summarized in the dipole moment $\vec{p}_d = q\vec{a}e^{-i\omega t}$. The electromagnetic field $\vec{E}_d(r)$ of the dipole at distance r is given by a Hertzian point dipole emitter [59].

$$\vec{E}_d(\vec{r}) = \left[\left(-\frac{k^2}{r} - \frac{3ik}{r^2} + \frac{3}{r^3}\right)\vec{e}_r(\vec{e}_r \cdot \vec{p}_d) + \left(\frac{k^2}{r} + \frac{ik}{r^2} - \frac{1}{r^3}\right)\vec{p}_d\right]\frac{e^{ikr}}{n^2} \quad \text{(Eq. 2-4)}$$

Here $k = 2\pi/\lambda = \omega/c$ is the free space angular wavenumber for the oscillation frequency ω (or wavelength λ) of the dipole emitter, n is the refractive index (RI) of the medium, c the vacuum speed of light and $\vec{e}_r$ is a unit vector pointing from the dipole towards the position r. We can split this equation to two important cases.

First, the far field approximation describes the light propagating over distances longer than the emission wavelength ($kr > 1$).

$$\vec{E}_d(\vec{r}) \propto \frac{e^{-ikr}}{r}\sin\varphi\,\vec{e}_\varphi \quad \text{(Eq. 2-5)}$$

$$I_d(\vec{r}) \propto \left|\vec{E}_d(\vec{r})\right|^2 \propto \frac{\sin^2\varphi}{r^2} \quad \text{(Eq. 2-6)}$$

The far field radiation intensity has a dumbbell like shape ($\propto \sin^2\varphi$) where the maximum propagation is directed perpendicular to the dipole orientation and the intensity emission intensity $I_d(r)$ decreases with r^{-2}. The behavior of far field radiation is shown in figure 2-2 (a,c). The dipole radiation power S_d (product of radiation rate k_d and photon energy E_{photon}) is given as [59]:

$$S_d = k_d E_{photon} = \frac{1}{3}p_d^2 k^4 cn \quad \text{(Eq. 2-7)}$$

Second, the near field approximation for the narrow regime around the dipole emitter ($kr \ll 1$) .

$$\vec{E}_d(\vec{r}) \approx [3\,\vec{e}_r(\vec{e}_r \cdot \vec{p}_d) + \vec{p}_d]\frac{e^{ikr}}{r^3 n^2} \qquad \text{(Eq. 2-8)}$$

$$I_d(\vec{r}) \propto \left|\vec{E}_d(\vec{r})\right|^2 \propto r^{-6} \qquad \text{(Eq. 2-9)}$$

Since the dipole near field intensity falls rapidly with r^{-6}, the highest energy density is located in few nanometers around the dipole. The near field amplitude is shown by electric field simulations in figure 2-2(b,d).

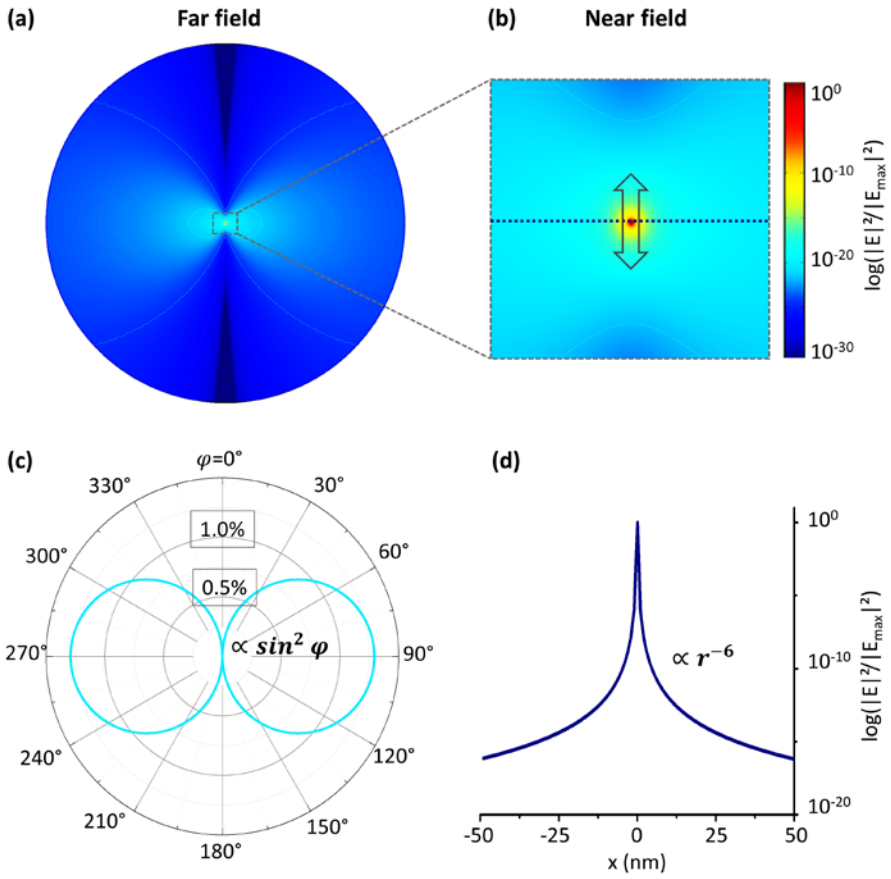

Figure 2-2. Electric field of a dipole emitter for different zoom ((a) sphere with 10µm radius and (b) a 100 nm square). An arrow indicates the dipole orientation. (c) Far field directivity shows a dumbbell like far field radiation pattern (shape $\propto sin^2\,\varphi$) with propagation perpendicular to the dipole orientation. The electric near field strength (d) extracted from (b) shows the highest values at the dipole position and drops laterally with $\propto r^{-6}$.

Fluorescence Resonance Energy Transfer (FRET)

Until now, we have discussed excitation and emission of a single fluorophore. In this work understanding the interactions of a fluorescent molecule with an interaction partner is a matter of particular interest. An interaction partner for our molecule is second fluorescent molecule. If several criteria are met, energy from a donor molecule can be transferred to an acceptor molecule. This energy transfer between a donor and acceptor molecule usually only takes place in molecules located less than 10 nm apart [60]. To understand FRET, we will start to place an acceptor molecule with the dipole moment $\vec{p}_A$ into the electric field of the acceptor molecule $\vec{E}_d(\vec{r})$. The excitation rate of the acceptor is thus directly given by the absorption of energy from the donor at the position $\vec{r}_A$ where the acceptor is placed [59].

$$k_{FRET} = 3\sigma_A \frac{nc}{8\pi}\frac{\lambda}{hc}\left|\vec{p}_A \vec{E}_d(\vec{r}_A)\right|^2 \qquad \text{(Eq. 2-10)}$$

Here σ_A is the absorbance of the acceptors and h the Planck constant. From above we know that the most energy density of the dipole is located few nanometers around the dipole in the near field. We can use the near field equation Eq. 2-8 and the relation of the dipole moment and the radiation rates Eq. 2-10 to describe FRET rates as follows:

$$k_{FRET} = \frac{3\sigma_A}{8\pi}\frac{\lambda}{hn^3}\frac{p_D^2}{r^6}\underbrace{\left|3(\vec{e}_r \cdot \hat{p}_A)(\vec{e}_r \cdot \hat{p}_D) - (\hat{p}_A \cdot \hat{p}_D)\right|}_{\kappa^2} = \frac{9}{8\pi}\frac{QY_D}{\tau_D}\frac{\sigma_A}{n^4 k^4 r^6}\kappa^2 \qquad \text{(Eq. 2-11)}$$

Here we have summarized a scalar term to κ^2 the dipole-dipole orientation factor. κ^2 includes scalar products of the normalized donor and acceptor orientation vectors ($\hat{p}_{A,D}$) and the unit vector ($\vec{e}_r$) [61]. Later, we will come back to the κ^2, because it is an important tuning factor to improve FRET [53, 62, 63].

As already described before, the absorbance of a molecule is dependent on its electronic structure, thus σ_A is wavelength dependent. The efficiency of the acceptors absorbing properties depends on the donor emission spectrum. The spectral match of donor emission $F_D(\lambda)$ and acceptor absorption $\varepsilon_A(\lambda)$ is given by the overlap integral J what also includes $k^{-4} = (\lambda/2\pi)^4$ term from equation Eq. 1-11 [59].

$$J = \frac{\int F_D(\lambda)\varepsilon_A(\lambda)\,\lambda^4 d\lambda}{(2\pi)^4 \int F_D(\lambda) d\lambda} \qquad \text{(Eq. 2-12)}$$

It has become the standard to summarize terms of k_{FRET} to the Förster radius R_0.

$$R_0^6 = \frac{9}{8\pi}\frac{QY_D}{n^4}\kappa^2 J \qquad \text{(Eq. 2-13)}$$

That gives us a compact form of the FRET rate k_{FRET}.

$$k_{FRET} = \frac{1}{\tau_D}\left(\frac{R_0}{r}\right)^6 \qquad \text{(Eq. 2-14)}$$

So far, we have derived the formula for energy transfer. The efficiency of energy transfer is given by the ratio of donor intensity with (I_{DA}) and without (I_D) the presence of the acceptor.

$$E_{FRET} = \frac{I_D - I_{DA}}{I_D} = 1 - \frac{I_{DA}}{I_D} \qquad \text{(Eq. 2-15)}$$

The intensities of fluorescent molecules are related to their quantum yields ($I \propto QY = k_{rad}/k_{tot}$). If the donor transfers energy to the acceptor, the donor intensity is reduced and follows $I_{DA} \propto k_r/(k_{rad} + k_{nr} + k_{FRET})$. Together with equation Eq. 2-14 we can give an expression for the FRET efficiency in the dependency of the Förster radius and dipole-dipole distance r.

.

$$E_{FRET} = \frac{R_0^6}{R_0^6 + r^6} = \frac{1}{1 + \left(\frac{r}{R_0}\right)^6} \qquad \text{(Eq. 2-16)}$$

The FRET follows a step like function what as shown in figure 2-3. The FRET efficiency E_{FRET} is 100% for $r < R_0$ and rapidly falls to 50% for $r = R_0$ and drops even further to 0% for $r > R_0$. The reason for this rapid intensity drop is that the donor near field decays with $\propto r^{-6}$ (see figure 2-2).

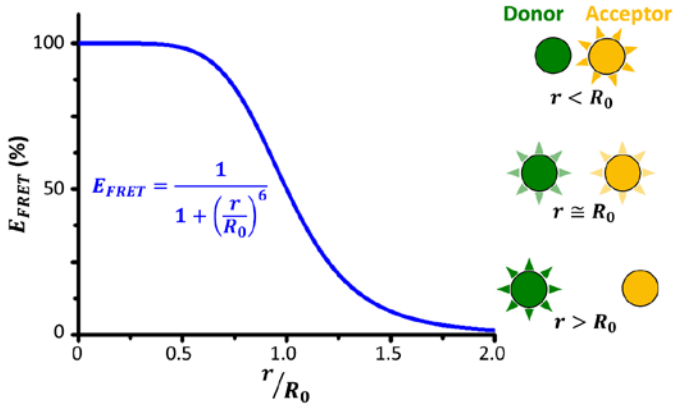

Figure 2-3. FRET efficiency E_{FRET} as a function of donor-acceptor distance r and FRET radius R_0. Depending on the efficiency of the energy transfer, different brightnesses of donor and acceptor molecules are observable.

The dipole-dipole orientation factor κ^2

Before we introduced the dipole-dipole orientation factor κ^2. Because of the direct connection of FRET radius and FRET rate (k_{FRET}; $R_0^6 \propto \kappa^2$) the dipole-dipole orientation factor has an impact for the FRET efficiency. We can express the scalar products of κ^2 with angular relationships [61].

$$k_{FRET},\ R_0^6 \propto \kappa^2 = (\cos\vartheta_T - 3\cos\vartheta_D \cos\vartheta_A)^2 \qquad \text{(Eq. 2-17)}$$

Here ϑ_D and $\vartheta_A$are the orientation angles of the donor and acceptor between the separation vector $\vec{r}_A$. The angle ϑ_T describes the dipole-dipole orientation to each other. A schematic illustration of the dipole-dipole orientation factor in dependence on the dipole directions is shown in figure 2-4(a). In practice using FRET in biological applications, sharp orientations of the molecules cannot be given or predicted. The reason for this is that the fluorescent markers have due to their link to the biological structurer of interest several degrees of freedom in their orientation [60]. Diffusion and vibration of the FRET molecules result in a distribution of the dipole-dipole orientation. Depending on κ^2, different orientations give a higher or lower contribution to the fluorescence energy transfer. Thus, we need to describe the dipole-dipole orientation factor as an average $\langle\kappa^2\rangle$ value of several κ^2 values. The formalism to calculate $\langle\kappa^2\rangle$ for different distributions is for example well described by Dale et al. [61].

The $\langle\kappa^2\rangle$ values for different donor and acceptor orientation distributions with ϑ_D, ϑ_A and ϑ_T as distribution mean values can be given in this form [61].

$$\langle\kappa^2\rangle = \frac{1}{3}(1-d_D) + \frac{1}{3}(1-d_A) + d_D(1-d_A)\cos^2\vartheta_D + d_A(1-d_D)\cos^2\vartheta_A + d_A d_D\,\kappa^2 \qquad (2\text{-}18)$$

Here are the normalized dynamic depolarization factors d_i for a given donor or acceptor orientation distribution $g_i(\theta)$ [61].

$$d_i = \frac{\int_0^\pi \left({}^3/_2\cos^2\theta - {}^1/_2\right)\sin\theta\, g_i(\theta)d\theta}{\int_0^\pi \sin\theta\, g_i(\theta)d\theta} \qquad (\text{Eq. } 2\text{-}19)$$

In figure 2-4(b) we show a scenario for average dipole-dipole orientation factors $\langle\kappa^2\rangle$ where the donor is randomly distributed, and the acceptor has a certain orientation distribution given by a Gaussian function (center ϑ_A and variance σ_{ϑ_A}). For sharp defined acceptor orientations, the $\langle\kappa^2\rangle$ value is depending on ϑ_A and has his maximum when acceptor and donor (mean) orientations are parallel to each other. Since high $\langle\kappa^2\rangle$ values are directly connected with high energy transfer between the molecules, these dipole-dipole orientations are preferable. In contrast, when the (mean) values of donor and acceptor orientations are perpendicular to each other, less often the energy transfer takes places what effectively reduce $\langle\kappa^2\rangle$. By broadening of the acceptor orientation distribution $\langle\kappa^2\rangle$ becomes more and more independent from ϑ_A and converges against 2/3.

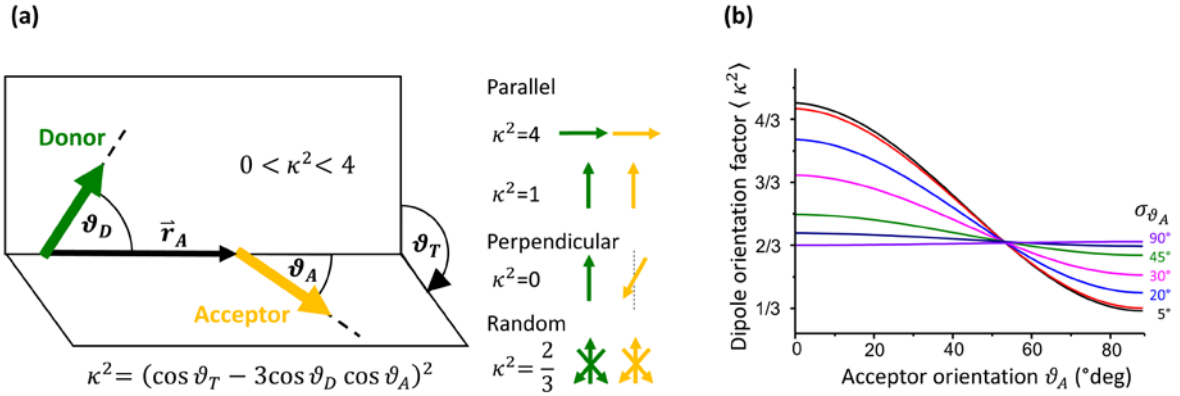

Figure 2-4. (a) Illustration of dipole-dipole orientation factor κ^2 in dependence of the donor ϑ_D, acceptor ϑ_A and separation ϑ_T angles. Special cases for dipole-dipole orientation are illustrated with corresponding κ^2 values. (b) Average dipole orientation factor $\langle\kappa^2\rangle$ of a system of a randomly orientated donor and an acceptor with mean orientation ϑ_A. The cases $\vartheta_A = 0°$ and $\vartheta_A = 90°$ display if the mean values of the dipole orientations are parallel or perpendicular. The acceptor orientation distribution is described by a Gaussian function with ϑ_A as center and σ_{ϑ_A} as variance. By increasing σ_{ϑ_A} the average dipole orientation factor $\langle\kappa^2\rangle$ becomes independent from ϑ_A and $\langle\kappa^2\rangle$ goes against 2/3, what describes the dipole-dipole orientation factor of a randomly orientated donor and acceptor pair.

2.2 Evanescent wave excitation at interfaces

In this section, we will introduce the phenomenon of evanescent wave excitation at interfaces. In particular, for the fluorescence-based imaging technique total internal reflection fluorescence microscopy (TIRF-M) allows axial-selective fluorescence excitation of a specimen attached to a coverslip. TIRF-M has become a very powerful technique to study membranes of cellular systems since TIRF-M yields high signal-to-noise (SNR) values [36, 64-66] . The high SNR values are generated because fluorescence background localized above the region of interest is not illuminated and thus will not be detected. The evanescent waves are generated by an overcritical oblique angle illumination at a refractive index (RI) mismatched interface. For TIRF-M this mismatch is realized by the refractive indexes of the coverslip and the specimen. By modification of the interface with a plasmonic noble metal coating, evanescent waves can be produced with few magnitudes higher intensities compared to the illumination intensity [66-68]. This field amplifying properties of plasmonic nanostructures are particularly interesting where high excitation intensities or strong local sectioning are beneficial.

We will introduce both evanescent phenomena in this section by comparing their physical similarities and differences. We start with dielectric interfaces.

Evanescent waves at dielectric interfaces

An evanescent electric field distribution perpendicular to a dielectric interface is observed by total internal reflection (TIR). We consider an interface built up from two dielectric materials with refractive indices n_1 and n_2, where $n_2 > n_1$. We illuminate the interface with a collimated beam under an oblique angle ϑ coming from the material with n_2, as depicted in figure 2-5. The beam, which passes from a material n_2 in a material n_1 is refracted by Snell`s law [37]. By increasing the illumination angle, ϑ pass a critical angle $\vartheta_{crit} = \sin^{-1}(n_1/n_2)$. For $\vartheta > \vartheta_{crit}$, the incoming light reflects totally. Under total internal reflection (TIR), the incident and reflected waves have equal energy, what means that no energy is lost at the interface. That results that surface wave intensity distribution must have an evanescent character perpendicular to the interface (in z direction) extended into material n_1. To understand the characteristic of evanescent behavior, we introduce the wave vector $\overrightarrow{k_l}$ here.

$$\overrightarrow{k_l} = k_{lx}\vec{e}_x + k_{ly}\vec{e}_y + k_{lz}\vec{e}_z \qquad \text{(Eq. 2-20)}$$

The index l stands for the corresponding material and $\vec{e}_{x,y}$ are the unit vectors parallel and $\vec{e}_z$ perpendicular to the interface. The amplitude of the wave vector $k_l = \left|\overrightarrow{k_l}\right| = 2\pi n_l/\lambda$ relates to the excitation wavelength λ. We define that the projection of the incidence beam to the interface is parallel to the direction of x. Given from Snell`s law the wave number in both interface materials must be identical [37].

$$k_1 = \sqrt{k_{1x}^2 + k_{1z}^2} = \sqrt{k_{2x}^2 + k_{2z}^2} = k_2 \qquad \text{(Eq. 2-21)}$$

That means, if one directional component of the wave number becomes larger than the total component, the other directional component must be imaginary. In this case, the electric field in this direction is limited and follows an exponential decay [37].

We visually the scenario in figure 2-5. From the perspective of wave fronts in x direction, the spacing $\lambda'(\vartheta) = 2\pi/k_2 \sin\vartheta$ is given by geometrical projection of wavelengths at the interface by oblique incidence angle. Increasing ϑ reduces $\lambda'(\vartheta)$. At the critical angle, $\lambda'(\vartheta_{crit})$= $\lambda_1 = 2\pi/k_1$ matches the

photon wavelength of the light propagating medium n_1. For overcritical illumination, $\lambda'(\vartheta)$ becomes more narrow than the natural propagation wavelength, so $k_{1x}^2 > k_1^2$. To fulfill equation Eq. 2-21, k_{1z}^2 must be negative, so k_{1z} must be imaginary. Since, the electric field components of propagating electromagnetic waves are given over an exponential function $E_{x,y,z} \propto e^{ik_{x,y,z}r_{x,y,z}}$, an imaginary wave number in the z direction results in an exponential decay $E_z \propto e^{-k_z z}$ of the electric field in this direction. We can describe the evanescent intensity distribution in z direction:

$$I(z) = E_z E_z^* = I_0 e^{-2k_z z} = I_0 e^{-z/\delta} \qquad \text{(Eq. 2-22)}$$

Where the illumination angle is depending on penetration depth $\delta(\vartheta)$ and is given by [37]:

$$\delta(\vartheta) = \frac{1}{2k_z} = \frac{\lambda}{4\pi n_2}(\sin^2\vartheta_{crit} - \sin^2\vartheta)^{-1/2} \qquad \text{(Eq. 2-23)}$$

Solutions for the penetration depths are given for $\vartheta > \vartheta_{crit}$. Figure 2-5(b) displays the intensity distribution with an exponential decay ($I \propto e^{-z/\delta}$) under oblique illumination $\vartheta > \vartheta_{crit}$.

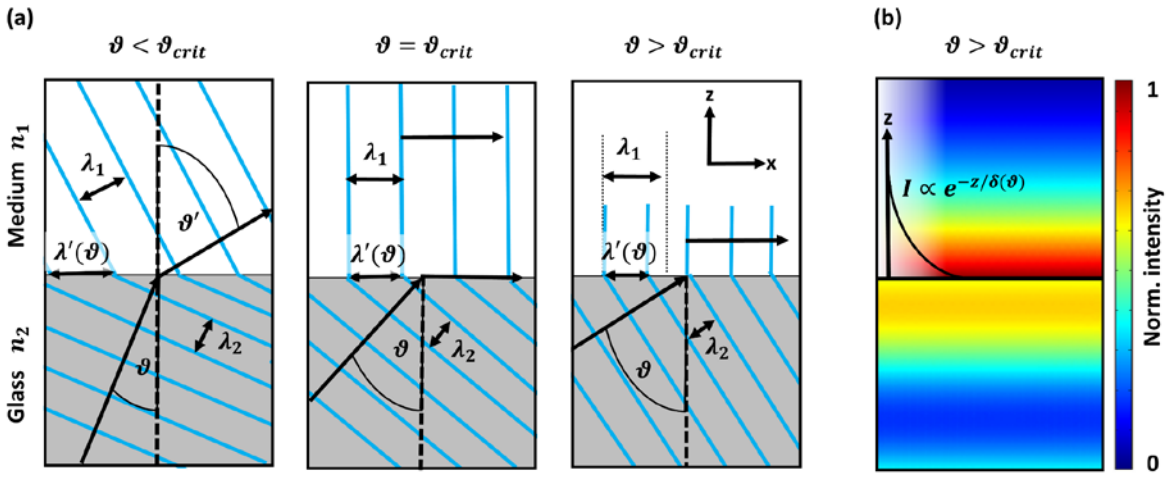

Figure 2-5. (a) Illustration of evanescence field generation at an interface of two dielectric interfaces with $n_2 > n_1$. (b) Intensity distribution of evanescent field in the z direction.

Evanescent waves at noble metal-coated interfaces

In the previous section, we investigated the formation of an evanescent field at the interface between two dielectric materials. In dielectric materials, charge carriers are fix localized and cannot move inside the material. In practice, dielectric materials are used, which are transparent for the spectral range of interest. Thus, it was sufficient to describe the interface by the real valued refractive indices n_l. In metals, free charge carriers (electrons) are not bound to a lattice structure and can move throughout their material within their conduction band. In order to describe the optical properties of the metal, the refractive index must be extended to a complex value $\tilde{n}_m = n_m + i\mathrm{K}_m$. It is common to express the optical response of a material via the complex dielectric function $\varepsilon_m(\omega) = \varepsilon'_m(\omega) + i\varepsilon''_m(\omega)$ [55]. Note here that dielectric functions and complex refractive index have the same information content and can be converted into each other [55]. The argument $\omega = 2\pi c/\lambda$ shows that the dielectric function is spectrally dependent.

Drude's theory (free electron model) demonstrates that the dielectric function of a metal can be described by one Lorentz function with a center peak position $\omega_0 = 0$ [55].

$$\varepsilon_m(\omega) = \varepsilon_\infty + \frac{\omega_p^2}{\omega_0^2 - \omega^2 - i\omega\Gamma} = \varepsilon_\infty - \frac{\omega_p^2}{\omega^2 + i\omega\Gamma} \qquad \text{(Eq. 2-24)}$$

Here the amplitude ω_p^2 is the plasma frequency, ε_∞ is an offset describing the high frequency limit and Γ describes the damping of the electron transport. Figure 2-6 shows the dielectric function and complex refractive index of gold. In a Drude-like dielectric function, the real part of the dielectric function starts with ε_∞ and drops with the wavelength $\varepsilon'_m \propto \varepsilon_\infty - \omega_p^2\lambda^2$ while the imaginary part rises $\varepsilon'_m \propto \Gamma\omega_p^2\lambda^3$ [69]. The dielectric function of gold follows perfectly a Drude function with exceptions in the inter-band spectral regime. The inter-band transitions are describable by Lorentz-like dielectric functions with center peaks at 400 nm [55, 70]. In figure 2-6(b) the real component of the refractive index is at the inter-band transition area above one, and later drops to nearly zero in the spectral area, while the absorption coefficient K_m rises with the wavelength.

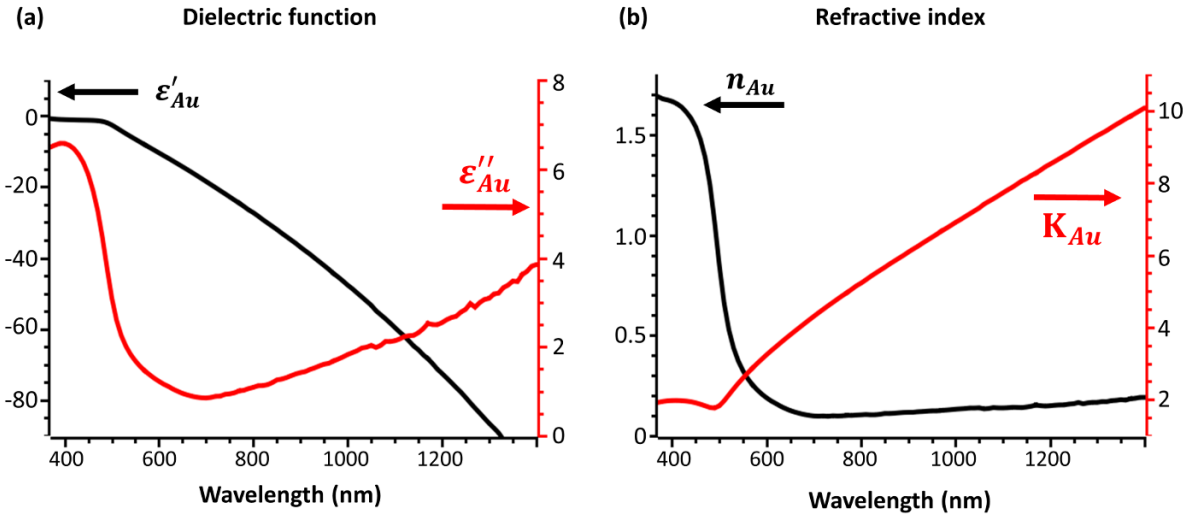

Figure 2-6. Real (black) and imaginary (red) part of dielectric function (a) and complex refractive index (b) of gold. Plotted data are taken from McPeak et al. [71] (derived from www.refractiveindex.info).

Surface plasmons in noble metal thin films are collective coherent oscillations of free electrons propagation along the metal surface [68]. For excitation of plasmonic surface waves we consider a metal-nanocoated interface between two dielectric materials with refractive indices n_1 and n_2, where $n_2 > n_1$. Now electrons can be resonantly excited what modifies the surfaces waves and can

gain strong localized electric field amplitudes at the interface. This resonant excitation of electronic surface waves is called surface plasmon resonance (SPR) [68, 72]. In figure 2-7 the scenario is illustrated. We consider, that the projection of the incoming light to the interface is in x direction and parallel to the propagation of the surface wave. The z direction points towards the material with RI n_1. The boundary conditions can be described as follows [72].

$$k_x^2 - k_{z1}^2 = n_1^2 k^2 \quad \text{(Eq. 2-25)}$$

$$k_x^2 - k_{zm}^2 = \varepsilon_m k^2 \quad \text{(Eq. 2-26)}$$

The dielectric function of the metal is a complex expression; it follows the wave vector for the surface plasmon propagation in x direction is complex as well [72, 73].

$$k_x' + ik_x'' = k\sqrt{\frac{\varepsilon_m n_1^2}{\varepsilon_m + n_1^2}} \quad \text{(Eq. 2-27)}$$

Surface plasmons are transversal magnetic (TM) waves. That means that only p-polarized oblique excitation can excite the surface plasmon resonance in flat metal nanocoatings. In addition, surface plasmons are resonant excitable under a specific illumination angle ϑ_{SPR}. At surface plasmon resonance (SPR), the surface plasmon propagation in x direction is $k_x = k\, n_2 \sin\vartheta_{SPR}$. Together with the previous equation, the illumination angle for the plasmon resonance is [72]:

$$\sin\vartheta_{SPR} = \frac{1}{n_2}\sqrt{\frac{\varepsilon_m n_1^2}{\varepsilon_m + n_1^2}} \quad \text{(Eq. 2-28)}$$

By comparison with the critical angle, we see that ϑ_{SPR} always exceeds ϑ_{crit}. Figure 2-7(b) shows the comparison of reflectance and field enhancement $|E|^2/|E_0|^2$ depending on the excitation angle ϑ. For undercritical angel illumination, the gold coated interface has an increased reflectivity in contrast to bare glass/medium interface. Above the critical angle, the reflectivity rises but extremely breaks down near ϑ_{SPR}. The low reflectance at ϑ_{SPR} corresponds to plasmonic light absorption. The resonantly excited surface plasmons enforce the excitation field at the interface. If the SPR condition is not reached, the electric field amplitude ratio at the interface is nearly zero.

The equations above well describe the plasmon excitation for the metal film between two materials. In practice, additional layers like an adhesion promoter and a dielectric capping layer are needed. Approaches for analytical calculation of the optical properties and plasmon excitation of a multilayer system exist [74, 75], however, with the help of finite element method (FEM), we get access to all parameters needed to get a deeper understanding of the surface plasmon phenomenon (for FEM details see the method part). In figure 2-8(a) we see a simulation of the electric field component representing the surface wave character of the electric field. Figure 2-8(b) shows a heat map of field enhancement for a gold nanocoating multilayer system with different gold thicknesses and excitation angles. Interesting is the ϑ_{SPR} development from the uncoated interface to thicker coatings, while ϑ_{crit} stays unaffected. The strongest field enhancement is observable for around 45 nm gold thickness, therefore this is the typical gold coating thickness for SPR applications [76-78].

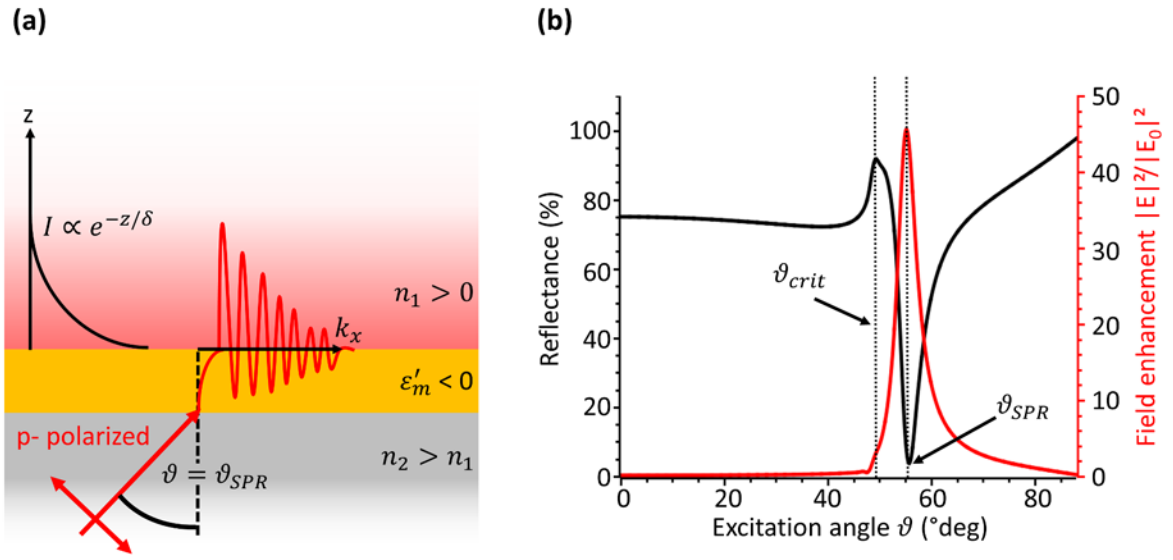

Figure 2-7. (a) Schematic illustration of surface plasmon resonance (SPR) excitation on a metal nanocoating ($\varepsilon'_m < 0$) between two dielectric materials. (b) Reflectance and field enhancement of a 50 nm gold layer on a glass substrate (RI = 1.78) in an aqueous environment (RI = 1.33). Spectra are FEM calculations for p-polarized excitation (λ = 640 nm) and different ϑ.

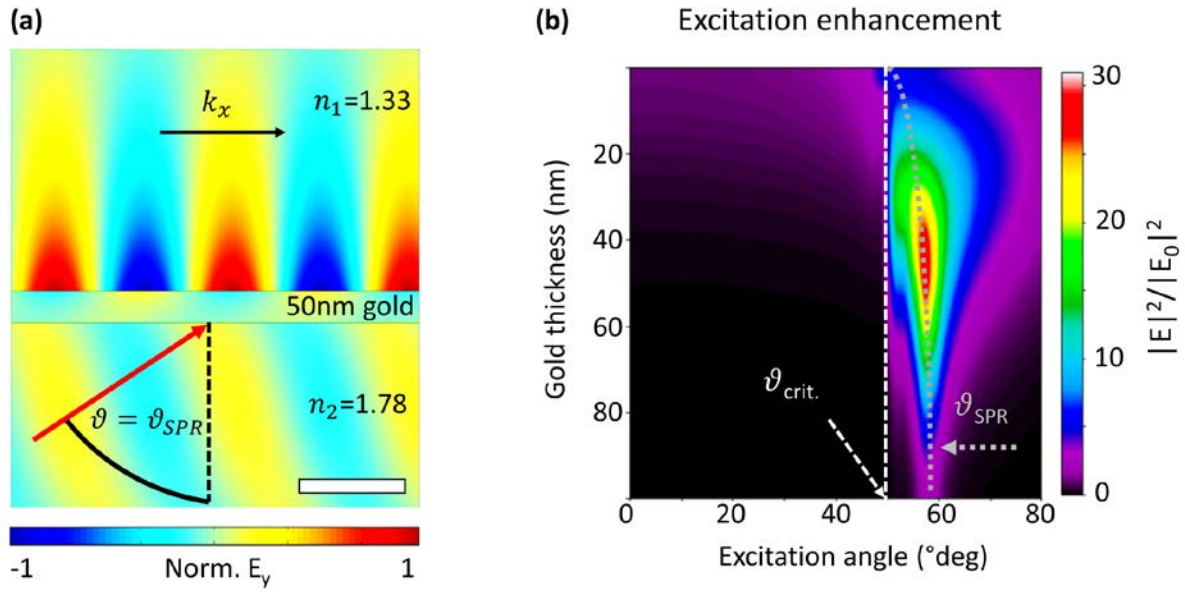

Figure 2-8. (a) Finite element method (FEM) simulation of the electric field component E_y under surface plasmon resonant excitation (SPR). Scale bar 200 nm. (b) Excitation enhancement of a multilayer system for different gold coating thicknesses. Here the multilayer system contaoins a glass substrate (NLAFN-21), a 2 nm chromium adhesion layer, a gold coating, a 6 nm silicon nitride capping in an aqueous environment (RI = 1.33). The simulations are performed for p-polarized 640 nm collimated light under different excitation angle. Critical excitation angle and SPR angle are indicated.

2.3 Emission near interfaces

In practice, fluorescent molecules are embedded into a transparent aqueous or cellular environment. The sample is placed on a microscopy slide with a certain refractive index (RI) higher than the RI of the sample. This refractive index mismatch forms an optical interface. Similar to oblique angle illumination, surfaces waves are excitable on this interface by dipole emission. If the florescent dye is close enough to the surface, fluorescence emission couples to the surfaces wave and radiates with a characteristic emission pattern into the material with higher RI. This effect is called supercritical angular fluorescence (SAF [37, 79]) or surface plasmon-coupled emission (SPCE [80, 81]) for an uncoated or a plasmonic-coated coverslip-to-medium interface, respectively.

A reflective coating on the interface modifies the emission properties of the fluorophore in the vicinity to the surface. In the sixties, Drexhage [82], already investigated this effect by placing fluorescent europium ions next to mirror surfaces. Just a few years later, Change, Prock, and Silbey (CPS theory [83, 84]) gave the theoretical explanation. The CPS theory uses a driven damped harmonic oscillator model to explain the emission changes in vicinity to the reflective surface. This emission modification depends on the fluorophore to surface separation distance (z direction). For fluorophores in few nanometers above nanocoating, the fluorescence lifetime is strongly reduced and rises within a subwavelength distance range to an unquenched value. By encoding the axial fluorescence distances over the fluorescence lifetime [85-87] or by corresponding spectrally coded emission shifts [88], axial super-resolved florescence microscopy is possible. This is in particular useful for axial super-resolved 3D reconstruction of cell membranes.

In this section, the optical interaction of a fluorescent emitter in the vicinity to a dielectric and a plasmonic interface will be introduced. Firstly, we will start with surface wave coupled emission (SAF and SPCE) and continue with height deepening changes in fluorescence emission properties.

Surface wave-coupled emission of fluorescent emitters near surfaces

In the previous section, we discussed the generation of evanescent surfaces waves on oblique angle illumination. We further discussed the resonance conditions and field enhancement properties of the evanescent field. Based on this knowledge, we describe surface wave-coupled dipole emission. Depending on the orientation and z distance of the dipole, emitted photons strike the interface under different angles. As in the case of oblique excitation, the excitability of surface waves is dependent from illumination angle and polarization. Figure 2-9 shows schematic illustrations of fluorescence emission through uncoated and gold coated interface. In case of a bare dielectric interface, fluorescence can emit through the surface. A fraction of emission is bended to high emission angels close to the critical angel of the interface [37, 79]. This occurs with a higher probability for photons that reach the interface with high incidence angles. Incident radiation at lower angles is less affected by the interface and passes almost unbent. The emission fractions of the radiation passing the interface below and above the critical angle are called undercritical angle fluorescence (UAF) and supercritical angle fluorescence (SAF) [89, 90].

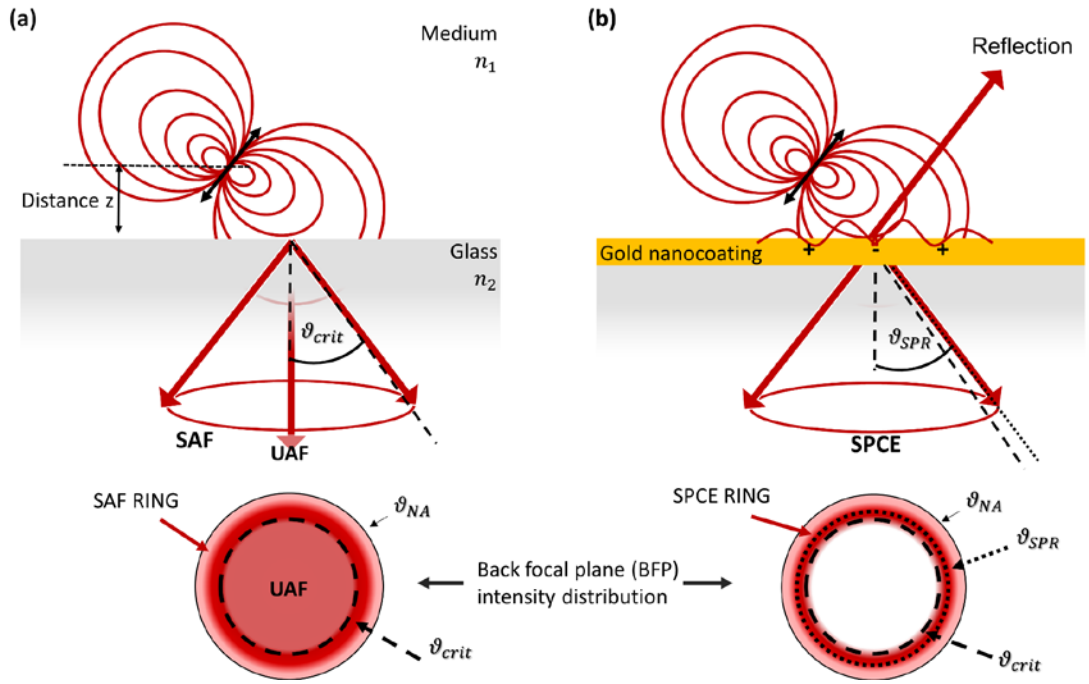

Figure 2-9. Schematic illustration of radiation modes of a dipole emitter at nanometer distance z above an interface. (a) Fluorescence emission of supercritical angle fluorescence (SAF) and undercritical angel fluorescence (UAF) above a medium glass interface ($n_2 > n_1$) are indicated. (b) Fluorescence emission near a plasmonic gold nanocoating. The excitation and coupling of surface plasmons resulting fluorescence emission into the glass under the surface plasmon resonance excitation angle ϑ_{SPR}. Emission angle signal collection at the objective lens back focal plane (BFP) is illustrated.

In the case of the plasmonically coated interface, two additional effects occur. On the one hand, the reflectivity of the surface increases significantly, so that the signal detectable by the boundary layer is reduced. On the other hand, surface plasmons can be excited. Due to the coupling of the fluorescence emission with surfaces plasmons (SPCE), fluorescence can radiate under narrow angular distribution (close to ϑ_{SPR}) through the metal. This effect is easily affected by surface sensitivities and polarization [52, 80, 91, 92]. Because of the high surface reflectivity and SPCE, fluorescence detection through plasmonic coatings can only be effective for molecules originated from a few nanometer-thin area above the coating. Since SPCE emits under ϑ_{SPR} into the glass substrate, a very high numerical aperture (NA) objective is need to collect SPCE. For aqueous and cellular samples ($n_1 \geq 1.33$), standard TIRF objectives designed for standard glass coverslips ($n_1 \approx 1.5$) are not sufficient for SPCE collection, since $\vartheta_{SPR} > \vartheta_{NA}$. Fortunately, for this case high refractive index coverslips (NLAFN-21; RI = 1.78) and high NA TIRF-M objective lenses (NA $\geq$ 1.65) can be used [51, 77, 93]. In following, we consider coverslips with RI=1.78 and a TIRF objective lens with NA=1.7.

Both effects, SAF/UAF and SPCE, are depended on fluorophore distance and orientation to the surface. Figure 2-10 shows radiation patterns of dipole emitters on an uncoated and gold coated medium/glass interface. For the case of an uncoated medium/glass interface (n_1/n_2 = 1.33/1.78) two different radiation patterns occur for dipole orientation perpendicular (⊥) and parallel (∥) to the surface. For ∥ the radiation directivity rather unaffected by the interface and shows the characteristic dumbbell pattern with propagation direction perpendicular to the surface. For ⊥ fluorescence, a characteristic angular distribution into the higher RI material is observable. This "butterfly" shaped SAF radiation pattern emits the highest fraction of radiation closely above the critical angel ϑ_{crit} [79]. By this effect, only a very high numerical aperture objective (e.g., suitable for TIRF-M) can collect SAF fluorescence emission, with the result of enhanced detectability of surface near fluorophores. By increasing the dipole distance z to the surface, SAF effect become less dominant. The SAF detection efficiency, follows

an exponential decay. This axial dependency is in particular useful for surface sensitive spectroscopy and axial super-resolved imaging [89, 90, 94, 95]. For the plasmonic interface and ∥ oriented dipoles, radiation through the surface is less detectable. For the dipole ⊥ to the surface, SPCE allows sufficient emission detection. SPCE is more efficient for dipole near field distances. The axial working regime for SPCE is indicated in figure 2-10.

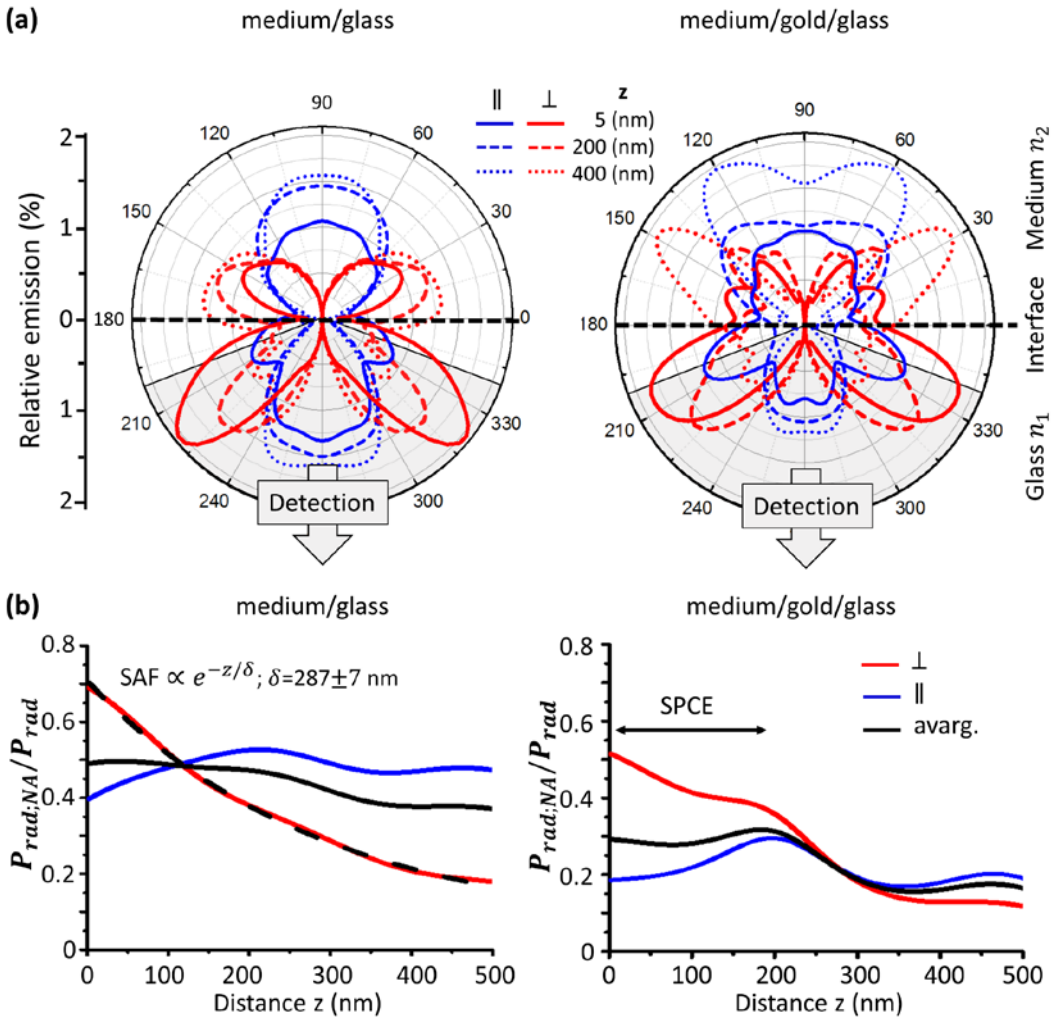

Figure 2-10. (a) Radiation patterns of a dipole emitter located above an uncoated (left) and gold coated medium/glass interface (n_1/n_2 = 1.33/1.78) for dipole oriented parallel (blue, ∥) and perpendicular (red, ⊥) to the interface. Gray area indicates fluorescence collected by an objective lens (NA = 1.7). (b) Distance z depended on detection ratio $P_{rad;NA}/P_{rad}$ for both cases. Exponential decay character of SAF and effective regime for SPCE are indicated. FEM simulations for 670 nm dipole emission wavelength.

Axial-dependent emission rate changes near metal coatings, CPS theory

When a dipole emits near a reflective surface, it may receive a part of its previously emitted radiation. According to Chance, Prock and Silbey (CPS theory [83, 84, 96, 97]), an emitting dipole (with dipole moment p) near a reflecting surface can be described by driven damped harmonic oscillator [96].

$$\ddot{p} + \tau_0^{-1}\dot{p} + \omega^2 p = (e^2/m)E_r \qquad \text{(Eq. 2-29)}$$

Here are τ_0 the unmodified fluorescence lifetime, ω the dipole emission frequency and E_r the electric field of the reflected emission at dipole position. The factor e^2/m describes effective charge and mass of the dipole emitter. The solution for the harmonic oscillator and electric field are given by $p = p_0 e^{-i\Omega t}$ and $E_r = E_{r;0} e^{-i\Omega t}$ with a complex oscillation frequency Ω. A substituted equation for the complex oscillator frequency Ω can be given by [96]:

$$\Omega^2 - \omega^2 - i(\tau_0^{-1})\Omega = e^2/(p_0 m)E_{r;0} \qquad \text{(Eq. 2-30)}$$

and therefore

$$\Omega = -\frac{i}{2\tau_0} + \omega\sqrt{\left(1 - \frac{1}{4(\tau_0\omega)^2} - \frac{e^2 E_{r;0}}{p_0 m\omega^2}\right)} \qquad \text{(Eq. 2-31)}$$

where with absence of all damping $\Omega = \omega$. With the extension of $p = p_0 e^{-i\Omega t}$ = $p_0 e^{-i\omega\prime t} e^{-t/(2\tau)}$ we introduced the lifetime τ in the vicinity of a reflective surface. According to the CPS theory (e.g. [96]), an approximation for the fluorescence lifetime is given by:

$$\tau^{-1} = \tau_0^{-1} + (e^2/(2p_0 m\omega))\mathrm{Im}(E_{r;0}) \qquad \text{(Eq. 2-32)}$$

Thus the relative lifetime change τ/τ_0 can be written with the intrinsic quantum yield $QY_0 = \tau_0 k_{rad;0}$, where $k_{rad;0} = 2e^2\omega^2 n_1/3c^3 m$ as follow:

$$\frac{\tau}{\tau_0} = \left[1 + \frac{3QY_0 c^3}{2p_0 n_1 \omega^3}\mathrm{Im}(E_{r;0})\right]^{-1} \qquad \text{(Eq. 2-33)}$$

As previously discussed, the electric field strength follows a r^{-n} behavior, where the exponent n ranges from three to one (near- and far field radiation). Under the assumption, the electric field is directly reflected by the surface in z direction, the relative fluorescence lifetime follows a $\propto z^n/(z^n + \alpha)$ behavior, where α summarizes all distance independent terms. In absence of reflected emission ($E_{r;0} = 0$), τ becomes τ_0, this is the case of high dipole to surface separation distances z. The theoretical introduction of fluorescence lifetime changes near reflective surfaces should be sufficient for now. The calculation of the reflective electric field can be done analytically near different reflective (e.g., metallic or semiconductor) surface geometries (e.g., in CPS theory and others [96-99]) in great agreement with experimental measured axial dependent fluorescence lifetime changes [83, 100-103].

Consider now an example of changes in relative fluorescence emission rates near a gold-coated surface. Figure 2-11 shows the dependencies of the emission rates for different distances to a gold nanocoating. If the dipole is just a few nanometers separated to the surface, a strong reflected electric field is present at the dipole position. In addition, sufficient excitation of surface plasmons takes place. This means that, on the one hand, the radiative rates are amplified by the excitation gain of the

reflection. On the other hand, there are absorption losses by the plasmon excitation. It follows the radiative and non-radiative are both enhanced near the metal. This strongly shortens the fluorescence lifetime. By increasing the distance of the dipole to the surface, the field amplitude of the reflected light at the location of the dipole emitter is reduced and the absorption losses on the metal layer decrease with greater distance. This increases the fluorescence lifetime by approaching the value τ_0. It should also be noted, that for dipole orientation ∥ to the reflecting surface, there is interference between the dipole emission and the reflective emission. Thus, depending on the constructive and destructive interference, the excitation rates may increase and decrease resulting in a swing of the fluorescence lifetime and emission rates near the undisturbed level.

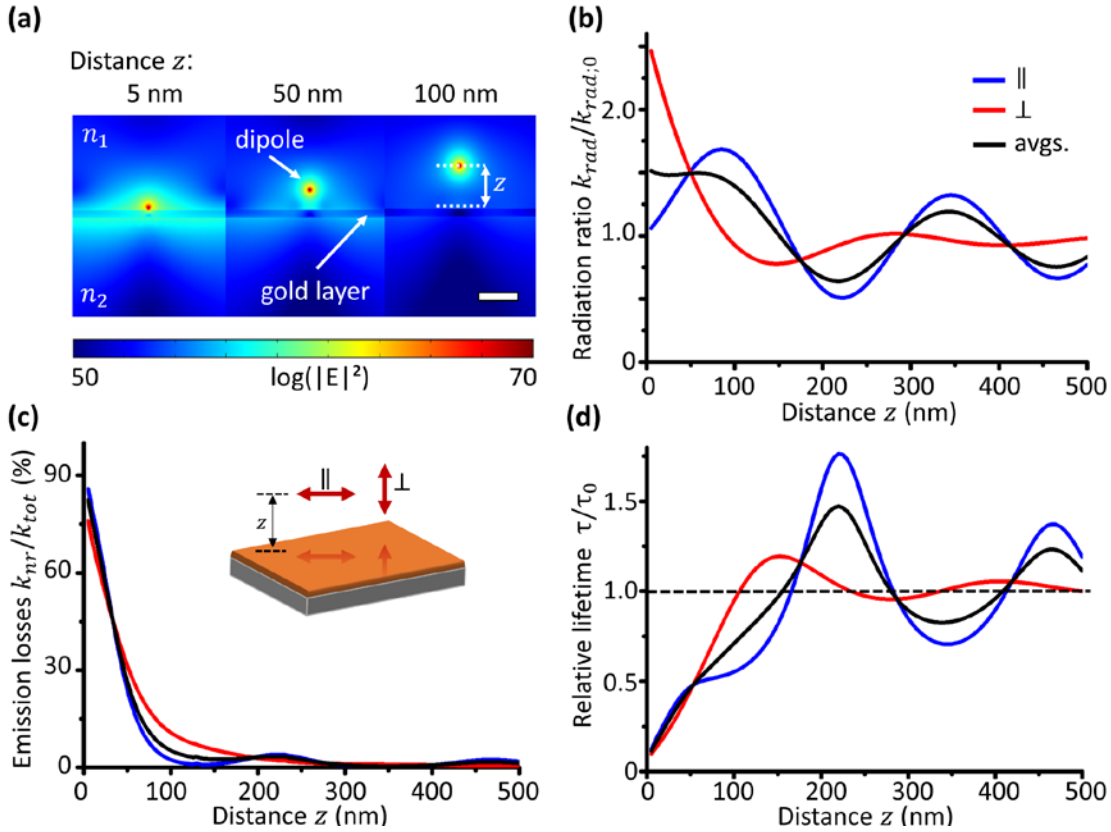

Figure 2-11. (a) Electric field distribution of a dipole emitter with distance z above a 20 nm gold nanocating on medium/glass interface (n_1/n_2 = 1.33/1.78). Dipole emits at 670 nm and is oriented perpendicular (⊥) to the surface. Scale bar 100 nm. (b) Radiation rate changes $k_{rad}/k_{rad;0}$, (c) relative emission losses k_{nr}/k_{tot} , (d) relative lifetime changes τ/τ_0. Calculations performed for a dipole emitter (λ = 670 nm) at distances z with orientations to the surface parallel (∥,blue), perpendicular (⊥,red), and orientation average (black).

It has been shown that both radiative and nonradiative rates increase near the metal coatings. To get an idea of how this changes the brightness of the fluorescent molecule, we consider the quantum yield QY near a nanocoating. If the dipole emitter is a fluorescent molecule, then the quantum yield in free space contains radiative and non-radioactive rates $QY_0 = k_{rad;0}/(k_{rad;0} + k_{nr;0})$. By analogy, the quantum yield modified near the surface is given by $QY = k_{rad}/(k_{rad} + k_{nr} + k_{abs})$. Since the intrinsic nonradiative rates are unchanged by the nanocoating, we can insert QY_0 in QY to get the following expression for the quantum yield [68, 104]:

$$QY = \frac{k_{rad}/k_{rad;0}}{k_{rad}/k_{rad;0} + k_{abs}/k_{rad;0} + (1 - QY_0)/QY_0} \qquad \text{(Eq. 2-34)}$$

This expression for the quantum yield not only includes radiative and nonradiative emission rates, but also the intrinsic quantum yield QY_0 of the fluorescent dye. Figure 2-12 shows relative quantum yield changes of fluorescent emitters with different QY_0 in distance z to a gold nanocoating. The distance behavior of the quantum yield looks at the first glance very similar to the lifetime behavior in figure 2-3. For very short distances, the quantum yield is greatly reduced. The reason is, that for short distances high emission loses take place by light metal absorption and plasmon excitation, even if there is a high radiation rate enhancement. Increasing the distance increases QY to the unmodified value QY_0. Like lifetime changes, the quantum yield changes swing around the unmodified value QY_0. Interestingly, the amplitudes of this swinging are dependent on the intrinsic quantum yield. The amplitudes are strongest for low QY_0. As a result, there are areas where a quantum yield enhancement occurs. This distance range is where absorption losses no longer dominate, but emission enhancement is present. Fortunately, this distance range matches with the typical cell membrane distances to the coverslips [105-108]. As a result, metallic nanocoated coverslips can be used to increase the signal of fluorescently labeled membrane proteins in living cells.

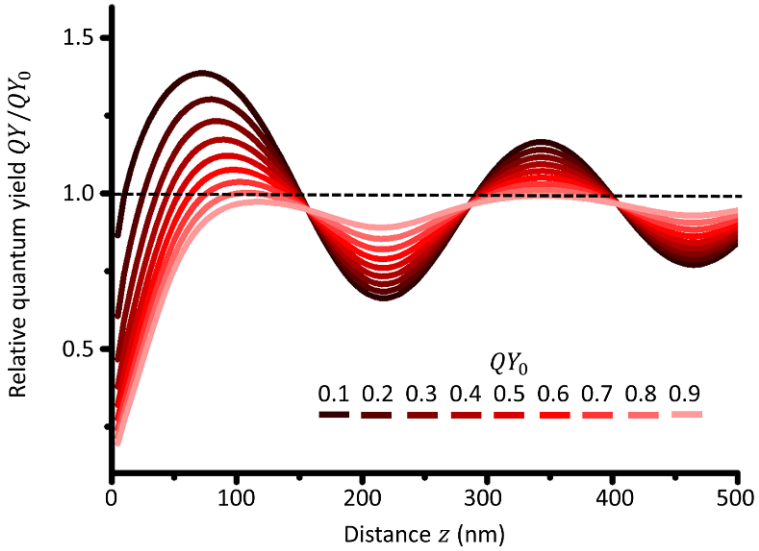

Figure 2-12. Relative quantum yield changes QY/QY_0 of a fluorescent emitter with distance z above a 20 nm gold coated glass substrate (n_1/n_2 = 1.33/1.78). Calculations are performed for dipole emitters (λ = 670 nm, averaged dipole orientations) with different intrinsic quantum yields QY_0.

3 Methods

3.1 Finite element method (FEM)

Finite element method (FEM) simulations are in particular useful to understand electromagnetic field interactions at different length scales. Several types of radiations can be implemented in Comsol Multiphysics. In this thesis, two cases of visible electromagnetic radiation are of interest. First, we are interested in how light behaves in a material transition for different angle of incidence. Depending on the design of the material system, different types of surface waves are excitable. Here are evanescent surfaces waves at dielectric interfaces and surface plasmons at metal-dielectric nanocoatings of particular interest. The second interesting system is the photonic interaction of a dipole emitter near such an interface. Surface waves are excitable, which radiate into the substrate (e.g., by supercritical angle fluorescence (SAF) and surface plasmon-coupled emission (SPCE)). These effects are dependent on the dipole orientation, distance to the surface z_{dipole} and emission wavelength λ. In addition, the back-reflected dipole radiation modifies the dipole emission. As discussed in the theory part, analytical expressions exist for surface plasmon resonance (SPR), SPCE and dipole emission changes in vicinity of reflective surface (CPS theory [97]). However, with electromagnetic simulations, we have several advantages. On the one hand, we gain access to all relevant physical processes at once (e.g., dipole emission characteristics, field enhancements, reflection and transmission coefficients, ...). In the other hand, we can visualize components of the electromagnetic field and the polarization. Going to more complex photonic environments, like multilayered nanocoating's or nanostructured materials it is wise to use FEM or other simulation methods (e.g., finite difference time domain [109, 110] or discrete dipole approximation [111, 112]), since analytical expressions are typically made for special cases including case-dependent approximations.

This section describes the two FEM models used in this thesis, using the electromagnetic wave frequency domain (ewfd) module of Comsol Multiphysics 4.4. One model calculates the oblique illumination for evanescent surface wave excitation at multilayered metal-dielectric interface. The second model describes the photonic interaction of a dipole emitter in vicinity of a multilayered metal-dielectric interface. Furthermore, if needed the described models can be extended to more complex systems.

Oblique illuminated and multilayered interfaces

The FEM model for oblique illumination at a (multilayered) material interface is described in the following. Figure 3-1 shows the model geometry. The model consists several rectangular domains, where $z = 0$ corresponds to the transition to the material with n_1. The material properties are given by the corresponding refractive indices (RIs). Comsol imports RIs (n and k values) as global definition via interpolation of data of original scientific publications (available via www.refractiveindex.info). A transition boundary condition (TBC) layer with thickness 2 nm describes the adhesion layer. A TBC layer enables implementation of ultrathin meterial transitions without the need of an extremely fine mesh grid, what would significantly increase the required computer resources. In principle, the other nanocatings could also be implemented as TBC. But in this case, not more than one TBC can be defined at one boundary. Excitation port and upper absorption port describing the electromagnetic inflow and outflow of the model. From this ports, reflection and transmission coefficients of the multilayer system are calculated. The ports are described by periodic ports with excitation angle ϑ (described by alpha in Comsol) and a detection angle (in Comsol asin(n2*sin(alpha)/n1), upper port). The port modes were set to magnetic field H = H0z for p-polarized illumination or E = E0z for s-polarization, while the

excitation field is periodic (set f0=c_const/lam0, and lam0 is λ and n = n2). Periodic boundary conditions (PBC) are needed to complete the geometry. The PBCs are set to use Floquet periodicity and the k-vector derived from the periodic port. For details of the used ports and PBC see e.g., Comsol model id 12407**.** For comparison of a coated and uncoated interface, we introduce the parameter M. The "uncoated" interface between n_1 and n_2 is realized by set the coating material RI = n_2. If M = 0, RIs of the coating are set to n_2 , for M = 1 the layers are represented by the RIs of the materials. As an example, the real part of the dielectric function for gold is n_{gold} = n_Au(lam0/1000[nm])*M+(1-M)*n2, where n_Au is the imported RI data of gold [71]. Alternatively, the change of RI can also be done by logic if-else expressions in form of if(M==1, n_Au (lam0/1000[nm]),n2).

The study is performed using a parameter sweep which solves the geometry for different model parameters (M = 0 or 1, illumination angel, lam0). For extracting results (e.g., maximum or mean values), an operator needs to be defined by components coupling beforehand. The results are stored after calculation. Normalized electric field distributions and electric field components can be plotted by 2D surface plots with ewfd.normE or ewfd.Ex (for Ex component). Under derived values, global evaluation allows to extract simulation results for different parameter sweep values at once. The S parameters of the port give expressions for reflectance and transmittance of the multilayered interface:

$$R = \mathrm{abs}(\mathrm{ewfd.S11})\text{^}2 \qquad \text{(Eq. 3-1)}$$

$$T = \mathrm{abs}(\mathrm{ewfd.S21})\text{^}2 \qquad \text{(Eq. 3-2)}$$

Here S11 and S21 describes the power flow from excitation port (port 1), reflected back to port 1 or transmitted to the upper absorption port (port 2). The amplitude of the evanescent wave decay in z direction is given by the average (by aveop operator) intensity distribution at the interface between the upper layer and material n_1 ($z = 0$):

$$I(z = 0) = I_0 = \mathrm{abs}(\mathrm{aveop}(\mathrm{ewfd.normE}))\text{^}2 \qquad \text{(Eq. 3-3)}$$

The electric field enhancement (FE) is given as intensity ratio. To describe the FE for SPR and TIR, we define the reference intensity at $z = 0$ for $\mathrm{M} = 0$ and $\vartheta = 0$ (normal illumination of the bare dielectric interface).

$$FE = \frac{I_0(\vartheta, M)}{I_{0;ref}(\vartheta = 0, M = 0)} \qquad \text{(Eq. 3-4)}$$

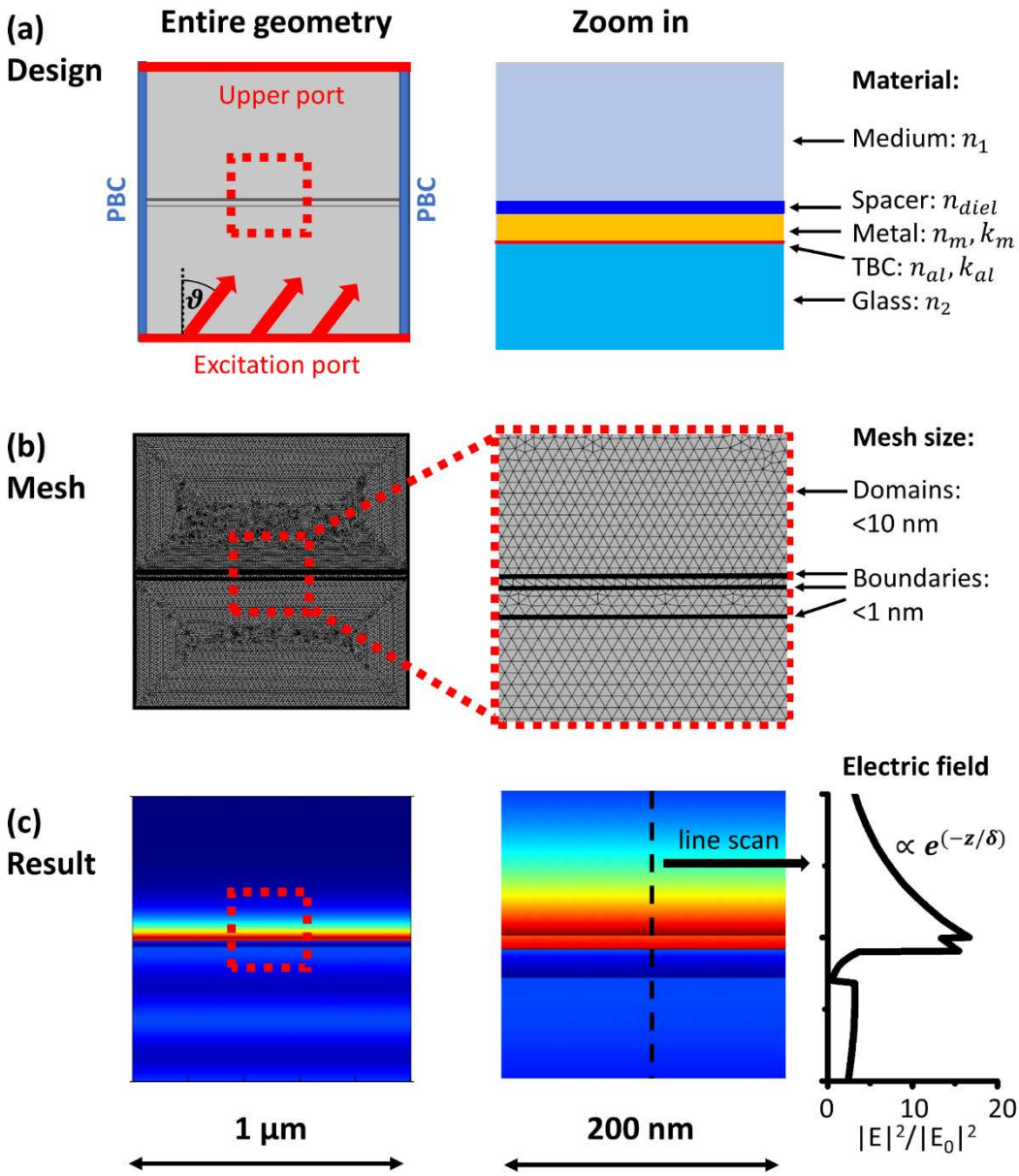

Figure 3-1. FEM model for oblique angle illumination of a multilayered material system (entire geometry and detailed zoom in left and right columns). (a) The model consists an excitation port for oblique illumination (angle ϑ) and an upper absorption port to receive transmitted illumination. Periodic boundary conditions (PBC) complete the model in the horizontal direction. The multilayered system consists of domains with different refractive indices as depicted. The transition boundary condition (TBC) is used to describe the ultrathin adhesion layer (al). (b) Illustration of the used mesh. (c) Result for an electric field distribution on a plasmonic interface system. The evanescent character of the electric field in the z direction is extractable by a line scan.

Dipole radiation near multilayered interfaces

Figure 3-2 shows the model to describe the dipole radiation close to a (multilayered) interface. To study the dipole radiation, a point dipole emitter is placed at $z = z_{dipole}$. The dipole components are described as follows:

$$\vec{p} = \begin{pmatrix} p_x \\ p_y \end{pmatrix} = \begin{pmatrix} \cos(\text{alpha\_d}) * \text{fl\_a647}(\text{lam0}/1[\text{nm}]) \\ \sin(\text{alpha\_d}) * \text{fl\_a647}(\text{lam0}/1[\text{nm}]) \end{pmatrix} (\text{Am}) \qquad \text{(Eq. 3-5)}$$

Here alpha_d describes the dipole orientation (0° (parallel,∥) and 90° (perpendicular,⊥)). The function fl_a647 is an imported fluorescence spectrum (here the dye Alexa647 imported from thermofisher.com). The geometry is completed by a 2nd order scattering boundary condition. To calculate the emission rates and far field radiation, two integration spheres are needed. One is 2 nm around the dipole emitter and the second surrounds the geometry. The integration spheres are depicted as "in" and "out" in figure 3-2. An outer integration sphere encloses the outer domain for calculation of the far field emission.

The study is performed using a parameter sweep which solves the model and stores the results for different model parameters. As described in the previous model, the electric field components can be plotted and exported. The far field radiation pattern can be derived by ewfd.normEfar and displayed by a polar plot. With global evaluation, the radiation rates for the different parameters are calculated and summarized. The line integration operators are named Ptot (inner integration sphere) and Prad (outer integration sphere). The names describe the radiation power outflow (ewfd.nPoav) leaving the dipole and the geometry. We can describe the radiation rate enhancements by comparison of the radiation powers for the bare interface (M = 0) and multilayered interface (M = 1).

Radiative emission rate enhancement:

$$\frac{k_{rad}}{k_{rad:0}} = \frac{\int_0^{360} p_{rad}(\varphi)d\varphi}{\int_0^{360} p_{rad:0}(\varphi)d\varphi} = \frac{P_{rad}}{P_{rad:0}} = \frac{\text{Prad}(\text{ewfd. nPoav})(\text{M} = 1)}{\text{Prad}(\text{ewfd. nPoav})(\text{M} = 0)} \qquad \text{(Eq. 3-6)}$$

Total emission rate enhancement:

$$\frac{k_{tot}}{k_{tot:0}} = \frac{\int_0^{360} p_{tot}(\varphi)d\varphi}{\int_0^{360} p_{tot:0}(\varphi)d\varphi} = \frac{P_{tot}}{P_{tot:0}} = \frac{\text{Ptot}(\text{ewfd. nPoav})(\text{M} = 1)}{\text{Ptot}(\text{ewfd. nPoav})(\text{M} = 0)} \qquad \text{(Eq. 3-7)}$$

And the detectability:

$$D = \frac{k_{rad;NA}}{k_{rad}} = \frac{\int_{-\varphi_{NA}}^{\varphi_{NA}} p_{rad}(\varphi)d\varphi}{\int_0^{360} p_{rad}(\varphi)d\varphi} = \frac{P_{rad;NA}}{P_{rad}} = \frac{\text{PradNA}(\text{ewfd. nPoav})}{\text{Prad}(\text{ewfd. nPoav})} \qquad \text{(Eq. 3-8)}$$

Where φ_{NA} is the maximum collection angel given by the numerical aperture of the assumed objective lens (NA=1.7). For practical reasons, this angular area is defined by a line segment in the geometry with the integration operator PradNA. The dipole orientation average rates are given by $\langle k \rangle = 1/3k_{\perp} + 2/3k_{\parallel}$ (see e.g. [113]), where the indices ⊥ and ∥ representing the corresponding dipole orientation. All simulations need to be performed for each dipole distance, dipole orientation and emission wavelength for both cases M = 1 and 0. Together with equations from theory section, all values of emission rate and quantum yield changes can be derived.

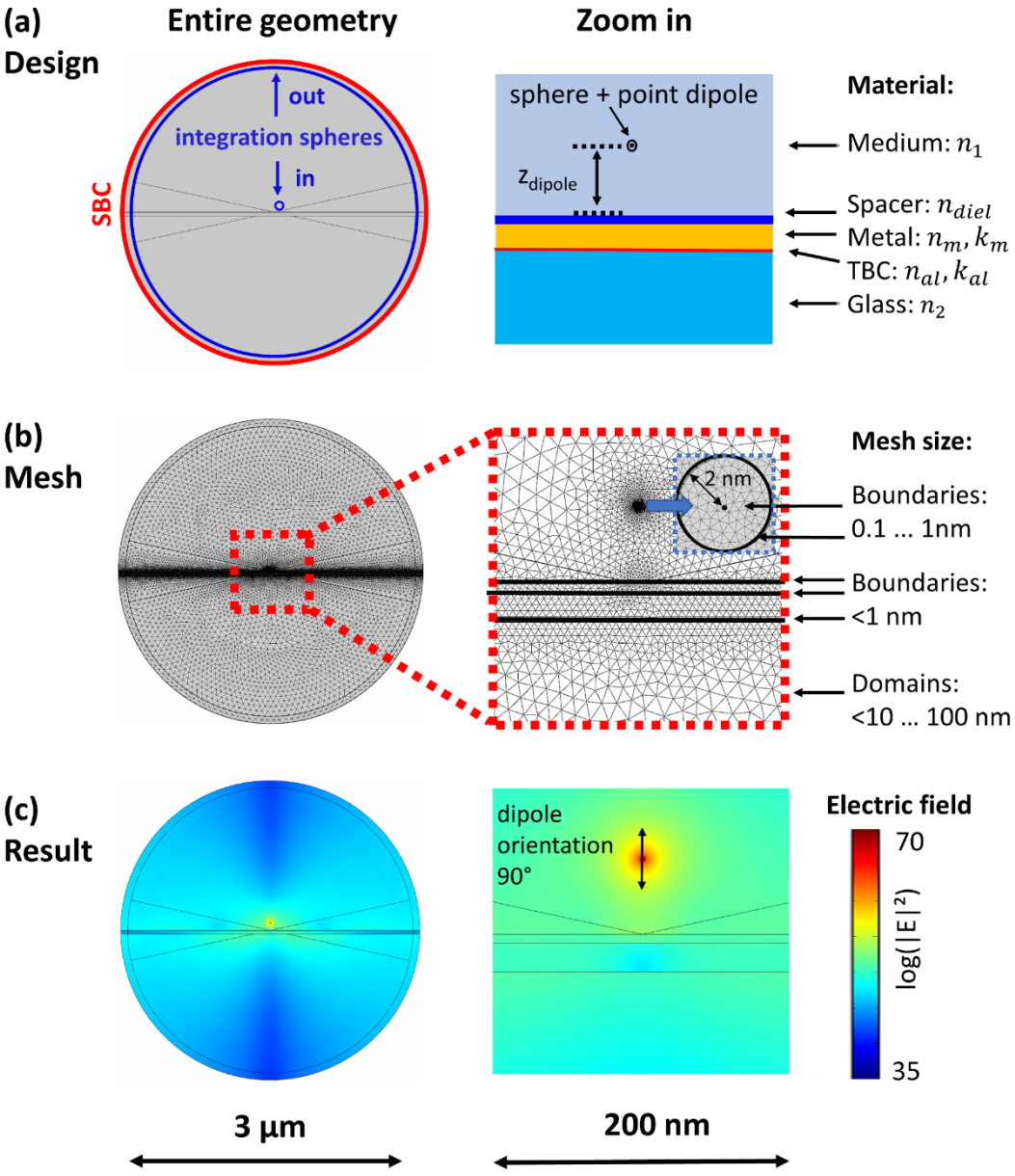

Figure 3-2. FEM model for an emitting point dipole near multilayered coated interface (entire geometry and detailed zoom in left and right columns). (a) The model consist of an emitting point dipole with distance z_{dipole} above the nanocoating. To extract radiative and nonradiative dipole emission rates, two integrations spheres are needed. The inner sphere is 2 nm around the dipole and outer is at the geometry edge. Scattering boundary conditions (2nd order) complete the geometry. The multilayered system consists of domains with different refractive indices as depicted. (b) Illustration of the used mesh. (c) Result of dipole emission close to a multilayered plasmonic interface.

3.2 Fabrication and characterization of nanocoated coverslips

This section describes the fabrication and characterization of the nano-coated coverslips. Depending on the application, different designs of nanocoatings on different substrates were produced. In this work, I focused on gold-coated coverslips, as they have high biocompatibility and chemical stability compared to other nanocoatings.

For the metal coatings, electron-beam physical vapor deposition (PVD) [114, 115] were used. For an optional dielectric spacer, radio frequency (RF) magnetron sputtering [114, 116] was used. The coverslips were analyzed by spectroscopic ellipsometry (SE) [117, 118] and atomic force microscopy (AFM)[119-121]. We start with the description of the used HEX thin film deposition system.

The Hex thin film deposition system

The hexagonally shaped HEX deposition system of the company Korvus Technology Ltd (United Kingdom) was used for nanocoating fabrication. The HEX is equipped with a TAU four-channel electron beam evaporator and a Fission radio frequency (RF) magnetron sputtering system. Further components are a sample stage and a quartz crystal microbalance (QCM) to monitor the deposition processes. In figure 3-3 the deposition system is shown. The samples are mounted on a sample holder (figure 3-3(d)). The sample holder (C) is from Korvus Technology and (A, B) are own designs made from aluminum (fabricated by Schaeffer AG, Germany*).* Components of vacuum system are controlled by different electronics, which all can be remotely controlled by the software Niobium 1.0 (Korvus Technology Ltd). A vacuum pre-pump (Agilent technologies IDP-3, Malaysia) and a turbo pump (Pfeiffer Vacuum TC110, Germany) evacuates the chamber. A vacuum pressure of approximately $5 \cdot 10^{-6}$ mbar is reached after around 30 - 40 min pumping, what is sufficient for our processes. By overnight pumping, the lowest possible vacuum pressure of approximately $8 \cdot 10^{-7}$ mbar is reachable. A water cooling circuit cools at 10°C (KT1 chiller from ATC, United Kingdom) the turbo pump, the TAU system, magnetron, and QCM.

TAU electron-beam deposition system:

For metal deposition, the TAU system was used. The TAU contains four independently heat-able crucibles. The metals chromium (1), gold (2), silver (3), and germanium (4) are located in crucibles (1-4). For PVD, the filament (0.15 mm diameter thoriated tungsten wire (W99/Th0.9) from Goodfellow, United Kingdom) is electrically heated with around one ampere. Electrons leave the filament and are accelerated by a 2 kV voltage to the respective crucible. The electrons heat the crucible. There is a 50 V voltage difference between the TAU and the vacuum chamber. The (partly ionized) evaporated material leaves the crucible into the direction of the sample stage. If the evaporated material sticks to the substrate, a layer is formed [114]. The heating power of the material can be adjusted and measured by the outflow of the electrons through the crucible. Typical heating powers are ranging from 50 W to 120 W depending on the coating material and deposition rates.

Fission radiofrequency magnetron sputtering system:

Magnetron radiofrequency (RF) sputtering is used for deposition of dielectric coatings. By inserting Argon (100 SCCM gas flow) into the HEX chamber, the chamber pressure increases. To strike the argon plasma, the pressure has to be further increased up to ≥ $2 \cdot 10^{-2}$ mbar. This is possible by decreasing the turbo pump speed (down to 40-60%). Now the argon plasma can be ignited (RF power typically with 50 W). The Fission system automatically tunes the RF source. When the plasma is burning, argon ions bombard the sputtering target. Under this ion bombardment sputtered atom (or atom compositions) leaves the target and can reach the substrate. Collisions between the gas molecules and the sputtered particles reduce the number of particles reaching the substrate. In order to increase the magnetron deposition rates, the pressure in the chamber must be reduced. This is achieved by reducing the argon gas inflow (to 20 SCCM or less) and increasing the frequency of the turbo pump (up to 80%).

Quartz crystal microbalance:

The deposition rates of the electron beam and magnetron deposition systems are detected by a quartz crystal microbalance (QCM). The QCM (Inficon SPC-992-G1-0, United States) is based on a gold-coated 6 MHz sensing crystal (LEWVAC TF-CRY, United Kingdom) and it is located close to the sample holder. Mass deposited on the QCM induces an oscillation shift what monitors the deposition rate ($\Delta m \propto \Delta f$ [122]). To derive the deposition rates, two values are needed. First the density of the used deposition material (See Table 2-1) and second the tooling factor. The tooling factor describes the relationship of the materials deposited on the QCM and the sample. This factor depends on the chamber geometry and location of the deposition system. Therefore, the tooling factor has to be determined individually for the different coating systems. The tooling factors are derived by test depositions of 10 nm, 30 nm and 50 nm of molybdenum (for magnetron) and gold (for TAU) on a silicon substrate (p-type (100) from Sciences Services, Germany). The film thickness was monitored by the QCM (with tooling factor 100). The real coating thickness was measured by Rutherford backscattering spectrometry (RBS) with a 2 MeV Helium ion-beam at the Helmholtz-Zentrum Dresden-Rossendorf. RBS spectra were analyzed with the software SIMNRA [123]. By comparison of coating thicknesses, tooling factors of 52 and 209 are derived for the TAU and the magnetron deposition system.

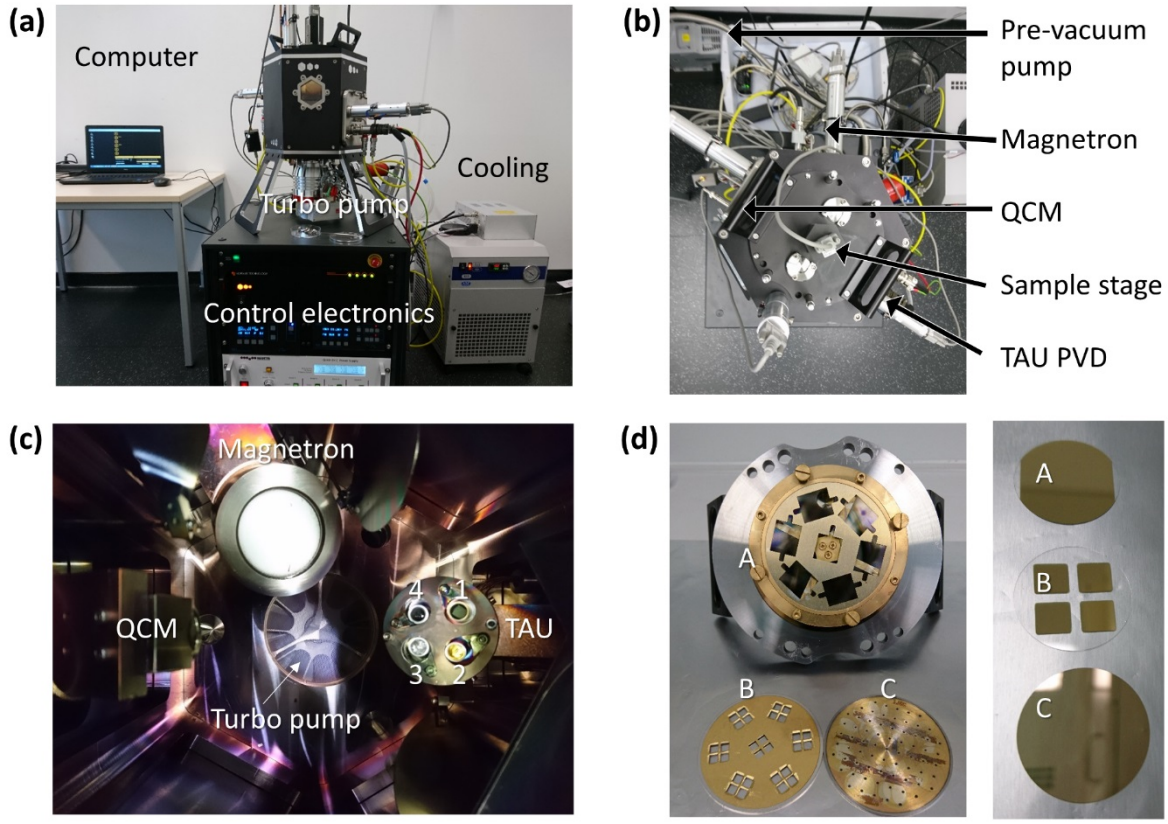

Figure 3-3. Photographs of Hex vacuum deposition system: (a) side-view (b) top-view (c) components inside the chamber and (d) used sample holder and sample holder plates (A, B, C). The components of the HEX are indicated and described in the text. The crucibles of the TAU system are numbered (1 to 4). (d) Photography's of coated coverslips were different sample holder plates (A-C) were used.

Material	Source	Tooling factor	Density (g cm^{-3})
Chromium (99.95%, 10 mm cubes, Goodfellow, UK)	Electron beam	209	7.14
Gold (99.99% <6 mm granulate, EVOCHEM, Germany)	Electron beam	209	19.32
Molybdenum (99.99% sputtering target, Ø 50.8 mm, 3 mm thick, Goodfellow, UK)	Magnetron	52	10.28
Silicon nitride (hot-pressed Si_3N_4 sputtering target, Ø 50.8 mm, 3 mm thick, Goodfellow, UK)	Magnetron	52	3.44

Table 2-1. Summary of the used deposition materials, manufacturer, deposition system with tooling factor and material density. Material densities were taken from https://en.wikipedia.org/.

Fabrication of nanocoated coverslips

The fabrication of the metal-dielectric coatings was performed in a HEX deposition system equipped with a RF magnetron sputtering (for dielectric coatings) and an electron beam evaporation system (for metal coatings). Two types of nanocoated coverslips are used in this thesis. One nanocoating is used for enhanced FRET experiments and a second for experiments in a total internal refection fluorescence microscope (TIRF-M). The difference between both nanocoatings are the coverslips. For FRET experiments a typical oil (RI = 1.515) objective lens was used. For the TIRF experiments, a special objective lens (NA = 1.7) is required designed for usage with special immersion liquid (Cargille M series n_D = 1.78, United States) and coverslips (NLAFN-21, 150 µm thick). The used coverslips are borosilicate glass coverslips (RI = 1.51, Ø = 24 mm, A. Hartenstein GmbH, Germany) and NLAFN-21 coverslips (RI = 1.78, NLAFN-21, Ø = 24 mm, 150 µm thick, UQG Optics Ltd, United Kingdom). The coverslips are cleaned by rinsing with acetone and isopropanol with subsequent dried by an oil free nitrogen stream.

The coverslips were mounted on the sample plate. The electron beam deposition was started when a base pressure ≤ $5 \cdot 10^{-6}$ mbar was reached. First, a 2 nm thick chromium adhesion layer was deposited with around 0.1 Å/s (100 W heating power) followed by the gold coating with typically 20 nm at around 0.3 Å/s (90 W heating power) unless otherwise stated. Additionally, the gold coating can be capped with a 6 nm silicon nitride spacer layer. The capping layer was deposited with the Fission RF magnetron with around 0.07 Å/s (RF power 50W, argon flux 20 SCCM, 80% pump speed, working pressure close to $2 \cdot 10^{-3}$ mbar).

Thin film inspection by spectroscopic ellipsometry

With spectroscopic ellipsometry (SE)[117, 118] the coatings are checked after evaporation. The spectrometer used is an alpha-SE (J.A. Woollam, United States) which operates with the software CompleteEASE 4.92. The spectra were recorded by variable angle spectroscopic ellipsometry (VASE) under the reflection angles of 65°, 70°, and 75°. SE measures polarization depending reflection coefficients (Δ, ψ), which we convert into the pseudo dielectric function. The pseudo-dielectric function consists of the dielectric functions of the individual layers [117, 118]. By a fitting model, which involves the optical properties of the materials, the layer thicknesses can be determined. The material functions used for fitting are from CompleteEASE database. For gold, the function Au_nk3, for chromium Cr_2 and for the silicon nitride SiNX-3CodyLor was used. The coverslip materials were described by the functions of BK7 and NLAFN-21. The figure 3-4 shows an example of an analyzed nanocoating.

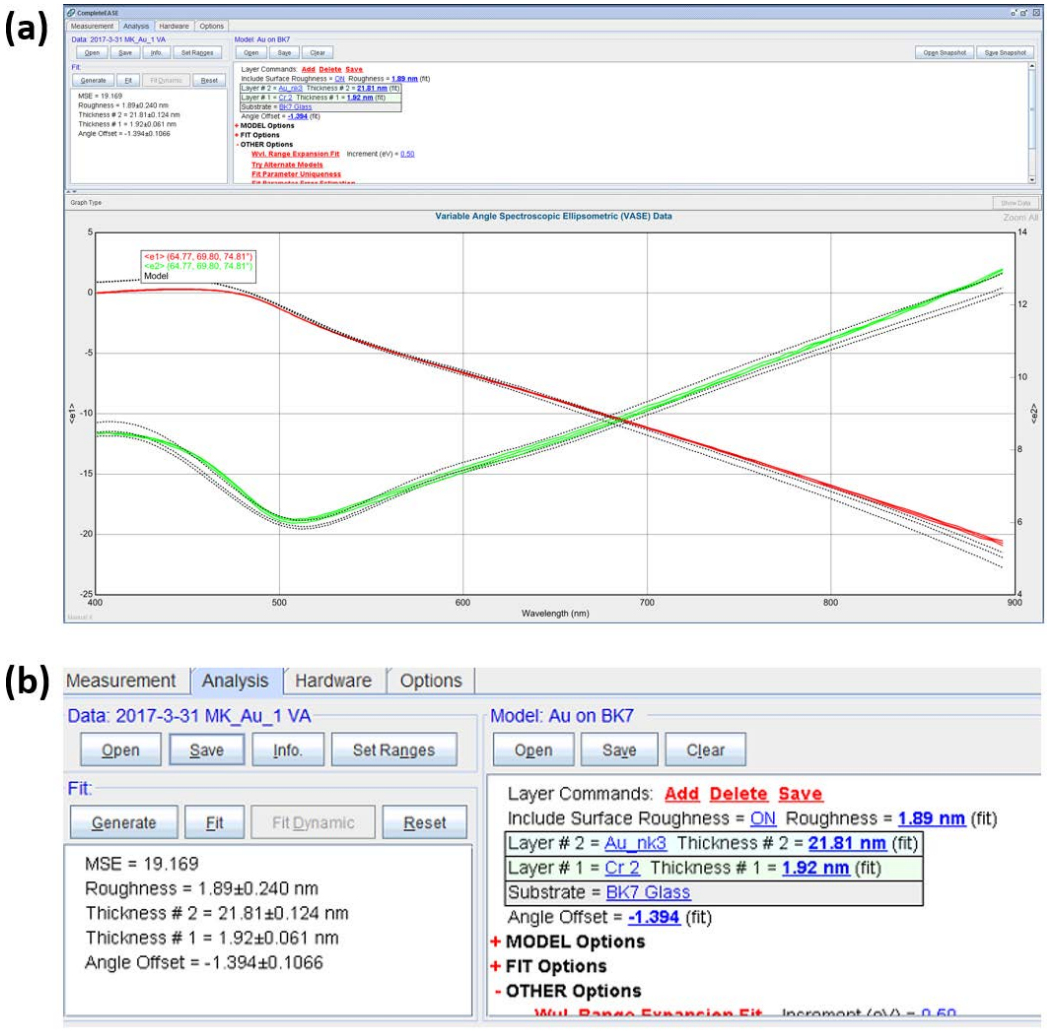

Figure 3-4. Example of thin film characterization via SE and CompleteEASE 4.92. (a) CompletEASE fit functions (black lines) and measured pseudo dielectric functions (green and red) of a 20 nm gold and 2 nm chromium coated borosilicate (BK7) glass substrate. (b) Zoom in to the model and corresponding fit results.

Roughness analysis with atomic force microscopy

Atomic force microscopy (AFM) [119-121] was used to analyze the surface roughness of the gold coatings. AFM measurements were performed with AFM probes (AC240TS, Olympus) mounted on an AFM (MFP-3D, Asylum Research, United Kingdom). Dr. Ingrid Tessmar (Rudolf Virchow Center, Würzburg, Germany) has recorded the AFM data. The topography were analyzed by me with the software Gwyddion [124]. The lowest surface roughness for the gold coating was derived for a 20 nm gold coating (on 2 nm chromium, borosilicate glass BK7) for a deposition rate of 0.3 Å/s.

(a)

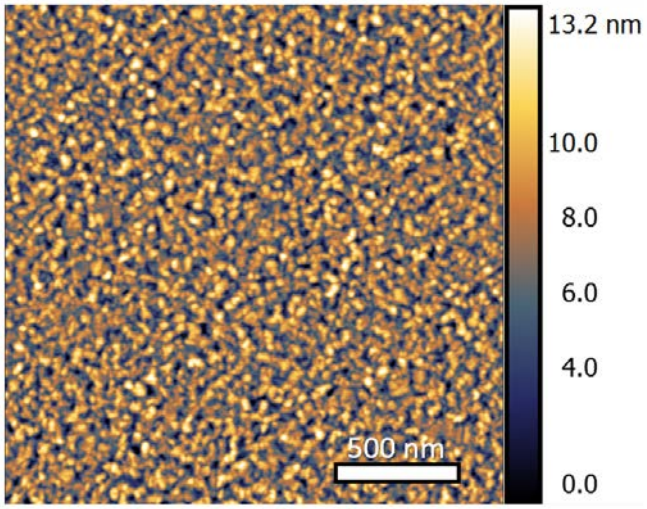

(b)

Coating	Roughness (rms)
Au 10 nm (0.1 Å/s)	(1.39 ± 0.09) nm
Au 30 nm (0.1 Å/s)	(1.66 ± 0.13) nm
Au 50 nm (0.1 Å/s)	(3.03 ± 0.16) nm
Au 20 nm (0.1 Å/s)	(1.34 ± 0.08) nm
Au 20 nm (0.2 Å/s)	(1.26 ± 0.06) nm
Au 20 nm (0.3 Å/s)	(1.18 ± 0.09) nm
BK7 Reference	(0.66 ± 0.05) nm

Table 2-2. (a) Example AFM measurement of gold (Au) coated glass substrate in Gwyddion. (b) Summarized results of surfaces roughness (rms values, 500 nm x 500 nm) analyzed for different gold coating thicknesses and deposition rates.

3.3 Home-built total internal reflection fluorescence microscopes (TIRF-M)

In this section, home-built total internal reflection fluorescence (TIRF) microscopy setups are described. The first setup is the Axicon-based ring illuminated TIRF-M and the second a computer-controlled variable-angle spinning-spot illuminated (VASi) TIRF-M. In this section, the information about the setups are summarized. In addition, the characterization method to derive the TIRF penetration depths is explained.

Axicon-based ring illuminated TIRF-M

The axicon-based TIRF-M is a home-built fluorescence microscope developed in the Dr. Kareem Elsayad's laboratory at the Vienna Biocenter. The setup description, characterization, and applications for homogenously flat-top illuminated TIRF microscopy are described in the publication Schreiber et al. “Axicon-based Bessel beams for flat-field illumination in total internal reflection fluorescence microscopy”[125] and can be found in the results part of this thesis. Here a full description of the illumination path is provided including photographs of the whole setup in figure 3-5 and a complete component list in table 2-3.

A fiber-coupled laser emits at 488 nm. The fiber is plugged into the home-built illumination system. The illumination system was built into a Thorlabs 30 mm cage system mounted on a vertically set breadboard. The Cobolt Monitor™ Software (Cobolt, Sweden) controls the laser excitation. A reflective fiber coupler leaves an 8 mm laser beam out of the fiber. A combination of wave plates polarizes generates a radially polarized laser beam. Two lenses expand this beam three times. A cone lens (axicon) radially separates the beam by deflection. At anular beam is filtered by an iris at the axicon focus point. A focus lens and a second axicon shape the laser to a ring and focus it on the back focal plane (BFP) of the TIRF objective lens. By three polarization maintaining mirrors (figure 3-5(c); M1-3) the laser ring is coupled into the microscope. The focus is aligned centrally at the BFP. To set the TIRF illumination angle, the second axicon is moved again the focus lens. The axicon to focus lens distance determines the diameter of the focus laser ring at the BFP. For calibration and ray trace calculations, please see the corresponding publication Schreiber et al. “Axicon-based Bessel beams for flat-field illumination in total internal reflection fluorescence microscopy” [125]. By the radially polarized ring illumination, a Bessel-beam like interference pattern is formed at the image plane. For overcritical oblique laser illumination, this interference pattern is built up from evanescent waves [37] and thus suitable to perform imaging in TIRF mode. We have shown, that this evanescent excitation field is suitable for homogenous TIRF imaging with a flat-top like illuminated field of view (FOV) [125]. The objective lens collects the fluorescence. A bandpass (BP) filters the fluorescence signal. A lens system, including the microscope tube lens and a 2.5x beam expander, focuses the florescence signal into an EMCCD camera. The Andor Solis software controls the EMCCD for fluorescence signal acquisition. Without pixel binning, one pixel is equal of 64 nm (given by the pixel size of the camera divided by the magnification).

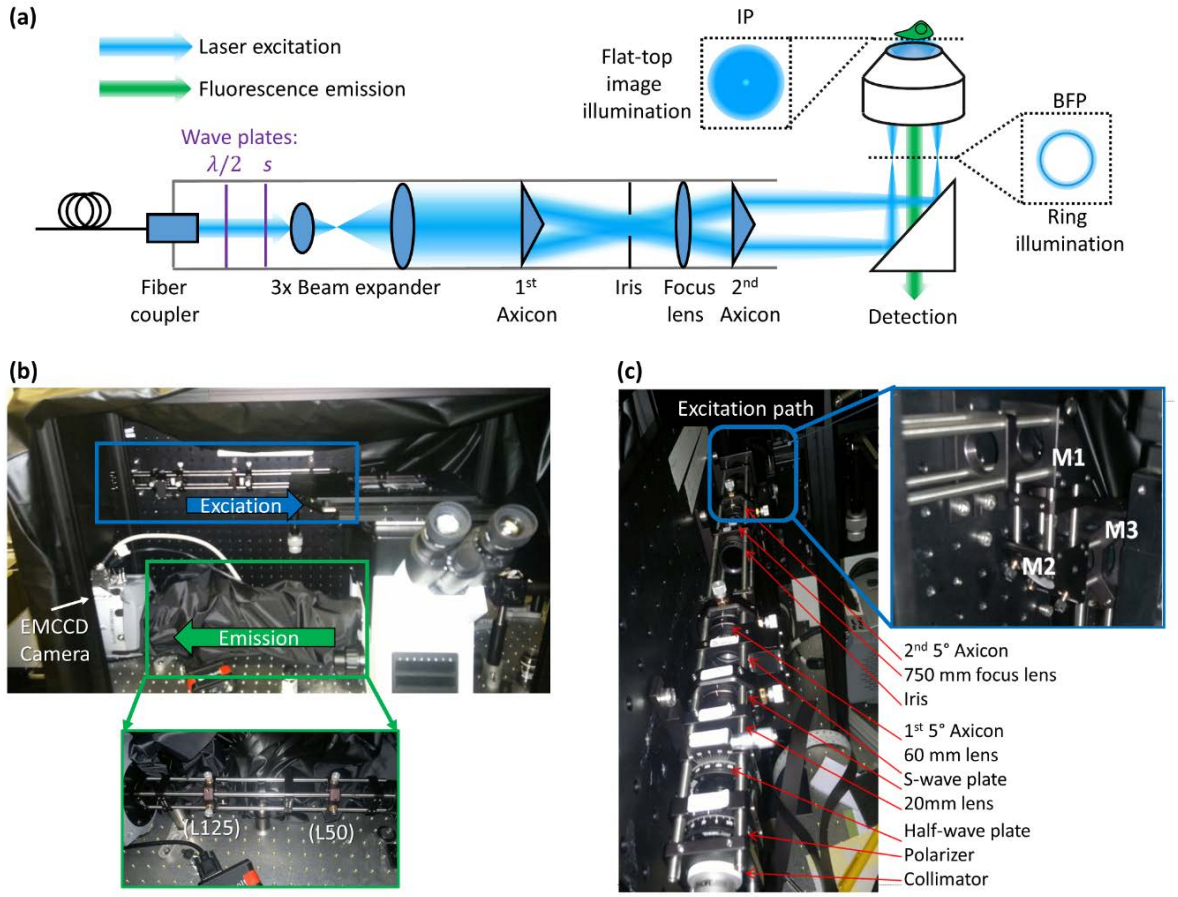

Figure 3-5. Axicon-based total internal reflection fluorescence (AxiTIRF) microscope at the Vienna Biocenter. (a) Illustration of the main components of the AxiTIRF-M setup. Focused laser ring at the objective lens back focal plane (BFP) and flat-top Bessel-beam like illumination pattern at the image plane (IP) are indicated. (b) Photograph of the home-built AxiTIRF setup at the Vienna Biocenter. Excitation and emission path (zoom in; telescope contains 50 and 125 mm lenses) are indicated. (c) Photograph of the excitation path with detailed component description. Mirrors M1-3 are used for precise coupling of the focused laser ring into the microscope.

Setup position	Component	ID	Distributor
AxiTIRF illumination beam path	488 nm fiber coupled (NA = 0.11) laser	06-MLD 488 nm	Cobol, Schweden
	Reflective collimator (8mm output)	RC08APC-P01	Thorlabs
	Linear polarizer	LPVISA100	Thorlabs
	Half-wave plate	AHWP05M-600	Thorlabs
	S-wave plate radial polarization converter	RPC-488-08	Altechna
	3X beam expander (f = 20 mm, 60 mm)	AC127-019-A-ML AC254-060-A-ML	Thorlabs
	Two 5° axicons	AX255-A	Thorlabs
	Focus lens f = 750 mm	LA1978-A	Thorlabs
	Iris	SM1D12C	Thorlabs
	Polarization maintaining dielectric mirrors	BB1-E02	Thorlabs
Microscope	Microscope corpus	IX73	Olympus
	TIRF objective lens; NA = 1.7	APON 100XHOTIRF	Olympus
	Beam splitter and bandpass fluorescence filter	F38-500 (BS 500) F37-516 (525/50)	AHF Analysentechnik
Detection	Telescope (f = 125 mm, 50 mm)	AC254-050-A AC254-125-A-ML	Thorlabs
	EMCCD camera	iXon^{EM} + DU-897D	Andor Technology Ltd.
Optics mounts/ cage parts	Cage system (30 mm) components	ERX, CP02/M, CP11/M, CPB1/M	Thorlabs
	X-Y translator for 1” optics	CXY1	Thorlabs
	X-Y translator for 1” optics; magnetic quick release for axicons	CXY1Q	Thorlabs
	Tip-tilt right-angle mirror mounts	KCB1C/M	Thorlabs
	Precision rotation mount for 1”optics	CRM1P/M	Thorlabs

Table 2-3. List of components installed in the AxiTIRF.

Variable-angel spinning-spot illuminated (VASi) TIRF microscope

The home-built VASi-TIRF-M is shown in figure 3-6. The setup is located at the Rudolf-Virchow-Zentrum of the University of Würzburg, and the scanning mirror illumination scheme is inspired by the publication of Ellefsen et al. “Spinning-Spot Shadowless TIRF Microscopy” [126]. The used components are listed in table 2-4 and illustrated as computer assisted design (CAD, FreeCAD) shown in figure 3-6(c-d).

In figure 3-6(b), the concept of the setup is shown. The heart piece of the VASi-TIRF microscope is the scanning mirror device arranged from two scan heads in 90° geometry. Both scan heads are controlled by an analog sinusoidal signal. The scan heads are controlled by a signal generator (NI-card) and the “Shadowless TIRF” Galvo Driver from Ellefsen et al. [126]. The excitation laser gets reflected by the scan heads resulting in an annularly spinning laser reflection. This ring-shaped spinning laser spot is focused by a focus lens onto the TIRF objective lens back focal plan (BFP). With increasing the analog signal amplitude (in volt), the mirror deflection and so the ring diameter and (TIRF) illumination increases.

The excited fluorescence is collected by the TIRF objective lens, filtered by a bandpass and detected by a camera (complementary metal-oxide-semiconductor (CMOS) type). Usually, the image is magnified by factor 1.6 using optics implement in the Olympus IX71 microscope. The laser spot spins with 400 Hz, what is several times faster than the camera acquisition speed. Because of this, during one camera acquisition, the sample is effectively all-sided illuminated. By this all-sided TIRF excitation, shadowing and fringe artifacts are significantly reduced while the image contrast is increased [47, 126, 127]. To reduce photobleaching of the sample, the camera and the acousto-optical tunable filter (AOTF) are synchronized. With this synchronization, the sample is just illuminated when the camera acquires. For this “fire” option, the “external” mode is enabled in the Andor Solis software to trigger the camera. Camera acquisition and illumination angle are controlled by the NI-card and Solis software, what allows the setup to perform as a variable angle (VA) TIRF microscope. By VA-TIRF a stack of TIRF images is taken for different penetration depths. By comparison of the image features of different penetration depths, an axially super-resolved 3D TIRF image is constructible [128-130].

The here presented VASi-TIRF-M was used for data acquisition in the publication Schreiber et al. “Live cell fluorescence imaging with extreme background suppression by plasmonic nanocoatings”, as shown in the results part of the thesis. The VASi-TIRF was used to sweep the illumination angle to find the surface plasmon resonance (SPR) angle.

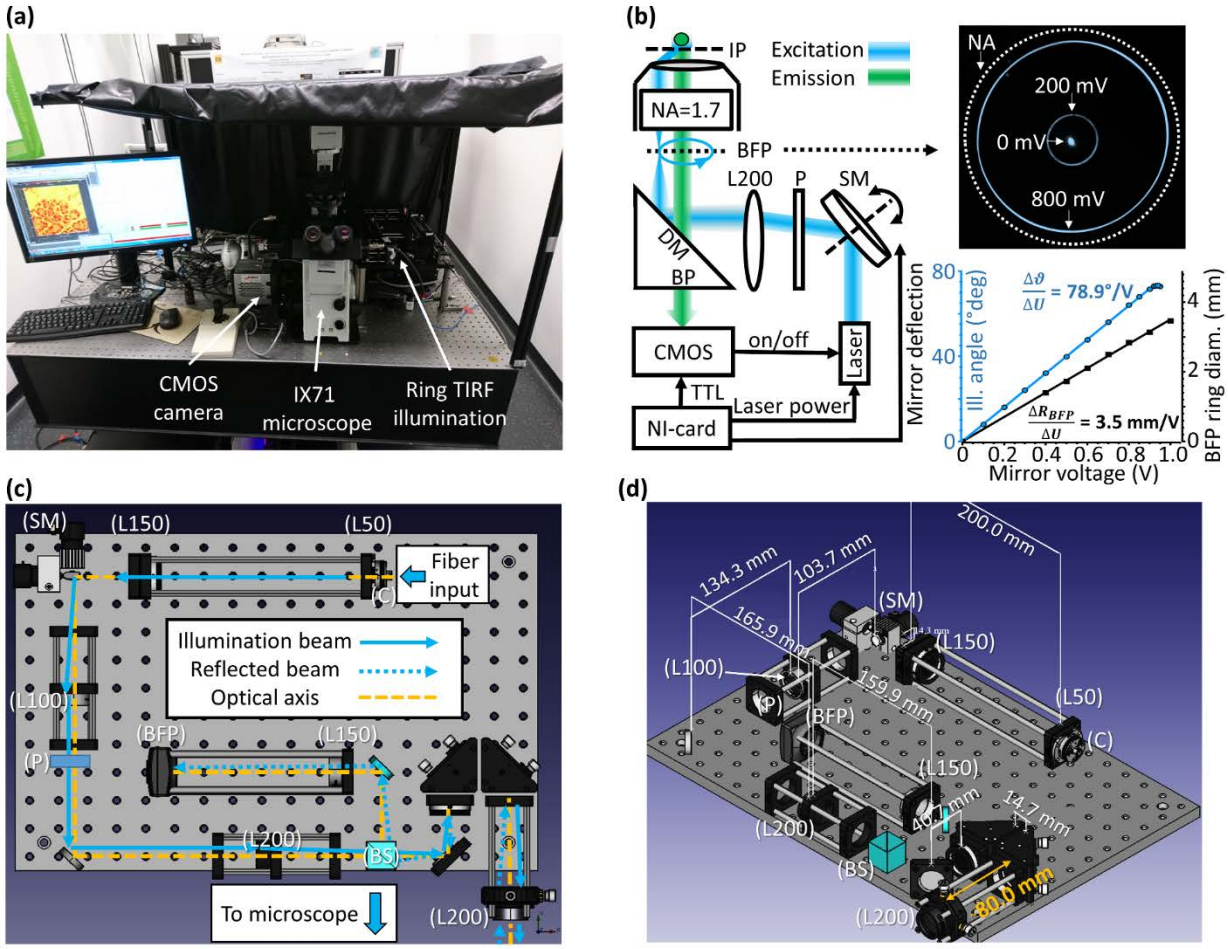

Figure 3-6. Home-built variable-angle spinning-spot illuminated (VASi) TIRF setup at the Rudolf-Virchow-Zentrum, Würzburg. (a) Photograph of the TIRF setup. (b) Illustration of the components and electronic control of the setup. Optical components are a laser, a scanning mirror (SM), a polarizer (P), and a 200 mm focus lens (L200). By the SM generated annular spinning-spot (or ring) is focused at the back focal plane (BFP) of the NA = 1.7 TIRF objective lens. Fluorescence from the image plane (IP) is collected by the objective, filtered by a bandpass (BP) and detected by a CMOS camera. The national instruments computer card (NI-card) controls mirror deflection, laser power by analog signals and triggers the CMOS camera by TTL pulses. The externally triggered CMOS camera is synchronized with the laser box and switches on/off the laser excitation ("fire" mode). With a camera collecting back reflection from the BFP, the alignment is controlled. The photograph inset shows the back reflected ring illumination for three different SM voltages. The corresponding angle over mirror voltage calibration curve is shown below. (c-d) Computer assisted design (CAD) of the illumination path. Corresponding optical components are labeled: LX (achromatic lenses, X = focus length), scanning mirror (SM), polarizer (P), beam splitter cube (BS) and back focal plane imaging camera (BFP). Beam paths, optical axis, components distances are indicated.

Setup position	Component	Manufacturer ID	Distributor
Laser box	640 nm laser	Obis 640nm LX40mW	Coherent
	473 nm laser	unknown	unknown
	Dichroic mirror	DMLP505	Thorlabs
	Acousto-optical tunable filter (AOTF)	AOTFnC-Vis-HR7-TN	AA Opto Electronic
	Achromatic fiber port coupler	PAF2-A4A	Thorlabs
	Pol. maintaining single mode fiber	PM-S405-XP	Thorlabs
	Encapsulation	AD18	A. Hartenstein
Spinning ring TIRF illumination beam path	(C) Fiber output coupler	PAF2-A4A	Thorlabs
	(L50), (150) 3X Beam expander (focus lengths: 50 and 150 mm)	AC254-050-A AC254-150-A	Thorlabs
	(SM) Scanning mirror galvanometer XY	62xxH series	Cambridge Technologies
	(L100), (200) 2X beam expander (focus lengths: 100 and 200 mm)	AC254-100-A-ML AC254-200-A-ML	Thorlabs
	(P) polarization optics (optional): Half-wave plate Quarter-wave plate S-wave plate	 AHWP05M-600 AQWP05M-600 RPC-632-10	 Thorlabs Thorlabs Altechna
	Focus lens f = 200 mm	AC254-200-A-ML	Thorlabs
	Iris	SM1D12C	Thorlabs
	Pol. maintaining diel. mirrors	BB1-E02	Thorlabs
BFP Imaging	(BS) 10:90 (R:T) Non-polarizing beam splitter cube	BS025	Thorlabs
	(L150) 150 mm lens	AC254-150-A	Thorlabs
	(BFP) USB 2.0 CMOS camera	DCC1545M	Thorlabs
Microscope	Microscope corpus	IX71	Olympus
	Objective lenses; NA = 1.7_(100x) NA = 1.4 (100x) NA = 0.4 (20x)	APON 100XHOTIRF UplanSApo 100x LD AchroPlan 20x	Olympus Olympus Zeiss
	Polarization maintaining laser line reflector	F73-421PH	AHF Analysentechnik
Detection	Light-tight bandpass filter holder	CFH2/M, CFH2-F	Thorlabs
	Bandpass emission filters for green and deep red fluorescence	F37-516 (525/50) F73-697 (697/58)	AHF Analysentechnik
	CMOS camera	Andor Neo DC-152Q-CRO-F1	Andor Technology Ltd.
Optics mounts/ cage parts	Cage system (30 mm) components	ERX, CP02/M, CP11/M, CPB1/M	Thorlabs
	x-y translator for 1” optics	CXY1	Thorlabs
	Tip-tilt right-angle mirror mounts	KCB1C/M	Thorlabs
	Precision rotation mount for 1”optics	CRM1P/M	Thorlabs
Electronic control	NI-card as signal generator for laser, camera and galvanometer controlling	PCI-6733	National Instruments

Table 2-4. List of components installed in the VASi –TIRF-M.

Evanescent field characterization

The evanescent TIRF field can be characterized with fluorescent beads [131]. For this purpose, outer shell coated beads with a diameter of 6 µm to 10 µm are ideal. In this thesis, I used 6 µm FocalCheck™ Microspheres beads (Invotrogen, F14808) for green fluorescence and for deep red fluorescence (Invotrogen, F14806). The beads were diluted one to ten in ultra-pure water. A drop of 20 µl was placed on a poly-D-lysine coated coverslip. After 10 to 20 minutes, the bead density was checked in the microscope. If the bead occupation is satisfactory, the sample was washed with ultra-pure water, and a wat drop is added to simulate an aqueous environment. Now the beads can be used for TIRF calibration. Alternatively, bead samples can be mounted in Mowiol (Sigma-Aldrich, Mowiol 4-88). For this case, NLAFN-21 coverslips and the NA = 1.7 objective lens should be used to achieve TIRF in Mowiol mounted samples. The fluorescence signal of TIRF calibration bead samples was measured under different illumination angles ϑ. The intensity and axial penetration depth δ are dependent from the illumination angle. When exceeding the critical angle, an evanescent field forms in the axial direction. Further increasing the illumination angle reduces the penetration depth. Because of the bead geometry, a reduced penetration depth reduces the effective illuminated area of the bead. The radius r of the measured fluorescent area and the bead radius R determine the penetration depth:

$$\delta = R - \sqrt{R^2 - r^2} \qquad \text{(Eq. 2-9)}$$

Figure 3-7 shows an illustration of the method and a corresponding characterization of the home-built VASi TIRF-M. For this TIRF characterization, the high NA = 1.7 objective lens is used. The measurement was performed on a coverslip (NLAFN-21)/Mowiol interface with 6 µm green fluorescent beads.

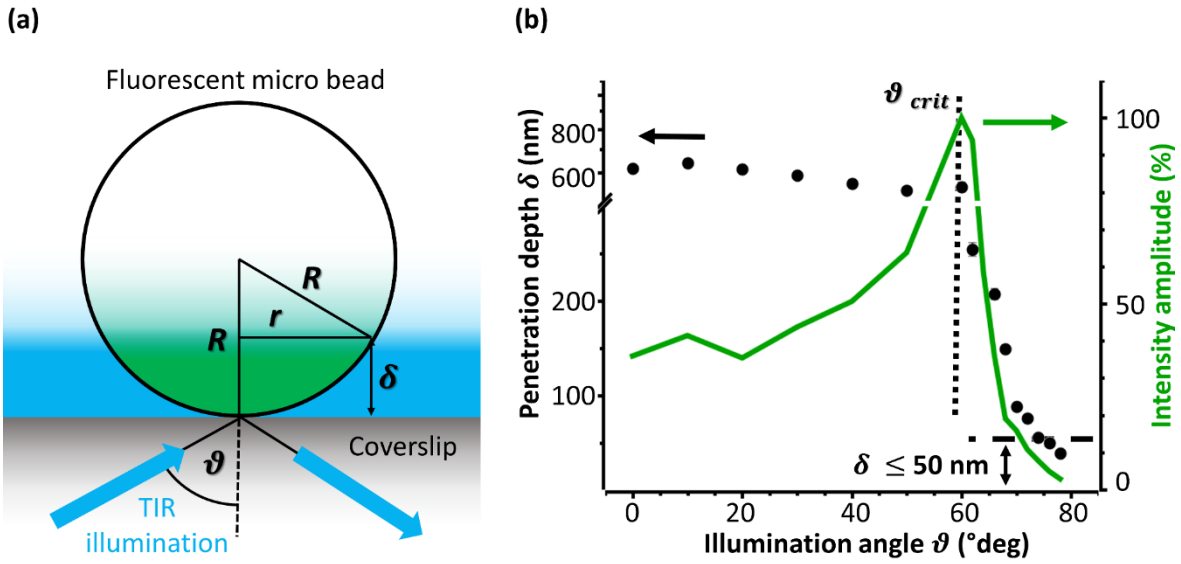

Figure 3-7. (a) Illustration of evanescent field characterization with fluorescent micro beads attached on a coverslip surface. The TIR illumination angle ϑ, the penetration depth δ, bead diameter (R) and effective illuminated bead radius (r) are indicated. (b) Example of an illumination angle-dependent characterization of the penetration depth and the bead intensity amplitude. Measurement was performed for a six µm green fluorescent bead on NLAFN-21 coverslips embedded in Mowiol in the VASi TIRF-M.

3.4 Cell culture, immunostaining, and FRET-constructs

Cell culture and immunostaining of Chinese hamster ovary (CHO) cells

Wild-type CHO cells were cultured at 37°C and 5% CO2 in Dulbecco's Modified Eagle Medium (DMEM/F12). Cells were seeded on coverslips in a six-well chamber with a typical cell number of 200.000 per chamber. After 24 hours, the cells are suitable for immunostaining. Used materials for cell culture and immunostaining are listed in table 2-5. If not otherwise indicated, typically a volume of 600µl is used for any washing or labeling step.

Plasma membrane staining

CellMask is used for plasma membrane staining of living cells. For this 1µl CellMask is diluted in one milliliter of phenol red-free imaging buffer (DMEM/F-12, no phenol red) for staining one cell sample. The protocol is identic with the manual provided by Thermofischer Scientific [132] unless otherwise stated. The protocol is:

- Wash the cells three times with phenol red-free medium
- Medium is removed, and CellMask is containing buffer is added. The sample is placed for 10 minutes in the incubator.
- Wash the cells three times with phenol red-free medium or PBS

Now the samples can be used for live cell imaging. In addition, stained cells can be fixed by paraformaldehyde (4% PFA in PBS, 5-10 minutes at room temperature or 37°C) and mounted in Mowiol.

F-actin labeling

F-actin is a protein of the microfilaments of the cytoskeleton. For f-actin labeling of fixed cells, Alexa dye conjugated Phalloidin is used. The staining protocol is:

- Wash cells three times by PBS
- Fix cells with 4% PFA in PBS for around 15 minutes at room temperature
- Permeabilize cells with 1% Triton X-100 in PBS for 3-5 minutes
- Block unspecific binding by 5% BSA and 0.1% Triton X-100 in PBS for 15 minutes
- Stain the samples with Alexa Phalloidin conjugates for 30 minutes (stock solution is diluted 1:200 in PBS)
- Wash sample three times by PBS

Afterwards, the sample can be used for imaging. In addition, the cells can be mounted in Mowiol.

Muscarinic M1 receptor with FRET sensor

The used muscarinic M1 receptor contains two fluorescent molecules. A cyan fluorescent protein (CFP) and a fluorescein arsenic hairpin binder-ethanedithiol (FlAsH-EDT_2). The construct was developed by the group of Prof. Dr. Carsten Hoffmann [21] (intra-group name M1-I3N-CFP). M1-I3N-CFP stands for the M1 muscarinic receptor with labeling position for FlAsH in the 3rd intercellular loop and CFP at the N-terminal end of the protein. Details of the receptor and the construct sequence are described by Messerer et al. [24].

The cell culture of a stabile HEK-293 cell line (where M1-I3N-CFP is expressed), FlAsH labeling and FRET experience were performed by Michael Kauk. The protocols for cell culture, labeling and FRET experiments can be found in the publications [23, 24, 133]. The FRET measurements were performed by the recording of the donor-to-acceptor fluorescence intensity ratios, see for example the publication Schreiber et al. [133]. For chemical bleaching experiments, 1,2-dimercapto-1-propanol (British Anti-Lewisite, BAL) were used in a final concentration of 5 mM. The group of Prof. Dr. Ulrike Holzgrabe kindly provided us Iperoxo.

Material	Manufacturer	Catalogue number (July 2018)
Six-well chamber Nunc™	Thermo Scientific	140675 (TF)
cell culture medium: DMEM/F12	Gibco	11320033 (TF)
cell culture medium: DMEM/F12, no phenol red	Gibco	11039-021 (TF)
PBS (1x)	Gibco	1419-094 (TF)
Triton-X 100	Sigma-Aldrich	9002-93-1(S-A)
BSA (Bovine serum albumin)	Sigma-Aldrich	9048-46-8 (S-A)
CellMask Green	Invitrogen	C37608 (TF)
CellMask Deep Red	Invitrogen	C10045 (TF)
Alexa Flour 647 Phalloidin	Invitrogen	A22284 (TF)
Alexa Flour 488 Phalloidin	Invitrogen	A12379 (TF)
Mowiol 4-88	Sigma-Aldrich	9002-89-5 (S-A)

Table 2-5. List of used materials for cell sample preparation. The abbreviations (TF) and (S-A) stands for the distributors Thermofischer Scientific and Sigma-Aldrich, respectively. Coverslip preparation is described in the methods section "Fabrication and characterization of nanocoated coverslips".

4 Results

4.1 Axicon-based Bessel beams for flat-field illumination in total internal reflection fluorescence microscopy

The content of this chapter has been published:

Benjamin Schreiber, Kareem Elsayad, Katrin G. Heinze, „Axicon-based Bessel beams for flat-field illumination in total internal reflection fluorescence microscopy“, Optics Letters 42, 2017 [125]

https://doi.org/10.1364/OL.42.003880

Summary and contribution:

TIRF-M is based on oblique sample illumination which is standardly realized with a single laser spot. This one-sided illumination can evoke unwanted shadowing and interference effects. Here we show a new approach to TIRF illumination. A combination of two cone lenses (Axicon) and a focus lens creates a laser ring for a 360° TIRF illumination. We show that a Bessel function like interference pattern is formed at the image plane of the microscope. With this flat-top like illumination method, artifact reduced and homogenous TIRF imaging over the whole field of view is achieved. This method was developed by myself during a research stay (June to December 2016) in Dr. Kareem Elsayad's laboratory at the Vienna Biocenter. All data shown was recorded and analyzed by myself. Prof. Dr. Katrin G. Heinze and Dr. Kareem Elsayad supervised the work and contributed to manuscript writing, and the revision process of the manuscript.

Axicon-based Bessel beams for flat-field illumination in Total Internal Reflection Fluorescence (AxiTIRF) Microscopy

BENJAMIN SCHREIBER,[1,2] KAREEM ELSAYAD,[2] KATRIN G. HEINZE[1*]

[1]*Rudolf Virchow Center, Research Center for Experimental Biomedicine, University of Würzburg, Josef-Schneider-Str.2, 97080 Würzburg, Germany*
[2]*Advanced Microscopy Facility, Vienna Biocenter Core Facilities, Dr. Bohr-Gasse 3, A-1030 Vienna, Austria*
**Corresponding author: katrin.heinze@virchow.uni-wuerzburg.de*

Received 31 July 2017; revised 31 August 2017; accepted 1 September 2017; posted 6 September 2017 (Doc. ID 303364); published 25 September 2017

Abstract: Total internal reflection fluorescence (TIRF) microscopy provides low-invasive high-contrast surface imaging with optical-sectioning of typically 100-200nm. Thus, TIRF microscopy (TIRF-M) has become an established tool for imaging surfaces including cell membranes. For TIRF-M a homogenous evanescent field of excitation over the whole field of view is generally desired for quantitative microscopy, however not necessarily straight forward to generate when Gaussian beams. In recent years, several improvements on TIRF-M have been developed, which have addressed non-uniform scattering fringes and other artifacts. Here, we introduce a cost-effective TIRF setup with a very low degree of complexity and no moving parts that provides a flat-top like excitation profile. The setup uses a tunable laser ring zoom focus system to generate a full 360° TIRF illumination. Two axicon lenses and one focus lens allow for generation and control of the ring diameter to tune the TIRF excitation angle. We show that 360° laser illumination in combination with a radial polarizer will generate an evanescent Bessel-beam excitation field that exhibits a flat-top intensity over an extended part of the field of view, and demonstrate the advantages of this axicon-based Bessel beams illumination (AxiTIRF) for live-cell imaging.

OCIS codes: *(170.2945) Illumination design; (110.0180) Microscopy; (180.2520) Fluorescence microscopy; (260.6970) Total internal reflection*

https://doi.org/10.1364/OL.42.003880

Total internal reflection fluorescence (TIRF) microscopy has become a key technique in the life sciences and allows for fast high-contrast fluorescence imaging in the cell membrane region. Fluorescent dyes in close vicinity (up to few hundred nanometers) to the microscopy cover slip interface are selectively excited by an evanescent field. The steep exponential axial intensity decay prevents out-of-focus fluorescence excitation [64]. Focusing a single Gaussian laser beam off-centered onto the objective back focal plane (BFP) is the most common way to achieve an evanescent excitation field in TIRF microscopes [134]. This results in an inevitable and generally undesirable lateral asymmetry of the excitation field which can hardly be avoided in this otherwise elegant and simple approach, as the single laser beam has to be focused at the periphery of the objective rear aperture to ensure overcritical angle illumination. Since homogenous excitation over the whole field of view (FOV) is crucial for many application several TIRF improvements have been developed over the last century. Popular approaches for enhanced field homogeneity are based on 360° incoherent illumination [47, 135], variable-angle TIRF (VATIRF) [136], and spinning TIRF (sp-TIRF) [137-139]. Such approaches result in a radial symmetric Gaussian illumination field for TIRF microscopes and suppress shadowing and TIRF fringes artifacts caused by one sided illumination. To achieve a homogenous flat-top illumination

field the combination of single and multimode fibers [140] or micro-lens arrays [141] can be used. Those allow a flat-field homogenous epi-fluorescence wide-field illumination with great potential to improve single molecule imaging. Unfortunately, these flat-field approaches have not been applied to TIRF-M.

Our work presented here closes this gap as we introduce an objective-based homogeneous TIRF illumination using Bessel-beam side lobes. Bessel beams have become highly desired and well-studied microscopy tools as they concentrate a large amount of laser intensity in a sub-diffractive limited laser spot [142]. Bessel-beam illumination is well known in the fluorescence microscopy community for decades and has been successfully implemented in Structural Illumination and Light-Sheet Microscopy [143-145]. For our approach a radial symmetric evanescent field is formed at the microscopy coverslip-sample interface by 360° overcritical p-polarized illumination. Focusing a radially polarized laser ring at the TIRF objective back focal plane (BFP) ensured all-sided p-polarization. The resulting intensity distribution in the image plane is described by a squared zero order Bessel-function with an exponential intensity decay in axial direction [146]. It has been previously shown that the resulting evanescent subdiffraction limited spot can be used for single spot TIRF-STED-FCS [147]. In this work, we demonstrate that Bessel-beam side lobes also have potential for homogenous and flat-top-like TIRF illumination.

Figure 4-1 shows finite element method calculations (*COMSOL Multiphysics 4.4*) for a typical single spot Gaussian illumination (a) and radially polarized 360° Gaussian ring illumination (b) for an excitation wavelength of 488nm and an illumination angle of 63°. The corresponding maximum normalized intensity distributions at the glass/sample interface (RI = 1.52/1.33) is plotted below (c). Note, the x-axis in (c) was normalized to the excitation wavelength and beam diameter of 10µm.

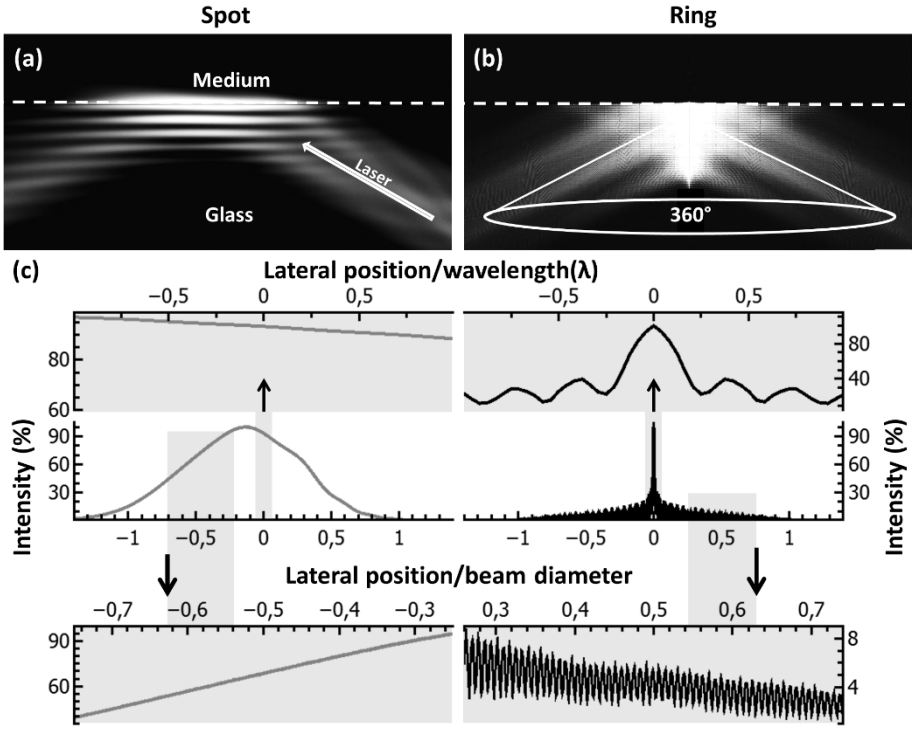

Fig. 4-1. Finite elements method calculations for single spot Gaussian (a) and 360° ring TIR illumination (b). Corresponding lateral intensity cross-sections at the glass to medium interface (c). The middle row shows cross-section overviews. Gray boxes indicate corresponding regions of interest and zoom-in at the center region (top) and at the side-lope region (bottom) as indicated.

The overcritical single spot illumination shows the typical Gaussian behavior. As expected, only at the center of the FOV the intensity distribution is homogenous. It is this relatively small area that is typically used in TIRF-M and spectroscopy. This area can be extended by the size of the incoming laser beam if reduced laser intensity is experimentally acceptable. The rest of the lateral excitation field is noticeably asymmetric along the direction of the excitation beam and the maximum intensity is shifted from the center of the focus. This is caused by the illumination angle tilted projection of the incoming Gaussian beam. Thus, for Gaussian illuminated side areas the intensity drops from the higher center area to the background level, which is challenging when quantitative imaging and/or low-light applications have to be performed.

On the contrary, a 360° radially polarized laser excitation results in evanescent illumination, and a radial-symmetric zero-order Bessel-function in lateral plane [146]. Radially polarization ensures that the radial symmetric evanescent field is fed by all-sided p-polarized illumination. Figure 4-1(b) shows respective illumination simulations with corresponding intensity line plots panel (c, right). Here, the Bessel-beam center exhibits the typical sub diffractive intensity spot with a FHWM of 0.32λ and the first intensity minimum at 0.26λ. The Bessel-beam side lobes show an interference pattern with a shallower radial intensity gradient than in the Gaussian case. The simulations demonstrate the potential of evanescently generated Bessel-beams for improved objective-based TIRF-M. We favor an objective-based configuration as this is often advantageous in cell imaging compared to the prism based TIRF-M: In the objective-type method, the specimen is well accessible, and the angle of incidence of the laser light can be changed easily.

Figure 4-2 shows the experimental setup (a) and calibration (b-c) to generate a 360° ring illumination in our TIRF-M. The illumination part of the setup is largely inspired by Dickey and co-workers annular laser ring zoom system [148] with several important variations. The illumination profile is generated by the use of axicons (cone lenses) and a focus lens. More specifically, a first axicon (Ax1) forms the laser ring, which is subsequently focused by the focus lens (FL). A second axicon (Ax2) then neutralizes the deflection of the laser beam and determines the ring diameter of the laser ring zoom system. The ring diameter control of the laser focused at the objective lens BFP is the crucial feature to finally control the TIR illumination angle.

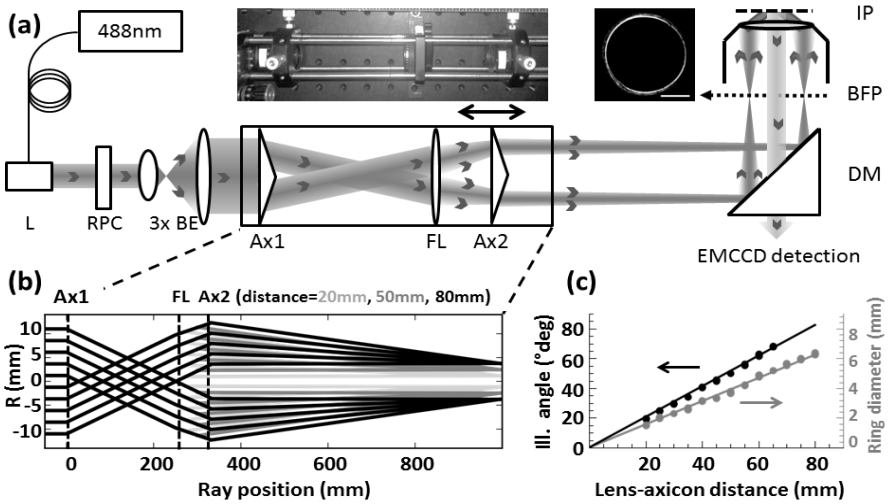

Fig. 4-2. AxiTIRF-M with laser ring focus system. Illustration of optical design (a) with photograph (middle) and the inset image of the laser ring back reflection (right, scale bar 2mm) inset. Main optical components are laser L, radial polarization converter (RPC), Beam Expander (BE), two axicons (Ax1 & Ax2), focus lens (FL), and a dichroic mirror (DM). Objective back focal and image plane (BFP and IP) are indicated. Ray traces of AxiTIRF-M for 20mm, 50mm and 80mm lens-axicon distances (b). Measured illumination angle and ring diameter (at BFP) (c) depending on lens-axicon distance.

In our setup two 5° axicon lenses (AX255-A, Thorlabs) and a focus lens (f = 750mm, LA1978-A, Thorlabs) are used to control this. First, a single mode fiber (NA 0.11) coupled laser diode (06-MLD 488nm, Cobolt) with a reflective collimator (RC08APC-P01, Thorlabs) was used to create an 8mm laser output. The beam was then passed through a radial polarization converter (RPC) consisting of a $\lambda/2$ waveplate (AHWP05M-600, Thorlabs) and s-waveplate (RPC-488-08, Altechna) generating a radially polarized laser beam. A beam expander (3x) optimized the performance of the first axicon in the AxiTIRF-M. Note, the first axicon and the focus lens are separated by 250mm (see Fig. 4-2(b)). The resulting radially polarized laser ring is focused at the TIRF Objective BFP. A dichroic mirror (Beamsplitter HC BS 500, *AHF* Analysentechnik) was used for light filtering and coupling to the microscope stand (IX73, Olympus), which was equipped with a TIRF Objective (APON 100XHOTIRF, Olympus, NA: 1.7) suitable for TIR illumination and fluorescence collection. AxiTIRF imaging can also be obtained with standard TIRF objectives. Here, we used the NA 1.7 objective to allow TIRFM in Mowiol mounted samples where the refractive index difference to glass is usually not sufficient to perform TIRFM with more common (NA~ 1.49) TIRF objectives. This optical layout allows for a theoretical FOV of 28.8µm. For direct comparison with single spot illumination, the axicons can be removed from the light path and replaced by a tiltable glass plate (thickness: 10mm) to laterally displace the focus at the BFP. An iris diaphragm ensures a comparable total FOV for single spot and ring illumination. The collected fluorescence is filtered by a bandpass (525/50, *AHF* Analysentechnik) magnified by 2.5x and focused onto an EMCCD (iXon EM+ DU-897D, Andor Technology Ltd.).

Figure 4-2(b) shows two dimensional ray trace calculations of the realized AxiTIRF-M with lens-axicon separations of 20mm, 50mm and 80mm. By separating the lens-axicon the diameter of the laser ring focus increases linearly (see Fig. 4-2(c)). Linear fitted slopes for ring diameter and illumination angle over the lens-axicon distance are 0.039 and 1.03(°/mm). Penetration depths of the setup were determined by 6µm FocalCheck Microspheres (F14808, Invitrogen, for the method see e.g. [149]).

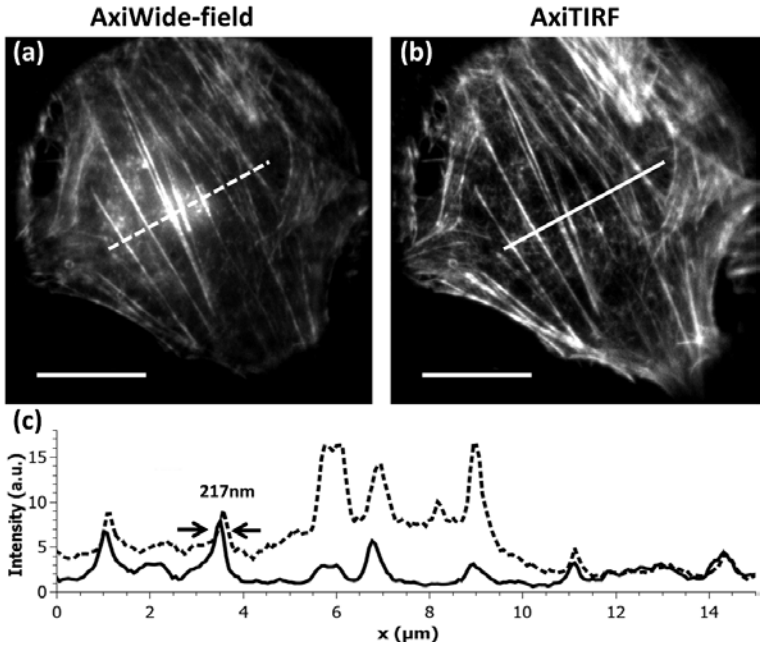

Fig. 4-3. Comparison of ring illuminated AxiWide-field (a) and AxiTIRF images (b) of A488-Phalloidin labeled CHO cells. Corresponding fluorescence intensity cross-sections (c). Scale bars: 10 µm.

Next, we demonstrate AxiTIRF-M for fluorescent imaging of cells. The cells were stained for actin filaments (f-actin) fluorescently labeled with AlexaFluor488 (A488)-Phalloidin (Invitrogen). Wild-type Chinese hamster ovary (CHO) cells were cultured at 37°C and 5% CO2 in Dulbecco's Modified Eagle Medium (DMEM/F12, Thermofischer). Cells were grown and seeded on high refractive index (RI = 1.78) NLAFN-21 cover slips (150 µm thick, UQG Optics Ltd.). Note, a high refractive index cover slips were used to even allow for TIRF imaging of Mowiol-mounted cells; respective live cell experiments would not require special coverslips. Before imaging, cells were paraformaldehyde fixed (4%) for 10 minutes, permeabilized by 1% Triton X-100 (Sigma-Aldrich) for 5 minutes and stained with A488-Phalloidin (1:200) for 30 minutes at room temperature and mounted in Mowiol 4-88 (Sigma-Aldrich). For imaging a laser (Cobolt 06-MLD 488nm, set laser power: 0.4mW continuous wave emission) and an EMCCD camera were used (gain: 300; exposure time: 100ms). For AxiTIRF imaging, a lens-axicon distance of 67° to 72° incident angle (corresponding to lens-axicon distances of 65mm to 70mm) was found to be optimal and used in all cell experiments. The measured effective excitation penetration depth was 220nm ±30nm.

Figure 4-3 shows cell images for wide-field (a) and conventional TIRF mode (b). The corresponding fluorescence intensity line plot is plotted in (c). For a small ring diameter (lens-axicon distance = 20mm) cells are illuminated in wide-field mode [see Fig. 4-3(a)]. With increasing the lens-axicon distance the illumination angle finally overcomes the critical angle for proper TIRF illumination [see Fig. 4-3(b)]. As expected the wide-field image shows out-of-focus fluorescence background, particularly in the center of the FOV while in overcritical TIRF illumination, out-of-focus background in this center area and beyond is reduced (see Fig. 4-3(c)). For a selected actin filament a full width half maximum of 217nm was measured to estimate the lateral resolution of the setup.

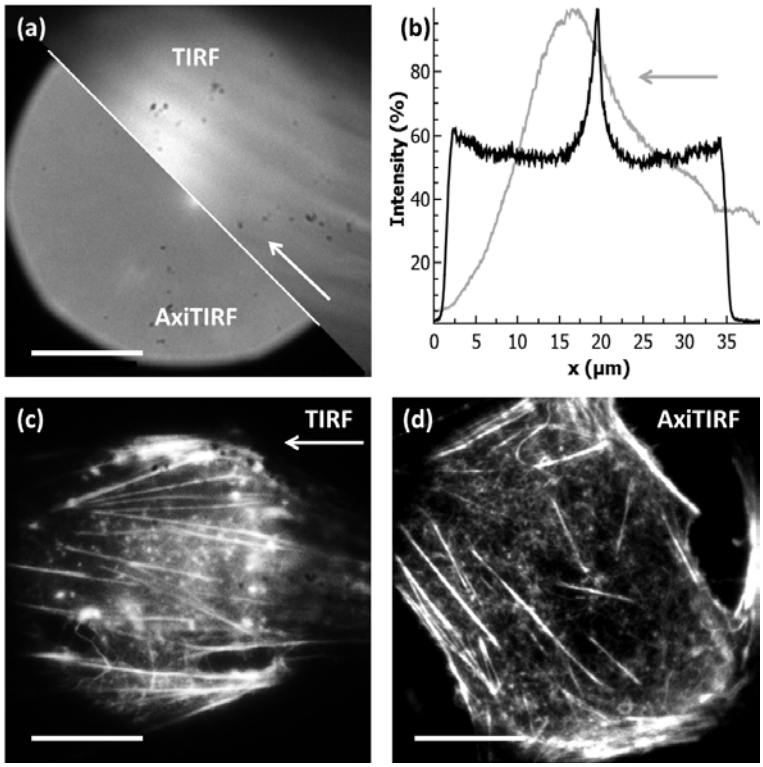

Fig. 4-4. A488 dye solution (a) imaged for direct single spot TIRF and AxiTIRF illumination field comparison with corresponding fluorescence intensity cross-sections (b). Comparison of single spot TIRF (c) and AxiTIRF-M images (d) of A488-Phalloidin labeled CHO cells. Arrows indicate the direction of single spot illumination. Scale bars: 10µm.

Next, we compare single spot Gaussian TIRF-M and AxiTIRF-M (see Fig. 4-4) for both 1µM A488 dye solution (a) with the corresponding line scans plotted in (b). Images of CHO cells stained for A488-Phalloidin (see above) are shown in (c-d). For AxiTIRF-M a symmetric flat-top-like illumination with the zero order center spot is achieved. In contrast, the single spot illumination follows the classical Gaussian distribution with its asymmetry due to the static excitation direction (see arrows in Fig 4-4(a) and (c). The measurements are in good agreement with finite element method calculations shown in Fig. 4-1. For the cell images, we note a background suppression in both classic and AxiTIRF-M, however, there is one striking difference: For single side illumination the images show an asymmetric and inhomogeneous intensity distribution, and effectively exhibit three subareas: First, the well illuminated middle part, second, a fast decaying shoulder at the opposite side of the illumination direction, and, third, a slower decaying shoulder at the excitation side. Consequently the classic TIRF image is dimmer at the periphery with the most pronounced effects at the side furthest from illumination direction. In contrast the AxiTIRF-M image in Fig. 4-4(d) is homogeneously illuminated with an effectively increased FOV (26.2 ± 0.12 µm for TIRF-M derived from Gaussian fit with linear background, and 31.2 ± 0.1 µm for AxiTIRF-M derived from plateau width).

Note, for the cell sample, we could neither observe a clear bright center peak nor any disturbing Bessel beam side lobes, most likely due to regular (elastic/Rayleigh) scattering and loss of coherence (and this vanishing interference), that feeds the Bessel-beam spot. Another reason may be due to the inhomogeneity of the sample [150] or cover-slip-sample interface which may smooth the interference effect. In Fig. 4-4(a) we noticed some weak shadowing stripes aligned radially to the illumination center. Excitation through a multi-mode fiber may allow for suppression of such weak interference patterns [135], however may compromise the sharp Bessel form formation.

In conclusion, we have shown that an axicon-based laser ring focused on a TIRF objective back focal plane can be used for TIRF-M with added value. The resulting Bessel beam effectively enlarges the FOV and provides a homogeneous TIRF illumination in a cell-friendly objective-based setup. The laser ring diameter can be easily adjusted by moving one lens along the optical axis, which allows for switching between wide-field and TIRF mode. AxiTIRF-M increases the effective FOV in comparison to classic TIRF-M by almost a factor of two as the radial polarized laser ring generates an evanescent flat-top illumination around a narrow center spot. Thus, the FOV for AxiTIRF-M becomes remarkably big compared to standard single spot Gaussian illumination where just a few percent of the central area is homogenously illuminated.

We believe that the illumination scheme of AxiTIRF-M has great potential for single molecule tracking and localization applications where a homogenous illumination over few µm FOV is desirable. Since the illumination strategy is based on a radial symmetric illumination we can imagine that this ring illumination could also have potential for TIRF structured illumination microscopy when the laser ring is chopped into two segments with a rotatable slit mask. As discussed by Chung et al. [151] even more pairs of interfering laser beams can be used for SIM-TIRF with an increased PSF symmetry. With some additional tweaks, the setup described here is also potentially suitable for 360° incoherent illumination which would further suppress TIRF fringes and would allow for even shadow-less TIRF-M.

4.2 Live cell fluorescence imaging with extreme background suppression by plasmonic nanocoatings

The content of this chapter has been accepted for publication in Optics Express:

Benjamin Schreiber, Hannah S. Heil, Martin Kamp, Katrin G. Heinze, „Live cell fluorescence imaging with extreme background suppression by plasmonic nanocoatings“, Optics Express 26(15), 2018

Summary and contribution:

For high-content imaging of the basal membrane, TIRF-M is usually the method of choice. Unfortunately, auto-fluorescence, light scattering and not perfect labeling efficiencies often lead to detection of unwanted out-of-focus fluorescence. To overcome this limitation, we implemented gold-nanocoated coverslips in a TIRF-M. The coating acts as an axial light filter which blocks out-of-focus fluorescence reaching the detection path. We prove this by computational simulations and in experiments. We could perform high-contrast TIRF-M basal membrane imaging of living cells even with four times higher fluorescent background, compared to what is possible with standard coverslips.

I have developed the imaging setup, fabricated the nanocatings, performed the experiments and analyzed the data. Hannah S. Heil designed and synthesized DNA-oligomers. Prof. Dr. Katrin G. Heinze and Dr. Martin Kamp conceived and designed the experiments. Prof. Dr. Katrin G. Heinze and I wrote the manuscript.

Live cell fluorescence imaging with extreme background suppression by plasmonic nanocoatings

BENJAMIN SCHREIBER,[1] HANNAH S. HEIL,[1] MARTIN KAMP,[2] AND KATRIN G. HEINZE[1*]

[1]*Rudolf Virchow Center for Experimental Biomedicine, University of Würzburg, Josef-Schneider-Str.2, 97080 Würzburg, Germany*

[2]*Technische Physik, University of Würzburg, Am Hubland, 97074 Würzburg, Germany*

[*]*katrin.heinze@virchow.uni-wuerzburg.de*

Abstract: Fluorescence microscopy allows specific and selective imaging of biological samples. Unfortunately, unspecific background due to auto-fluorescence, scattering, and non-ideal labeling efficiency often adversely affect imaging. Surface plasmon-coupled emission (SPCE) is known to selectively mediate fluorescence that spatially originates from regions close to the metal interface. However, SPCE combined with fluorescence imaging has not been widely successful so far, most likely due to its limited photon yield, which makes it tedious to identify the exact window of the application. As the strength of SPCE based imaging is its unique sectioning capabilities. We decided to identify its clear beneficial operational regime for biological settings by interrogating samples in the presence of ascending background levels. For fluorescent beads as well as live-cell imaging as examples, we show how to extend the imaging performance in extremely high photon background environments. In a common setup using plasmonic gold-coated coverslips using an objective-based total internal reflection fluorescence microscope (TIRF-M), we theoretically and experimentally characterize our fluoplasmonics (f-Pics) approach by providing general user guidance in choosing f-Pics over TIRF-M or classical wide-field (WF).

OCIS codes: (250.5403) Plasmonics; (310.4165) Multilayer design; (180.2520) Fluorescence microscopy; (260.6970) Total internal reflection.

1. Introduction

Fluorescence microscopy has become an indispensable tool in biological imaging due to its selectivity and sensitivity. However, even with bright and photostable markers at hand, auto-fluorescent cellular structures as well as non-ideal labeling efficiency make suppressing out-of-focus fluorescence challenging. This results in a serious bottleneck for crisp biological imaging [152]. A common concept for spatial selectivity and optical sectioning in fluorescence is based on total internal reflection fluorescence microscopy (TIRF-M) [36, 64, 125]. Another concept utilizing evanescent fields is based on Surface plasmon coupled emission (SPCE) [37, 66, 153]. Here, evanescent modes at the metal SPCE supporting nanocoated surface are manipulated. As a result, fluorescence can only be emitted through the coating within the narrow supercritical angle. The efficiency of SPCE depends on the fluorophore–nanocoating distance as well as its relative orientation [80, 81]. SPCE is well known to be able to discriminate close-to-surface signals from signals originating from higher distances [52, 68, 154], and surface plasmon resonant (SPR) illumination of plasmonic nanocoating has been shown to enhance the evanescent TIRF field excitation [155-157]. As demonstrated by several research groups [51, 158], SPCE reduces the observation volume in fluorescence correlation spectroscopy to several attoliters, suppresses fluorescence background and favors a certain dipole emission direction [51, 158]. Nevertheless, applications of SPR and SPCE for surface sensitive fluorescence spectroscopy and imaging are still rare. One reason may be due to the metal-induced energy transfer, which reduces the quantum yield of standard bright molecules [159]. Another reason may be due to the setup geometry, which requires very high numerical aperture (NA ≥ 1.65) objectives [51, 93, 160] or prisms [92, 161] for to collect SPCE.

Here, we theoretically and experimentally dissect the optimal operational regimes and conditions for a successful application of SPCE. First, we compare different plasmonic gold film thicknesses to find the best compromise between coating transparency, SPR excitation and SPCE efficiency. Second, we show how fluoplasmonics (f-Pics) microscopy on gold-dielectric coated coverslips can outperform common imaging techniques by extreme background suppression. We introduce suitable instrumentation and useful operative regime for efficient SPR excitation and SPCE detection that particularly supports live-cell experiments when extremely high photon background is the dominant hurdle.

2. Materials and methods

2.1 Mathematical modeling and simulations

Analytical expression of surface plasmon resonances and plasmonic excitation enhancements on thin noble metal films have been found previously by various analytical approaches (e.g. [73, 74]). The interaction of a point emitter in the vicinity of the metallic surface is given by the Chance, Prock, and Silbey (CPS) theory [83, 84] with its radiation directivity [80]. Here, we use finite element method (FEM) calculations to have access to all parameters describing our experimental situation. With FEM, we simulate an emitter on our metal-dielectric multilayer system. From this, derive excitation field enhancement and radiation rates, fluorescence quenching, transmission through the multilayer system and the detection efficiency.

We performed FEM calculations (Comsol Multiphysics 4.4) for the radiative and non-radiative dipole emission rates and far-field radiation distribution, considering different dipole to surface heights and orientations (parallel and perpendicular). We simulated a dipole emitter in water (RI = 1.33, QY_0 = 0.35, emission peak: 665 nm) that mimics the situation for Alexa 647 that we use later in the experiment. We placed the dipole at different distances above an uncoated (RI = 1.78, NLAFN-21) and coated glass substrate. The coating design includes a 2 nm chromium layer followed by a gold layer (different thicknesses selected between 10 to 50 nm) and a capping layer of 6 nm silicon-nitride. The wavelength dependent complex refractive indices are extracted from literature [71, 162], also accessible by (https://refractiveindex.info/). The radiation rates k_{rad} in close vicinity to the surface are directly connected with the line integral of the power outflow $\mathrm{P}(\varphi)$ [163]. To determine the amount of light collected by the objective lens (NA = 1.7), we calculate the detection ratio of radiation reaching the objective to total radiation:

$$\frac{\mathrm{k_{rad,obj}(z)}}{\mathrm{k_{rad}(z)}} = \frac{\int_{-\mathrm{NA}}^{\mathrm{NA}} \mathrm{P(\varphi,z)d\varphi}}{\int_{0}^{360^\circ} \mathrm{P(\varphi,z)d\varphi}} \qquad \text{(Eq. 4-1)}$$

Since excitation of evanescent waves and absorption effects of the gold coating are connected with reduced radiation strength, we can express the non-radiative rates by the difference between total and radiative dipole emission rate $(\mathrm{k_{tot}} - \mathrm{k_{rad}})$, where the total dipole emission rate $\mathrm{k_{tot}}$ given by the 360° line integral of the power outflow at the dipole position. The resulting height dependent quantum yield QY(z) [68, 164] can be expressed as follows:

$$\mathrm{QY(z)} = \frac{\mathrm{k_{rad}(z)/k_{rad,0}(z)}}{\mathrm{k_{rad}(z)/k_{rad,0}(z)+(k_{tot}(z)-k_{rad}(z))/k_{rad,0}(z)+(1-QY_0)/QY_0}} \qquad \text{(Eq. 4-2)}$$

Here $\mathrm{k_{rad,0}}$ represents the radiation rates of the dipole not affected by an interface. Note that emission rate values are averaged over the dipole orientations. The excitation is considered as an evanescent field [36]:

$$I_{exc.}(z,\theta) \propto \left|\frac{E}{E_0}\right|^2 e^{-z/\delta(\theta)} \quad \text{(Eq. 4-3)}$$

Here the excitation enhancement factor is $|E/E_0|^2$. The field enhancement of our multilayer system is simulated by oblique angle illumination of a glass/gold/coating/medium interface originating from the glass side. We used periodic ports parallel to the multilayers and periodic boundary conditions to complete the model in the perpendicular direction. The penetration depth of the evanescent field is [37]:

$$\delta(\theta) = \frac{\lambda_o}{4\pi\, RI_{cover}} \frac{1}{\sqrt{(\sin^2\theta - \sin^2\theta_c)}} \quad \text{(Eq.4-4)}$$

Here RI_{cover} is the refractive index of the coverslip and $\sin\theta_c = RI_{medium}/RI_{cover}$ the sine of the critical angle. By multiplication of excitation field $I_{exc.}$, quantum yield $QY(z)$ and detection ratio of the radiative rates $k_{rad,obj}(z)/k_{rad}(z)$ we derive the fluorescence at a certain distance z to the coverslip. Finally, we can calculate the theoretical intensities for fluorescent spheres and homogenous fluorescent background:

$$Signal_{Bead} \propto \int_0^{max} \left|\frac{E}{E_0}\right|^2 e^{-\frac{z}{\delta(\theta)}} \rho_{Bead}(z) QY(z) \frac{k_{rad,obj}}{k_{rad}}\, dz \quad \text{(Eq. 4-5)}$$

$$BGR \propto \int_0^{max} \left|\frac{E}{E_0}\right|^2 e^{-\frac{z}{\delta(\theta)}} \rho_{BGR}\, QY(z) \frac{k_{rad,obj}}{k_{rad}}\, dz \quad \text{(Eq. 4-6)}$$

Here $\rho_{Bead}(z) = \pi\,(Dz - z^2)$ describes a spherical dye distribution with diameter D, ρ_{BGR} represents fluorescent background induced by a homogenous dye distribution. We performed those calculations for different gold thicknesses and normalized the results to the uncoated case (standard TIRF) to pinpoint the best compromise between most efficient SPR illumination, SPCE collection, and lowest signal losses. As a measure for the image contrast, we calculate Signal/(Signal + BGR) which provides a value for contrast that is independent of the illumination strength.

2.2 Metal coating and coverslip preparation

Fabrication of the metal-dielectric coating is performed in a HEX deposition system (Korvus Technology Ltd.) equipped with a radio frequency magnetron sputtering (for dielectrics deposition) and an e-Beam evaporation system (for metals). Coverslips with high refractive index RI were used (NLAFN-21, 150 µm thick, UQG Optics Ltd.). The metal coating consists of a 2 nm adhesion promoter (chromium, 99,99%, Goodfellow), followed by a gold layer (99,99%, EVOCHEM) and a 6 nm Si_3N_4 layer (hot-pressed Si_3N_4 sputtering target, Goodfellow).

2.3 Experimental setup

We used a home-built total internal reflection fluorescence microscope (TIRF-M) setup in combination with a commercial base (IX71, Olympus). A digital illumination angle control was used to perform wide-field, TIRF and f-Pics imaging with red laser illumination of 640 nm (OBIS 640nm LX 40 mW). The beam was expanded to 4 mm beam diameter and deflected by a digital scan mirror (62xxH series galvanometer XY, Cambridge Technologies). The laser is focused (f = 200 mm, AC254-200-A-ML Thorlabs) onto the back focal plane (BFP) of the TIRF objective (APON 100XHOTIRF, Olympus, NA = 1.7). A linear polarizer ensured efficient excitation of surface plasmons by p-polarized light (half-wave plate AHWP05M-600, Thorlabs). Note that an objective lens with NA ≥1.65 is strictly required to be able to induce SPR excitation and/or SPCE collection of fluorescence in aqueous or cellular samples [93]: For gold coatings on standard glass coverslips, the SPR/SPCE angle is between 80° and 90° (for

RI= 1.33 to 1.4 in visible spectral regime, calculations see [74]). This angle is higher than the maximum possible excitation/collection angle limited by numerical aperture ($NA \leq 1.49$, $\vartheta_{max} = 78°$) of the objective lens. For NA = 1.7 ($\vartheta_{max} = 72°$) the use of coverslips with a high refractive index (RI = 1.78) reduces the plasmon resonance angles below 70°, which makes SPR/SPCE possible in our TIRF setup.

The fluorescence signal is split and filtered by a dichroic mirror and a band pass filter (F73-421PH and F73-697 (697/58), AHF Analysentechnik). The fluorescence signal is projected onto a camera (Neo 5.5 sCMOS, Andor). Camera detection and laser illumination are synchronized to minimize light exposure of the sample. Scan mirror, laser power, and camera acquisition are controlled by analog signals (PCI-6733, National Instruments) and the python script "Shadowless TIRF" from Ellefsen, Dynes, and Parker [126]. Minor modifications in this python script allow synchronized mirror deflection, laser excitation, and camera detection. Images and image stacks are acquired with the software of the camera manufacturer (Solis, Andor). Calibration curves of the illumination angle θ show a linear behavior over the mirror deflection voltage (slope = 78.9°/V). The penetration depth was determined on uncoated substrates with 6 µm fluorescently stained microspheres (FI4806, Invitrogen) on poly-D-lysine coated coverslips in an aqueous environment (for method see [131]). We determined penetration depths of (179 ± 18) nm at illumination angle (ϑ = 54° ± 1°) and (89 ± 11) nm at SPR angle (60° ± 1°).

2.4 Imaging of fluorescent beads and background characterization

For characterization of the illumination angle dependent fluorescence signal and background suppression, we used 100 nm multi-color fluorescent beads (T7279, TetraSpeck Microspheres 0.1 µm, Invitrogen) on coated and uncoated coverslips excited at 640 nm. We experimentally confirmed the random distribution of fluorescent molecules of the fluorescent bead by polarization and implemented a polarizer in the emission path. To avoid photobleaching by the strong SPR excitation enhancement during the acquisition series, we used a relatively low laser power of 20 µW, camera binning 2 and exposure time of (0.5 – 1.0) seconds. For easy comparison, signals are normalized to counts/s. Analysis of signal and background was supported by the python module "Trackpy" [165]. "Trackpy" localizes and analyzes fluorescence signals originated from the beads on uncoated and coated coverslips. For each event, "Trackpy" calculates the amount of total and signal fluorescence in an area connected to the event so that the background can be calculated by the difference of total "Raw" and signal "Signal" intensity.

$$\mathrm{BGR} = \mathrm{Raw} - \mathrm{Signal} \qquad \text{(Eq. 4-7)}$$

We performed a fluorescent background series by adding different concentrations of Alexa Fluor 647 (A647) labeled oligonucleotides (IBA, for sequence [166]) in ultrapure water (mili-Q, Millipore Corporation). In contrast to pure dye solution, the oligonucleotides coupled to the dye prevented unspecific binding to the surface in our experiments.

2.5 Cell Culture, immunostaining, image acquisition and analysis

We cultured wild-type Chinese Hamster Ovary (CHO) cells on un-/ coated coverslips at 37°C and 5% CO_2 in Dulbecco`s Modified Eagle Medium (DMEM/F12, Thermofischer), and performed experiments on uncoated and coated coverslips in the same manner for comparison. The plasma membrane was fluorescently stained (Cellmask Deep Red, Invitrogen, 1x = 1 µl/ml). After 10 minutes of incubation with cell mask, the cells were washed 3 times with DMEM (Gibco, Lifetechnology). For image acquisition, we transferred the cell dish to a home-built imaging chamber that allowed measurements under physiological conditions. On the microscope, we kept the cells in phenol-red free DMEM buffered by 15 mM HEPES for pH-stability. Cell mask in excess (0 - 6 µl/ml) induced a significant fluorescence background. Image acquisition was at 100 µW laser power (before the objective) and 200ms camera exposure time without binning, For wide-field microscopy the illumination angle was

set to 0°, for TIRF and SPR to ≅ 60° reflecting the surface plasmon resonance angle to induce maximum fluorescence on coated coverslips.

For characterization of cell membrane signal and step sharpness, we use Gwyddion [124] to extract profiles from the cell membrane to coverslip transition and fit the line scan with a smooth step function $f_{step}(x)$.

$$f_{Step}(x) = BGR + \frac{Signal}{2}\,erf\left(\frac{x-x_0}{w}\right) \qquad \text{(Eq.4-8)}$$

Here, $Signal$ from the cell membrane is given by the step height of an error function $erf\left(\frac{x-x_0}{w}\right)$ at the position x_0 with w as step width. We started the experiment without induced background and then subsequently increased the fluorescence background.

3. Results

First, we simulated SPR field enhancement (excitation pathway), and SPCE fluorescence (emission pathway) independently, to determine the optimal thickness of the metal coating. We simulated the situation of a fluorescent emitter on a gold coated versus an uncoated glass surface. Figure 4-5(a) shows the logarithmic electric field intensity distribution of both scenarios (uncoated and coated) for different emitter distances and orientations to the surface. Figure 4-5(b) shows the emission directivity of our emitter oriented parallel or perpendicular to the interface and for the dipole close to (30 nm) or far from (400 nm) the interface. The gray area illustrates the collection angle of the objective lens. For an uncoated interface, fluorescence emission follows the classical dumbbell radiation pattern with small modification by the refractive index difference at the interfaces. The “butterfly” shaped radiation of an emitter perpendicular (p-pol) to the surface is known as supercritical angled fluorescence (see e.g. [153]) and disappears for increased z. On the uncoated interfaces and for a parallelly oriented emitter the fluorescence pattern (s-pol) is less affected by refractive index mismatch. In the case of our gold coatings, the situation is different: The higher reflectivity and lower transparency of our coatings restrict transmittance of fluorescence, and thus light collection by the objective lens. Fluorescence coupled to the gold surface plasmons (SPCE) is able to pass the gold layer and is most efficient for p-pol fluorescence from emitters few tens of nanometers above the interface [80]. Thus, fluorescence originating from such fluorophores is most pronounced. Since a randomly dipole orientation is the most meaningful scenario in our (biological) experiments, we assumed an averaged dipole orientation.

Second, to determine the ideal gold layer thickness for our scenario we simulated the emission of a 100 nm fluorescent sphere a homogenous distributed background separately. Intensities were normalized to the uncoated case. As shown in Fig. 4-5(c), best imaging performance is expected around 30 nm gold thickness where the plot of fluorescence on different gold layers as well as the expected background peak. A gold thickness of 30 nm leads to the highest intensity and a clear signal contrast even if the strongest SPR is observable for ~48 nm thick gold layers. Note that without excitation enhancement; detected fluorescence is strongly reduced compared to the case without coating.

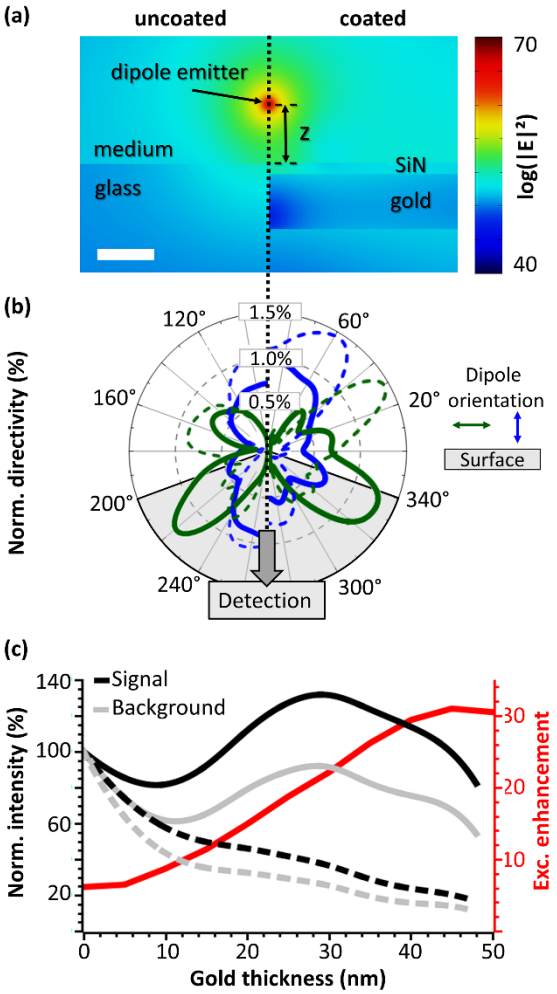

Fig. 4-5. Finite element method calculations for surface plasmon coupled emission. (a) Electric field distribution log(|E|²) of an electric dipole emitter next to an uncoated and coated (gold 30 nm) medium/glass interface (scale bar 30 nm). (b) The corresponding far-field radiation patterns for a dipole with parallel (dark green) and perpendicular (blue) orientation are depicted for dipole-to-surface distances of 30 nm (solid) and 400 nm (dashed). (c) Calculated intensities for a fluorescent sphere (black, sphere diameter: 100 nm), and a homogenously distributed background (gray) for different gold thicknesses. Intensities were calculated w/ (solid) and w/o (dashed) plasmonic excitation enhancement (red).

Next, we simulated the fluorophore behavior at a distance z above the interface. In Fig. 4-6(a) we plotted the effective distance depending quantum yield QY for a near-infrared dye emitter (emission: 665 nm) with intrinsic quantum yield QY_0: For the chosen metal-dielectric nanolayers, fluorophores with $QY_0 > 0.4$ are strongly quenched in the first nanometers than those with lower QY_0 [68]. In other words, the effective QY of fluorophores with low QY_0 increases in the plasmonic environment while QY (and brightness) decreases in the case of high QY_0. For the following experiments, we will use the commonly used fluorescent dye A647 (emission: 665 nm, $QY_0 = 0.35$) that benefits from such quantum yield modification in the SPCE efficient region. Next, we simulated the fluorophore signal intensity in dependence of distance z above the interface; see Fig. 4-6(b). Here the signal is the product of the excitation field, quantum yield and the detection efficiency (for details see Methods section). Wide-field (WF) and TIRF illuminations (for penetration depths of 169 nm ($\vartheta_{crit} \leq \vartheta = 50°$) and 72 nm ($\vartheta_{SPR} = 58°$) are modeled for an uncoated interface. The SPCE is calculated on the coated interfaces at SPR excitation. The TIRF and WF signal distribution follow their well-known decay behaviors. The signal in the case of SPCE starts lower due to fluorescence quenching, followed by a steep rise when

efficiently coupling to surface waves, and peaks at ≈ 50 nm distance before dropping rapidly at higher interface distances. The simulations shown in Fig. 4-6 are in good agreement with the experimental results reported in the literature [167]. Note that the silicon nitride spacer layer prevented stronger fluorescence quenching at z ≈ 0 nm. To pinpoint the benefit of SPCE compared to WF and TIRF, we calculated Signal/(Signal + BGR) as a measure of contrast for 100 nm fluorescent beads (Signal) attached to the nanolayered interface and a homogenous background (BGR). The concentration ratio of BGR and Signal is given by the factor c, while here BGR = c·$BGR_{c=1}$. In Fig. 4-6(c) we plot the Signal/(Signal + BGR). For all illumination methods reasonable contrast is given until a BGR exceeds the signal by a factor of 100 and drops later to zero depending on the illumination method. We confirmed that changes of the signal contrast are negligible for small quantum yield variations, which may occur in heterogeneous chemical environments or different buffer solutions.

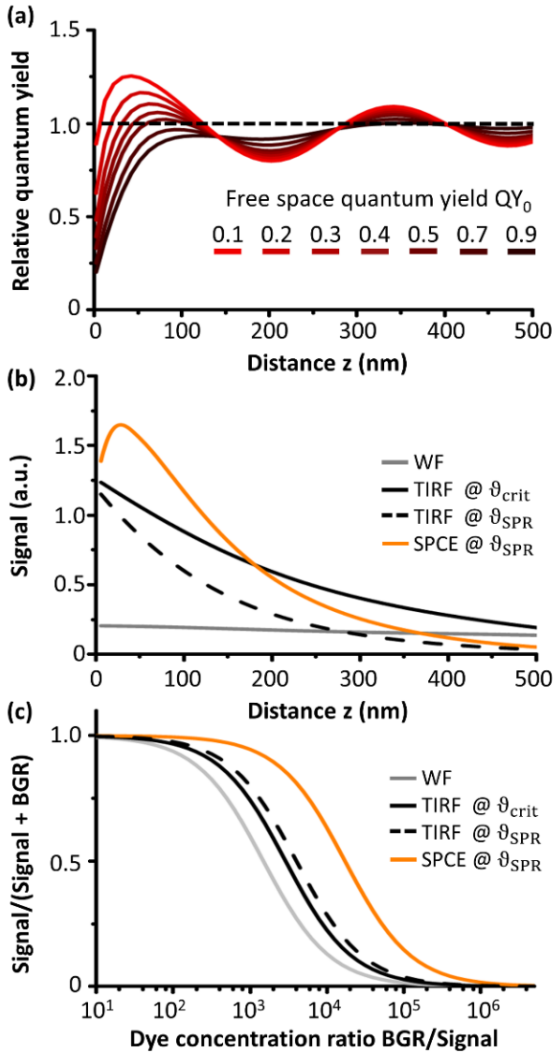

Fig. 4-6. FEM calculations of fluorophore behavior. (a) Distance z depending relative fluorescence quantum yield QY/QY_0 for different free space quantum yield QY_0. (b) Calculated signal collected by an objective lens (NA = 1.7) for different fluorophore distances z to the uncoated (WF and TIRF) and coated (SPCE, 30nm gold coating) coverslip surface. (c) Contrast of fluorescence signal (Signal) and homogenous background (BGR) depending on dye concentration ratios for different illumination scenarios. A step like Signal/(Signal + BGR) distribution illustrates the signal-contrast in high-background environments. The signal-contrast is independent from the excitation amplitudes. For TIRF two different penetration depths (solid: 169 nm; dashed: 72 nm) were considered. The penetration depths for SPCE under SPR illumination is 64.4 ± 0.3 nm (extracted by a mono exponential decay fit, z > 20nm).

For experimental validation of our theoretical simulations, we used a home-built TIRF-M. For intensity characterization of the fluorescent beads on coated and uncoated coverslips, a high NA objective (NA = 1.7) provided efficient excitation of SPR and collection of SPCE. Our TIRF setup allows computer assisted fine 0.5°deg changes of the excitation angle ϑ to precisely hit the critical ($\vartheta_{\mathrm{crit}}$) and SPR ($\vartheta_{\mathrm{SPR}}$) excitation angles. Figure 4-7(a) shows an illustration of the TIRF-M setup. By sweeping the excitation angle, different modes of fluorescent excitation can be induced. For uncoated interfaces, the fluorescent beads are visible for all illumination angles. The fluorescence signals for undercritical WF illumination and critical to overcritical TIRF illumination is shown in Fig. 4-7 (b). When approaching the critical angle, the fluorescence is increased due to resonance excitation of the surface modes and then drops rapidly when further increasing the angle. In contrast, for coated coverslips (gold layer thickness > 25 nm) the beads are only visible at SPR illumination. A doughnut-shaped point-spread function (PSF), a well-known characteristic of the SPCE [168-170], is clearly observable. Analysis of signal and background was supported by the python module "Trackpy" [165]. Figure 4-7 (c) shows the resulting average signal of beads for different gold thicknesses with highest values for uncoated and 30 nm gold-coated coverslips. Thus, the latter was picked as the best compromise to efficiently analyze samples in high background environments.

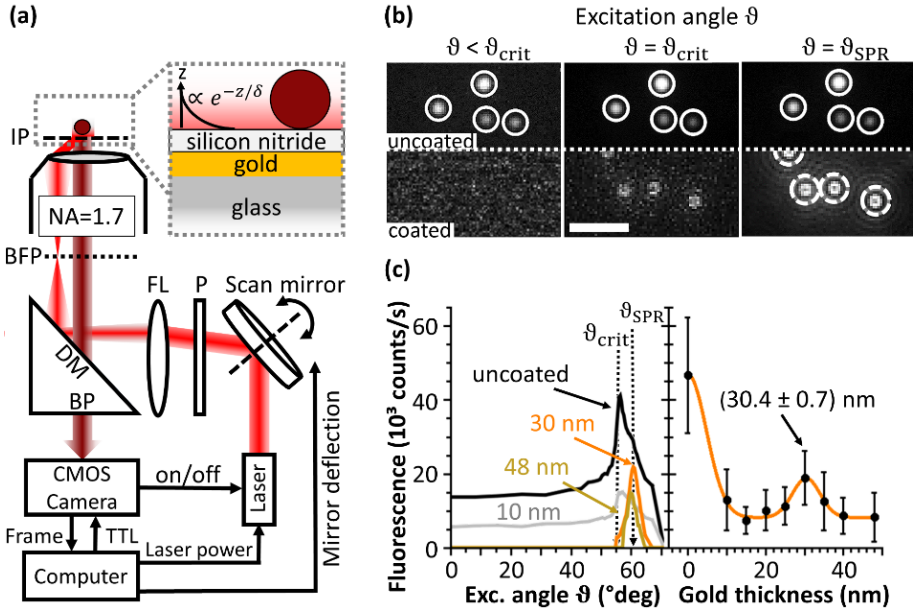

Fig. 4-7. Experimental f-Pics setup and performance scheme of the setup and sample configuration. (a) Main optical components include scan mirror, laser (640 nm), linear polarizer (P), focus lens (FL), dichroic mirror (DM) and bandpass filter (BP). The TIRF objective back focal plane (BFP) and the image plane (IP) are indicated. (b) Measurements of fluorescent spheres on uncoated and coated coverslips for different excitation angle ϑ: undercritical $\vartheta < \vartheta_{crit}$, critical $\vartheta = \vartheta_{crit}$ and surface plasmon resonant (SPR) $\vartheta = \vartheta_{SPR}$ excitation. The circles indicate analyzed objects. Scale bar: 2 µm. (c) Excitation angle ϑ dependent fluorescence of spheres on gold coatings (left), and the maximal fluorescence for different gold thickness (right) with best performance for 30 nm gold layers.

Figure 4-8 shows fluorescence images of beads on uncoated and gold coated glass coverslips in the presence of different background levels induced by respective cell mask concentrations. In Fig. 4-8 (b) the results for the signal to background contrast are summarized. The step-like function observed in Fig. 4-8 (b) is in compliance with the theoretical calculations shown in Fig. 4-6 (c). For low BGR, the fluorescent beads are clearly observable on uncoated (WF and TIRF) and coated glass (SPR excitation). For such low BGR conditions, classic TIRF-M is clearly preferable as it provides higher photon yield and thus outperforms f-Pics as expected. The situation is different for high (100 nM) BGR: Even if exhibiting sufficient contrast in TIRF mode, beads show the best contrast in f-Pics where SPR excitation and SPCE provides background-suppression far beyond TIRF-M. Finally, at extreme BGR of 500 nM, beads only remain detectable for f-Pics.

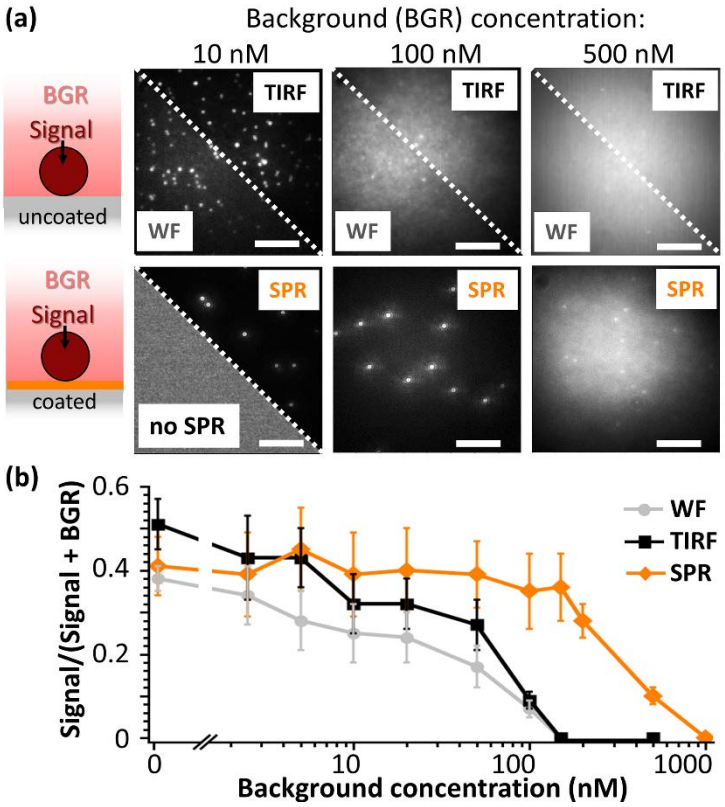

Fig. 4-8. (a) Images of fluorescent beads (emission bandpass 697-58) *in high background A647-oligonucleotides environment on uncoated (WF and TIRF) and coated (SPR, 30 nm gold) coverslips. (b) Results of the signal-to-BGR analysis for different BGR concentrations. Scale bars: 10 µm.*

Next, live-cell imaging is performed to test the versatility of our operational regime. Figure 4-9(a) shows respective cell images (with additional background 0, 2 and 4 µl/ml) detected in the presence of a high fluorescent background. For TIRF and SPR illumination (both by $\vartheta \cong 60°$) the intensity profiles in Fig. 4-9 (b) derived from panel (a) exhibit a step profile at the cell membrane. For WF illumination, the intensity rises further towards the image center because of the unselective axial illumination. We analyzed intensity profiles to identify cell signal and background, respectively. For all illumination modes, the step height and base values are determined; in addition, for TIRF and SPR the step width was described by a slanted step model, so that step base and height determine the signal-to-background contrast see Fig. 4-9 (b). The step widths are 0.65 ± 0.21 µm and 1.27 ± 0.27 µm for TIRF and SPR illumination (cell numbers N > 10). The reason for the increased step size is the doughnut-like PSF on the metallic films resulting in blurrier images. For comparison, we measured a full width half maximum (FWHM) of 100 nm beads of ~330 nm on uncoated and ~435 nm on coated coverslips.

The results of background suppression are comparable to the previously shown experiments in Fig. 4-8 and the theoretical results in Fig. 4-6(c). For WF and TIRF, the contrast drops immediately when the staining concentration is increased. For the SPR illumination on coated coverslips, the contrast remains high, and only decreases if background concentration is increased to 6 µl/ml. Taken together, the background suppressed operative regime for this live-cell experiments on coated coverslip ranges from ~2 to 4 µl/ml staining concentrations.

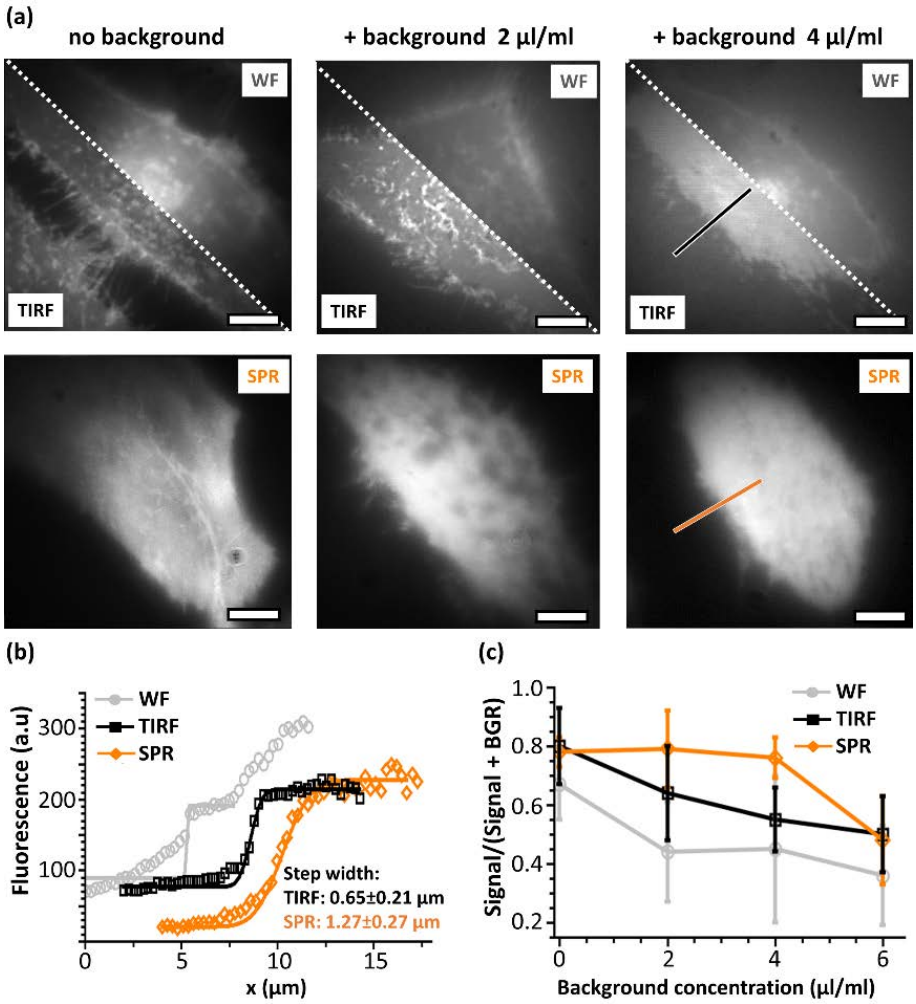

Fig. 4-9. (a) Fluorescence images of living membrane stained CHO cells on uncoated (WF, TIRF) and gold coated (30 nm, SPR) coverslips. (b) Example of lateral intensity profiles (open symbols) with data fits (solid lines) representing step models to dissect image contrast. (c) Comparison of image contrast for depicted imaging modalities. Scale bars: 5 µm

4. Discussion

SPCE for fluorescence imaging has not been widely successful far; most likely due to its limited photon yield compared to other techniques. Here, we showed that there is an attractive SPCE operational regime for extremely high background applications including live-cell experiments in a noisy environment. In our experiments, the determined image contrast was decoupled from the excitation enhancement so that dissection of the interesting operational regime for f-Pics became evident. Thus, we systematically explored an experimental regime where surface plasmon assisted microscopy in our f-Pics approach provides higher image contrast compared to TIRF-M. As our data shows, f-Pics allows for imaging under high-background conditions. While 20 nM to 500 nM background fluorophore concentration would prevent imaging by WF and TIRF-M, SPCE is more selective and enables fluorescence imaging under this extreme background conditions.

For the respective coating design, we identified 30 nm gold as optimal layer thickness and confirmed this by computational modeling and imaging experiments. Unfortunately, the optimal gold layer thickness always represents a compromise when an epi-fluorescence, objective-based illumination mode is used. Therefore, this approach is not ideal for very low-light or single molecule applications where a prism-based setup [155, 156, 171] with decoupled excitation and detection pathways would provide more detection efficiency but no SPCE fluorescence selectivity.

To make the method more versatile for future applications, f-Pics need to address the reduction of ohmic losses inside the metal layer. The reduced quantum yield and the doughnut-shaped PSF of the SPCE are equally unfavorable for fluorescence-based applications. Approaches to overcome these issues are under current development. It has been already demonstrated that the doughnut-shaped PSF can be transferred with polarizers into an Airy-shaped PSF to increase the resolution preferable with deconvolution later [169, 170]. As alternative methods, supercritical angle fluorescence (SAF) approaches blocking fluorescence signals in the Fourier plane [172] are useful to distinguish between surface-near and surface-far fluorescence. In SAF approaches, the PSF stays Gaussian-shaped and the signal losses are lower than for SPCE; however, modifications in the instrumentation are required to separate undercritical and supercritical fluorescence in the detection, followed by computational recombination. This additional effort allows for excellent 3D super-resolution [89, 94]. In comparison, the main advantage of nanocoatings such as used in f-Pics is their straight-forward experimental implementation. This, taken together with their capability of extreme background suppression under biologically relevant conditions, makes them unique and highly valuable for applications that otherwise suffer from high background levels.

Another innovative approach for nanocoatings are all-dielectric multilayer coatings, which support evanescent modes by Bloch surface waves without ohmic and diffraction losses [173]. If this issue is solved, we believe that such evanescent interface mode-supported fluorescence may have exciting prospective for surface sensitive fluorescence-based imaging and spectroscopy. It could be beneficial for high-throughput screening (on non-purified substances), cell growth studies and near-surface binding studies where a reservoir of fluorescent dye is present or added for long-time studies. Imaging cell membrane receptors of adherent cells to study receptor interactions or internalization would be straightforward even if a high concentration of markers inside the cell would outshine the specific membrane signal.

4.3 Enhanced fluorescence resonance energy transfer in G-protein-coupled receptor probes on nanocoated microscopy coverslips

The content of this chapter has been published [133]:

Schreiber et al. Enhanced Fluorescence Resonance Energy Transfer in G-Protein-Coupled Receptor Probes on Nanocoated Microscopy Coverslips *ACS Photonics*, 2018, 5 (6), pp 2225–2233

https://pubs.acs.org/doi/10.1021/acsphotonics.8b00072

Summary and contribution:

In this article the FRET enhancement capacities of gold nanocoatings are presented. This is demonstrated for G-protein coupled receptors, where CFP-FlAsH construct is used as a sensor. The FRET sensors are expressed in M1 muscarinic membrane receptor in intact living cells. For this sensor, the coatings reinforce “forbidden FRET” between not optimal orientated donor-acceptor molecules. A FRET enhancement of ~ 60% compared to uncoated glass coverslips on the used FRET sensor is observable. The results are supported by simulation of the fluorescence emission in vicinity of the coatings.

I worked out the theoretical framework and performed one part of the data analysis, together with Michael Kauk who performed the FRET experiments and the other part of the data analysis. Both authors contributed equally to this work. I performed the simulations together with Hannah S. Heil and I designed and fabricated the gold substrates together with Monika Emmerling; Dr. Martin Kamp and Prof. Dr. Sven Höfling supervised the fabrication process. Dr. Ingrid Tessmer characterized the roughness of gold surfaces by AFM. Iperoxo was synthesized in the lab of Ulrike Holzgrabe. Prof. Dr. Katrin G. Heinze and I wrote the paper. Prof. Dr. Katrin G. Heinze and Prof. Dr. Carsten Hoffmann conceived and designed the experiments.

Enhanced fluorescence resonance energy transfer in G protein-coupled receptor probes by nano-coated microscopy coverslips

Benjamin Schreiber[#, ‡], Michael Kauk[#, ⊥, ||, ‡], Hannah S. Heil[#], Monika Emmerling[†], Ingrid Tessmer[#], Martin Kamp[†], Sven Höfling[†, §], Ulrike Holzgrabe[//], Carsten Hoffmann[#, ⊥, ||, *], Katrin G. Heinze[#, *]

[#] *Rudolf Virchow Center, Research Center for Experimental Biomedicine, University of Würzburg, Josef-Schneider-Str.2, 97080 Würzburg, Germany*
[||] *Department of Pharmacology and Toxicology, University of Würzburg, Versbacher Strasse 9, 97078, Würzburg, Germany*
[⊥] *Institute for Molecular Cell Biology, CMB-Center for Molecular Biomedicine, University Hospital Jena, Friedrich Schiller University Jena, Hans-Knöll-Strasse 2, 07745, Jena, Germany*
[†] *Technische Physik, Physikalisches Institut and Wilhelm Conrad Röntgen-Center for Complex Material Systems, University of Würzburg, Am Hubland, 97074 Würzburg, Germany*
[§] *SUPA, School of Physics and Astronomy, University of St Andrews, St Andrews, KY16 9SS, United Kingdom*
[//] *Institute of Pharmacy, Pharmaceutical and Medicinal Chemistry, University of Würzburg, Am Hubland, 97074 Würzburg, Germany*
[‡] *B.S and M.Kauk contributed equally to this work.*

[*] *Correspondence to katrin.heinze@virchow.uni-wuerzburg.de or carsten.hoffmann@uni-jena.de*

ABSTRACT: The G-protein-coupled receptor (GPCR) superfamily mediates cellular responses and communication across cellular membranes, and is the largest known class of molecular targets with proven therapeutic value. For probing conformational changes of GPCRs and others in a live-cell setting Fluorescence Resonance Energy Transfer (FRET) is usually the method of choice. FRET probes often require careful labeling procedures, elaborate characterization and assay optimization to provide both physiologically relevant probes with unaltered pharmacology and a sufficient dynamic range of the FRET changes. Here, we present an approach to optimize the energy transfer without changing the design of the FRET probe. We show that gold coated glass cover slips allow reinforcing the otherwise forbidden donor-acceptor energy transfer by virtual optimization of the dipole orientation. First, we confirm the resulting enhanced FRET on our nano-coatings for the inactive M1 muscarinic acetylcholine receptor (mAChR) labeled with a CFP-FlAsH pair in classical bleaching experiments. Second, we demonstrate the advantage of this enhanced FRET technique for ligand binding studies in live cells by the increased dynamic FRET response between the inactive and active state of the M1 mAChR receptor. Our method is not limited to GPCRs, and thus has general potential for surface-bound FRET approaches. We believe our technique is particularly suited for pharmaceutical drug screening to boost FRET probes, where amplifying signal responses without interfering with the well-characterized assay is highly desired.

KEYWORDS: fluorescence spectroscopy, FRET, receptor dynamics, membrane biophysics, fluorescence enhancement

Introduction

G-protein-coupled receptors (GPCRs) represent the most versatile and pharmacologically most important class of membrane receptors that regulate cellular functions and constitute prominent targets for drug therapy [174]. Over the last decades tremendous efforts were made to gain structural knowledge about GPCRs, mostly by investigating X-ray crystal structures.[175] Hence, inactive as well

as active X-ray structures have been solved for different class A GPCRs. In combination with molecular modeling analysis and numerous mutational studies detailed models were developed concerning the activation processes [176, 177]. But still, we know very little about structural dynamics because X-ray structures mostly provide averaged snapshots of different receptor states. Thus, we and others have developed fluorescence resonance energy transfer (FRET) techniques for GPCRs that allow us to monitor particularly conformational changes of GPCRs, which corresponds to agonist-induced activation [15, 16, 21, 178]. The chance to study GPCRs in their native environment on a millisecond timescale made and still makes a valuable contribution to biomedical research [23, 179]. FRET is one of the most general and adaptable live cell techniques. Despite the explosive growth in the biological application of FRET in the last decade, the method still has its weak points; one is the probe design, and its consequences on the final FRET data quality.The design of GPCR FRET probes is elaborate and crucial to ensure unaltered functionality and binding kinetics of the molecular complex.[16, 21, 180-183] For the assay design, this means limited options for donor-acceptor positions, distances and orientations, and often a compromise to the detriment of detectability of emitter signals in general, and the dynamic range of the FRET changes in particular.

An improved donor-acceptor energy transfer can be obtained by specific labeling strategies such as multiple acceptor molecules [184-186] and plasmonic nanoparticles [187-189]. However, additional linkers and particles on the receptor may interfere with ligand binding, diffusion, and other crucial GPCR dynamics. One promising approach to manipulate the direct donor-acceptor FRET without manipulating the probes are optically active nanostructures such as microresonators [190, 191], nanoapertures [166, 192] or nanoantennas [193]. Unfortunately, these methods may not be able to address a wide range of applications. Particularly for live cell studies it can be difficult or even impossible to bring the fluorophore of interest within or inside such photonic environment. A well-known approach is the control of fluorescence emitters on or above mirror surfaces, which allow manipulating the emission [82, 83]. Such approaches, highly compatible with fluorescence microscopy, cannot only enhance fluorescence, but also support axial super-resolution in (live) cell imaging [85, 87, 88]. Even if classically a positive effect on FRET efficiency above such reflective surfaces is almost unnoticeable [194-197] the recent work of de Torres [198] and co-workers elegantly derive a new photonic model including the dipole-dipole orientation factor κ^2 of the fluorophore, and have brought to proof that improved FRET is possible on specific photonic environments. They show that photonic environments have an effect on FRET by virtually depolarizing the electric nearfield of donor and acceptor. Those 'forbidden states' eventually have a significant influence on the average dipole orientation $\langle\kappa^2\rangle$. Until then, it was generally assumed that $\langle\kappa^2\rangle = 2/3$, which is true for homogenous angular distribution of donor and acceptor molecules, but not necessarily for systems with limited degrees of freedom, such in the case of labeled GPCRs where other $\langle\kappa^2\rangle$ values are possible [61].

Here we present how to utilize and optimize this effect [198] to increase the FRET efficiency for *in vivo* live cell experiments on gold coated microscopy slides. We performed FRET studies on the M1 muscarinic acetylcholine receptor (mAChR**)** in human embryonic kidney (HEK) cells labeled by cyan fluorescence protein (CFP; C-terminus) and fluorescein arsenical hairpin binder (FlAsH; inter cellular loop 3 (IL3)). This FRET assay has been already well characterized [21, 24] and proven to be advantageous for GPCR studies under physiological conditions. We demonstrate the increased FRET efficiency by typical acceptor bleaching experiments, and further monitor receptor activation of M1 mAChR by ligand application experiments by FlAsH/CFP ratiometric FRET measurements. Our observations are fully supported by simulations and mathematical modeling.

Results and discussion

For a FlAsH-CFP FRET sensor, we first analyze the fluorescence and FRET efficiencies for different sample configurations with and without the gold coating. First, the FRET efficiencies of the inactive M1 mAChR (figure 4-10(a)) were determined by BAL induced chemical acceptor bleaching experiments (figure 4-10b(c)). Bleaching experiments in three configurations are shown: on an uncoated glass surfaces for reference (figure 4-10(a) left), on gold coated coverslips in upright configuration (figure 4-10(a) middle) as well as in a flipped configuration (figure 4-10(a) right). For the latter the sample was covered by an additional coverslip. The ratio of the donor intensity before and after BAL treatment represents the FRET efficiency. Figure 4-10(b) shows typical CFP and FlAsH intensity curves and the respective FRET efficiency over time. As expected the fluorescence in the CFP detection channel rose after addition of BAL while the intensity of the FlAsH signal dropped indicating that the FlAsH label dissociated from the receptor and the system transfers from maximum FRET of the sensor to no-FRET. Note, for reasons of sample geometry this process needs approximately 50 s for the upright configuration and more than 100 s for the flipped configuration due to the restricted diffusion within the limited space between the coverslips.

The average FRET efficiency increased from 16.3 ± 1.1 % on glass to 21.6 ± 1.7 % for the gold coated coverslips in upright and even 26.3 ± 2.8 % in the flipped configuration. Thus, for gold coated coverslips the FRET efficiency of our inactive FRET sensor were significantly improved by up to 61 % and consequently the dynamic range of the experiment. We are convinced that the FRET efficiency on the gold upright configuration is principally comparable to the flipped configuration, however the higher noise by excitation and emission through the gold films slightly reduce the enhancing effect in the upright case. In parallel, we performed respective acceptor photobleaching experiments in flipped configuration to compare the results. We found FRET efficiencies of 15.4 ± 1.1 % for glass and 25.8 ±2.0 % for gold coated coverslips, which are comparable to the experiments based on chemical bleaching. Taken together the chemical and photobleaching experiments in different configurations we can exclude artefacts that may lead to FRET efficiency overestimation. Thus, the first important finding is that gold-coated coverslips can boost the performance of FRET studies.

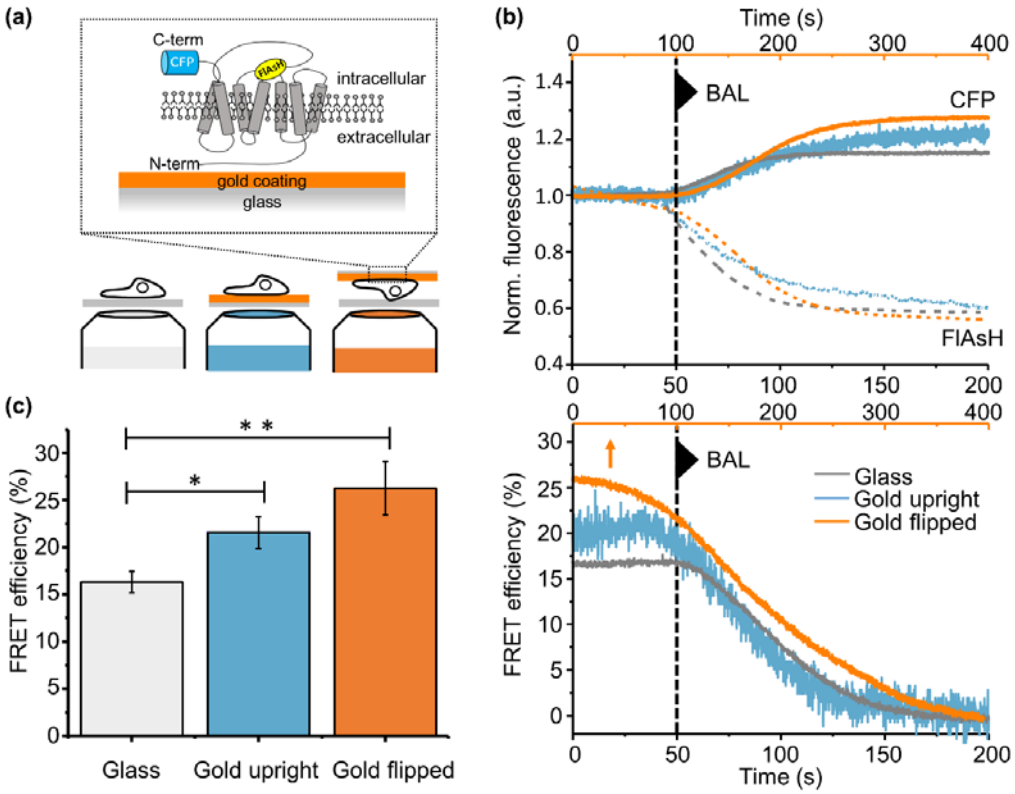

*Figure 4-10. Comparison of FlAsH/CFP FRET efficiencies of the inactive M1 mAChR in HEK cells measured by BAL treatment. (a) Illustration of the experimental configuration on glass coverslips (gray), gold coated coverslips (blue) (excitation and detection through the cover slip) and flipped configuration (orange) (excitation and emission trough an additional uncoated cover slip). (b) Examples of the fluorescent changes of CFP and FlAsH while adding BAL and resulting FRET efficiency changes for the different experimental configurations. Note the different time axis for the gold flipped configuration. (c) FRET efficiency mean values for the different experimental setups are for uncoated glass 16.3 ± 1.1 % (N=12), for gold coated glass in upright configuration 21.6 ± 1.7 % (N=11) and in flipped configuration 26.3 ± 2.8 % (N=7). Bar graphs represent mean ± SD (of N values), *p=0.02; **p=0.01.*

To demonstrate that increased energy transfer will lead to improved detectability of FRET signals in receptor activation experiments; we investigated the M1 mAChR FRET sensor (figure 4-11). The agonist Iperoxo [199] activates M1 mAChRs and induces conformational changes of the receptor that alter the donor acceptor distances so that donor and acceptor show an increased FRET (acceptor/donor intensity) ratio; a typical experiment is shown in figure 4-11(b). A FRET ratio of 1.0 corresponds to the inactive receptor state, wherby values above 1.0 reflect a FRET gain by receptor activation. The dynamic FRET changes clearly correspond in a concentration dependent manner to the activation by Iperoxo. We monitor the receptor activation of mAChR on glass and on gold coated coverslips both in upright configuration (figure 4-11(c-d)). Note, a flipped configuration is here impracticable when Iperoxo need to be applied locally. Nevertheless, a significantly increased dynamic FRET response is observed. The maximum FRET ratio change increases from 0.051 ± 0.007 on glass to 0.081 ± 0.013 on gold coated glass coverslip, and thus by 58 %. The signal-to-noise ratio of the experiment could be further improved, e.g. in a flipped configuration where the absorbance of the metal layer is not limiting.

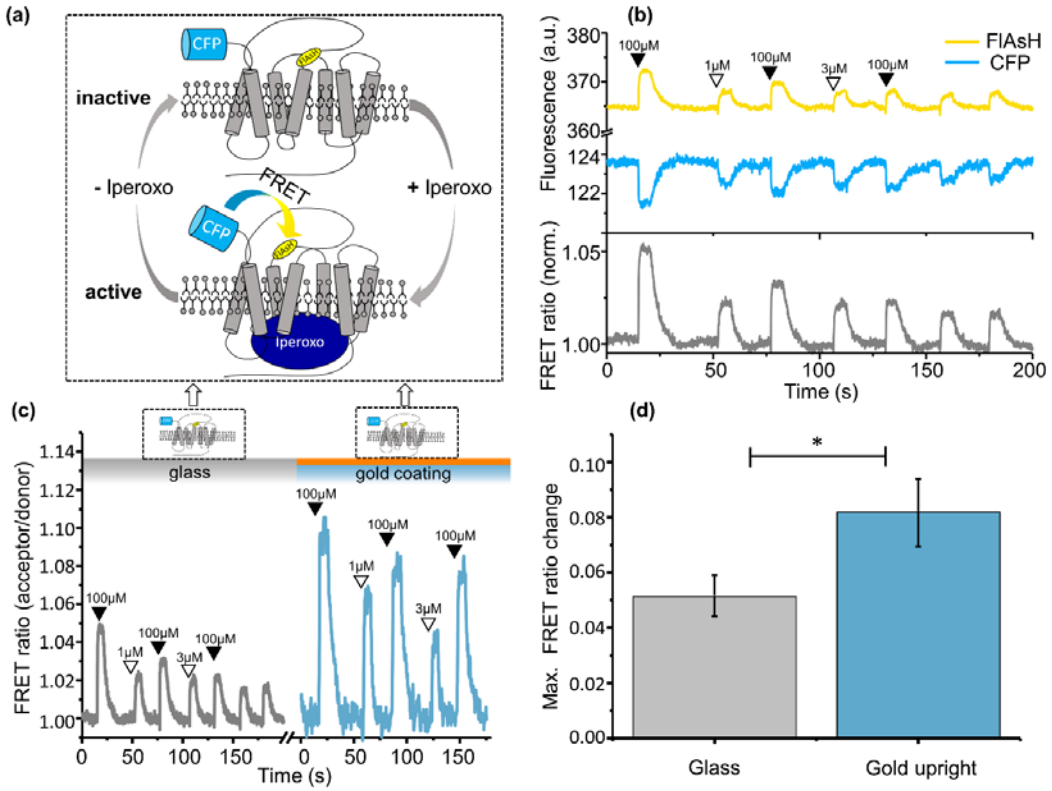

Figure 4-11. *Iperoxo induced FRET changes in FlAsH/CFP-labeled M1 mAChR in HEK cells. (a) Illustration of the agonist Iperoxo induced activation of the M1 mAChR and thus increased FRET signal by conformational changes. (b) Example fluorescence time traces for CFP (cyan), FlAsH (yellow) and the FlAsH/CFP FRET ratio (gray) while adding the agonist Iperoxo. Labels indicate time points and concentrating of the added Iperoxo. (c) Example of FRET ratio changes on glass coverslips and gold coated coverslips. All FRET ratio time traces are baseline corrected and normalized to the FRET ratio of the inactive receptor. (d) Results of the max. FRET ratio on coverslips with and without additional gold coating are 0.051 ± 0.007 (N=7) and 0.081 ± 0.013 (N=6),*p=0.01.*

At a first glance, an increase of FRET ratio without changing the probe is counterintuitive. To understand the mechanism leading to the increased FRET on gold coated coverslips, we performed simulations where we placed an electric dipole emitter in close vicinity to a glass/gold/medium interface with distances varying between 10 nm, 50 nm and 100 nm. In figure 4-12(a) we plotted the calculated logarithmic electric nearfield strength $\log(|\mathbf{E}|^2)$ of the dipole emitter at three different dipole-surface distances (10 nm, 50 nm and 100 nm). Note, 50 nm to 100 nm are typical membrane-coverslip distances for adherent cell lines as previously reported by super-resolution studies [106, 108, 128, 200]. For fluorophores very close (approximately 10-50 nm) to the surface the electric field is able to excite surface waves inside the metallic thin film, known as surface plamons [68]. The interaction strength between the dipole and the metal film is height dependent and decreases for higher distances. Note, the vast majority of donor energy for acceptor excitation in FRET is located in the first nanometers around the dipole emitter even if a surface plasmon is excited. The height dependent changes of emission for a CFP and a FlAsH label in comparison to an uncoated glass surface are plotted in figure 4-12(b). The angular averaged values are depicted where the dipole is 2/3 parallel and 1/3 perpendicular orientated to the surface [83]. Figure 4-12(b) indicates a radiation enhancement for FlAsH close to the surface, while above 70 nm the value drops again with a turning point around 150 nm distances rising afterwards to value comparable to a non-coated glass. CFP shows the same tendency but without reaching a radiation enhancement. Moreover, fluorescence originated at the gold interface is nearly completely absorbed by surface plasmon excitation (see figure 4-12(b) upper right panel). The increased radiation and absorption rate results in a decreased fluorescence lifetime

and quantum yield (figure 4-12b lower left panel) for both molecules in the first 100 nm above the surface. The unmodified quantum yields of CFP (eCFP [201]; *QY* = 0.4) and FlAsH (FLASH-EDT$_2$ [202]; *QY*=0.49) taken from literature are indicated by dashed lines. Taken together, this means that the signal of unspecific, bound fluorescent dyes just at the glass surface vanishes what effectively leads to reduced fluorescence background in an FRET experiment. Figure 4-12(c) shows the height dependent red-shifted fluorescence of CFP. In case of FRET, this stands for an increased spectral overlap integral J. As J is proportional to the FRET rate ($J \propto k_{FRET}$) (this may immediately increases the FRET efficiency. In table 4-1 the results of the height depending emission changes are summarized. Calculations without gold coating are indicated by the index 0. However the plot of $k_{FRET}/k_{FRET;0}$ does not show any significant effect. The reduced donor quantum yield QY_{CFP} and donor radiation rate ratio $k_r/k_{r;0}$ seem to counteract the increased overlap integral. Thus, effectively, the increased FRET efficiency observed in our experiments cannot be explained by metal induced changes of emission properties above reflective surfaces.

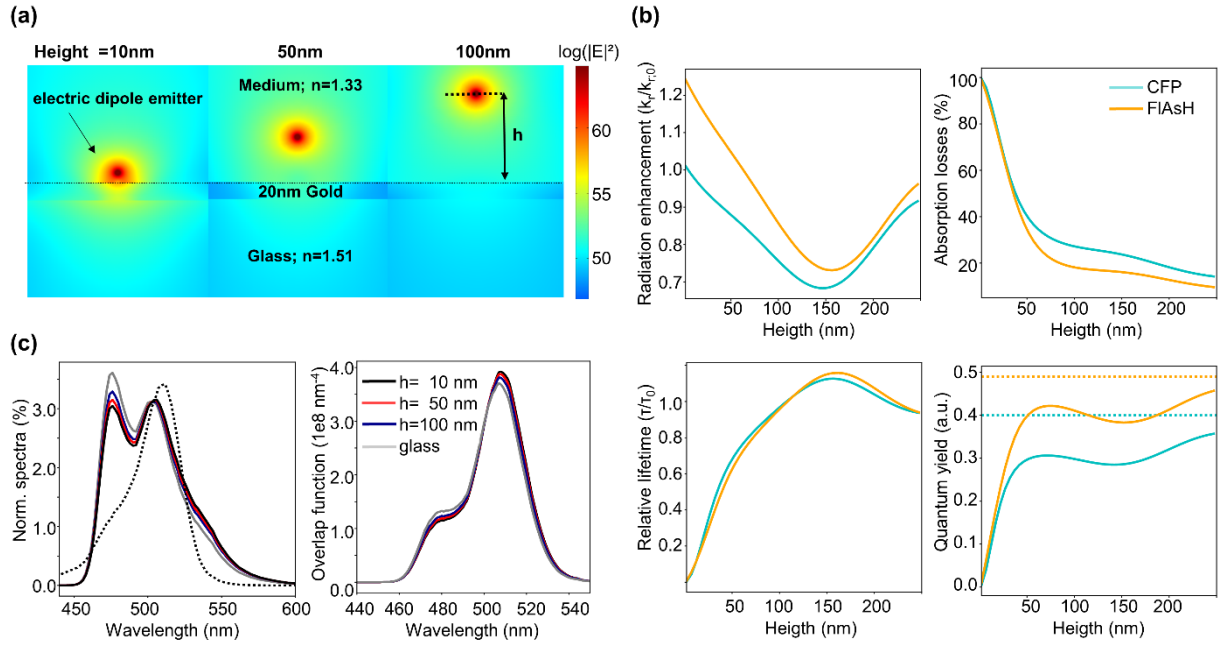

Figure 4-12. *Calculation of the emission property changes of CFP and FlAsH in vicinity of a gold coated glass surface. (a) FEM calculation of the electric field distribution* $|\boldsymbol{E}|^2$ *(logarithmic color bar) for different dipole emitter heights.(b) Height dependent relative changes of the radiative fluorescence rate, the non-radiative losses, relative fluorescent lifetime and the quantum yield on a gold coated glass surface (in comparison to a bare glass surface; average dipole orientation). (c) Height depending spectral emission changes of the CFP resulting a red shift in direction of the FlAsH absorption spectra (dashed lines) and thus an increased CFP-FlAsH spectral overlap function.*

Table 4-1. Calculated fluorescence emissions for different surface-fluorophore distances and average dipole orientation[a]

Height	QY_{CFP}	$k_r/k_{r;0}$	J/J_0	$k_{FRET}/k_{FRET;0}$
10 nm	0.09	0.97	1.021	0.99
50 nm	0.29	0.87	1.012	0.88
100 nm	0.29	0.75	1.009	0.75

[a]*Data taken from figure 4-12.* [b]*CFP quantum yield refers to 0.4 in free space.[201]*

Next, we hypothesize that the FRET enhancement may originate from changes in the electric nearfield of the donor molecule. To test this, we simulated the electric nearfield in a 10 nm radius around the donor molecule as shown in figure 4-13. Panel 4a shows the electric nearfield log($|\mathbf{E}|^2$) and the electric field orientation of an in-plane aligned dipole without (w/o) and with (w/) gold coating at the glass surface. The plot clearly shows that the coating has an influence on the electric nearfield indicated by tilted electric field orientation. We test the impact of the nearfield enhancement factor $\langle|\mathbf{E}|^2\rangle/\langle|\mathbf{E}_0|^2\rangle$ on the FRET rate $k_{FRET}/k_{FRET;0} \propto \langle|\mathbf{E}|^2\rangle/\langle|\mathbf{E}_0|^2\rangle$ in figure 4-13(b) depending on the distance to the donor dipole. It turns out that in the first nanometer around the dipole the FRET rate cannot be noticeably affected by the gold coating. Consequently, we can also exclude electric nearfield enhancing as a reason for increased FRET efficiencies.

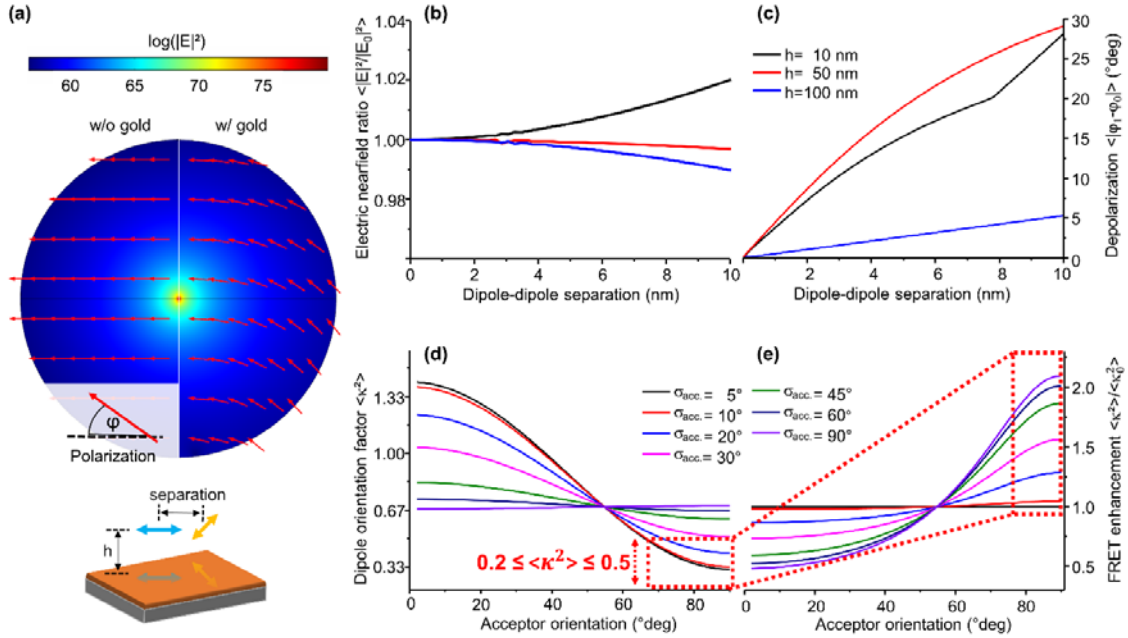

Figure 4-13. Calculation of donor electric field changes in vicinity of the gold coating. (a) Finite element calculation of the donor near field ("side-view", sphere radius 10 nm, dipole parallel to the surface) on a coverslip w/o and w/ gold coating. Color showing the logarithmic electric field strength $|\mathbf{E}|^2$ and red arrows indicating the polarization of the electric field. (b-c) acceptor dipole separation dependent on electric nearfield ratio $\langle|\mathbf{E}|^2/|\mathbf{E}_0|^2\rangle$ and depolarization $\langle|\phi-\phi_0|\rangle$for different donor heights. (d-e) Calculation of $\langle\kappa^2\rangle$ and $\langle\kappa^2\rangle/\langle\kappa_0^2\rangle$ for randomly orientated donor molecule against acceptor orientation for different acceptor orientation distribution width $\sigma_{acc.}$. In our experiments, $\langle\kappa^2\rangle$ is between 0.2 and 0.5, corresponding acceptor orientations and possible $\langle\kappa^2\rangle/\langle\kappa_0^2\rangle$ enhancements are indicated by the red boxes.

Finally, by exclusion, we must have found the reason for increased FRET efficiencies in our FRET sensor construct. As no further mechanism comes to mind, the effect must be driven by virtual depolarization of the acceptor molecule und thus a reinforcement of the $\langle\kappa^2\rangle$ value of our donor-acceptor pair. This FRET enhancement mechanism was previously described by de Torres and co-worker`s [198] whereby the FRET rate enhancement corresponds to $\langle\kappa^2\rangle/\langle\kappa_0^2\rangle$. They compared FRET pairs with different donor-acceptor orientation factor in photonic environments effecting $\langle\kappa^2\rangle/\langle\kappa_0^2\rangle$. They found that for low $\langle\kappa^2\rangle$ FRET efficiency can be improved.

As shown in the electric nearfield calculations (see figure 4-13(a)) the electric field polarization of the molecules are effected by the mirror-like metallic coating. The vector arrows in figure 4-13(a) are deflected compared to the case without metallic coating. Induced by the metal coating one can see a virtual depolarization $<|\phi\text{-}\phi_0|>$ of up to 30° (figure 4-13(c)). We know from our FRET sensor that the donor (CFP) is attached at the C-terminal end of the GPCR and thus can strongly fluctuate. In contrast the acceptor FlAsH is a bidentate lable and therefore stiffly attaches to the third intercellular loop (IL3). Based from this knowledge we plot $<\kappa^2>$ for a randomly orientated CFP molecule against an acceptor orientation with different possible dipole orientation distribution widths σ_{acc} (for the detailed equation see the work of Dale and co-workers [61]). An acceptor orientation of zero degree represents a parallel orientation of acceptor and donor in the projection plane. In this case $<\kappa^2>$ is maximized for parallel donor-acceptor dipole orientations when the acceptor orientation distribution width σ_{acc} is nearly zero. For perpendicular orientations the value of $<\kappa^2>$ drops to 1/3, but never becomes zero as for the more stiff (less fluctuating) dipoles. When increasing the degrees of freedom for the acceptor orientation the $<\kappa^2>$ converges against 2/3 for all acceptor orientation mean values. This represents the value that is frequently found in literature and describes the dipole-dipole orientation factor of homogenous freely orientated donor and acceptor molecules. From our experiments we know that the FRET efficiency on glass is 16.3 %. We also know from the M1 mAChR crystal structure that the mean FlAsH CFP distance is 3.4 nm [203]. By comparison our measured FRET efficiency with the theoretical FRET efficiency (for $<\kappa^2>$ = 2/3) we can profoundly estimate dipole-dipole orientation factors of $<\kappa^2>^M$=0.2…0.5 (for distances of 1.9 to 4.9 nm; label position distance ± CFP diameter (~3 nm)). Obviously, the $<\kappa^2>$ value for our FRET sensor is below the $<\kappa^2>$ value for randomly orientated molecules. Thus, we postulate that the FlAsH molecule is perpendicular orientated to the CFP molecule so that FRET is not perfect (see red box in figure 4-13(d)). Thanks to the specific electric field depolarization properties of our gold coating the FlAsH orientation distribution is virtually broadened and σ_{acc} is increased. For different acceptor orientations, figure 4-13(e) shows a plot of $<\kappa^2>/<\kappa_0^2>$, which is proportional to the FRET rate enhancement $k_r/k_{r;0}$. By virtual depolarization of the electric near field the value for $<\kappa^2>/<\kappa_0^2>$ can increase up to 200% for a dipole with low $<\kappa^2>$ starting values. This reinforced FRET is induced by the metallic coating allowing an otherwise forbidden FRET at that dipole orientation. In contrast, for optimal donor-acceptor orientations with $<\kappa^2>$ above 2/3 FRET efficiency the opposite effect would be possible, so that the FRET efficiency will be even decreased by the virtual electric field depolarization. Fortunately, the case of non-ideal orientation and a non-ideal FRET system is much more likely in a realistic cellular setting so that the typical FRET application is likely to benefit from gold coated coverslips.

Conclusion and perspectives

We have shown that gold coatings can increase the fluorescence energy transfer between a donor and acceptor molecule. This is demonstrated by a CFP-FlAsH FRET sensor system developed for mAChRs in living cells. The gold coatings increased the FRET efficiency by up to 61 % and thus allow monitoring dynamics of ligand binding induced conformational changes in GPCRs by FRET with increased signal responses. The best signal to noise values and enhancement results were experimentally achieved by the flipped gold coated coverslip configuration were imaging through the metal is avoided. Thus, in future it would be beneficial to equip the inverted FRET microscope with an upright detection path to further minimize signal losses. An upright detection path would even allow a combination with prism or objective based (conventional or surface plasmon resonant) total internal reflection fluorescence microscopy [64, 125, 156, 157, 167], which would further extend the tool box by providing a high level of optical sectioning.

In the present work, we also dissected the mechanism of the observed FRET enhancement, and confirm that the increased FRET responses are not based on metal induced spectral emission changes

and nearfield enhancements effects. Instead we showed that, at least in our experiments, the mechanism of increased FRET is given by changes in the electric nearfield polarization. FEM calculations indicated that the effect is (solely) driven by virtual optimization of the donor-acceptor dipole orientation. As the enhanced FRET effect is based on polarization changes in the electric dipole nearfield, other coating approaches could also be explored. Particularly interesting would be randomly or anisotropic aligned metallic nanoparticle and nanowire films which can be easily fabricated on wafer scales with selective optical properties [204-209]. These approaches may be able to selectively improve the dipole orientation factor in the spectral FRET overlap area while neither illumination nor detection will be negatively influenced.

In summary, we believe that enabling forbidden FRET (*for*FRET) pathways as demonstrated in our *for*FRET approach has particular potential to be applied in pharmaceutical high-throughput drug screening. The *for*FRET approach allows to boost non-ideal FRET probes, and thus amplify signal responses without interfering with the well-characterized molecular assay.

Methods

Coverslip coating: The metal coating was performed in a vacuum deposition chamber (HEX, Korvus technology, United Kingdom) by electron beam evaporation. Glass coverslips as substrates were cleaned by acetone and isopropanol. The deposition was started when a base-pressure ~10^{-6} mbar was reached. The coating consists of an adhesion layer of 2 nm chromium (99.95 %, Goodfellow, United Kingdom) followed by 20 nm gold (99.99 %, EVOCHEM GmbH, Germany). The layer thickness were controlled by a quartz crystal microbalance during deposition and afterwards checked by spectroscopic ellipsometry (alpha-SE, J.A. Woollam, United States). Additionally, average (root mean square) roughnesses of 1.6 nm for the gold coated and 0.5 nm for uncoated coverslips were determined by atomic force microscopy (AFM) using a Molecular Force Probe MFP-3D system (Asylum Research) and AC240TS probes (Olympus). Coverslips were washed with ethanol before culturing cells.

FRET sensors: An established M1 mAChR FRET sensor was used and stably expressed in HEK293 cells as previously described [23, 24]. The construct contains eCFP at the C-terminal receptor end and the FlAsH binding motif is localized within the third intercellular loop (IL3) as described previsouly [24].

Cell culture: HEK293 cell line (stably expressing the FRET sensor) were cultured in cell medium (DMEM with 4.5 g L^{-1} 10 % (v/v) FCS, 100 U mL^{-1} penicillin, 100 µg mL^{-1} G-418) at 37 °C by 7 % CO_2. For FRET experiments cells were grown on gold coated or bare glass coverslips that were both pre-treated with poly-D-lysine. Prior to use, both types of coverslips were sterilized with 100 % ethanol followed by two washing steps with PBS. For FlAsH labeling we followed the published general procedure [22]. In brief, cells were washed with buffer and incubated in labeling buffer containing 500 nM FlAsH and 12.5 µM 1,2-ethandithiol for 1h at 37 °C. Afterwards non-bound FlAsH were removed by incubating the cells for 10 min with labeling buffer containing 250 µM EDT. The cells were subsequently cultured in DMEM again.

FRET measurements: An inverted microscope (Axiovert, Zeiss, Germany) equipped with a 100x oil objective (numerical aperture = 1.3, PLAN-Neofluar, Zeiss) were used for FRET experiments. For excitation at 436 nm a polychromatic light source (Till Photonics, FEI Munich GmbH, Germany) was used coupled into the microscope by a longpass dichroic mirror (LP460 nm), and the fluorescence additionally filtered by a dielectric bandpass filter (480/40 nm and 535/30 nm; for CFP and FlAsH) and recorded by photodiodes. Illumination and acquisition time per 10 Hz frame was 40 ms and 100 ms, respectively.

For chemical bleaching (repressing the FlAsH label from binding) 1,2-dimercapto-1-propanol (British Anti-Lewisite, BAL) (final concentration 5 mM) was added (Jost *et al.*[210]). FRET efficiencies from BAL treatment experiments were confirmed by classical acceptor photobleaching experiments.

For receptor activation experiments a perfusion needle was positioned next to the cell of interest expressing the M1 receptor sensor. As described before cells were continuously superfused with a physiological measuring buffer resulting in a basal FRET signal. By switching the perfusion channel to Iperoxo [199] (dissolved in measuring buffer) in saturating or subsaturating concentrations (figure 4-11) a clearly concentration dependent increase in FRET ratio could be observed. After reaching a constant signal within a few seconds perfusion was switched back to buffer so that the signal dropped again the baseline level. The “gold flipped” configuration was not possible for this experiment since this configuration obstruct the positioning of the perfusion needle next to the cells.

Data and statistical analysis: Fluorescence acquisition and data analysis were performed using Clampex, Clampfit (Axon Instruments, USA) and OriginPro 2017 (OriginLab, USA). For acceptor bleaching experiments the FRET efficiency is calculated from donor cahnnel intensities before (I_{DA}) and after (I_D) acceptor bleaching by $E_{FRET} = 1 - I_{DA}/ I_D$. No FlAsH or metal flourescecne were observed in the CFP channel. For receptor activation traces we corrected the acceptor channel (I_A) for CFP bleed through ($\alpha = 0.57$). The FRET ratio (donor/acceptor) = $(I_A - \alpha I_{DA})/I_{DA}$. In addition, traces were corrected for photobleaching by applying baseline subtraction. All data are shown as means ± S.D. for *N* independent observations.

Simulations and Modelling: Finite element method (FEM) simulations of dipole emitter properties were performed with Comsol Multiphysics™ 4.4 (Comsol Inc., USA) software using the wave optics module. FEM calculation provides electric field vector E and the angle depending dipole emission power $P(\vartheta)$. The total k_{tot} and radiative k_r dipole emission rate is given by ring integration next to the emitter and at the geometry boundary. Calculations are performed for a dipole emission of different wavelengths and heights above a 20 nm gold coated and uncoated medium/glass interface with refractive indices of 1.33/1.51. With optical constants derived from Johnson and Christy [211] fluorescence quantum yield, lifetime and energy transfer rates are calculated [68, 83, 84, 194] for the described geometry.

5 Discussion

This section presents three different strategies to improve total internal reflection fluorescence (TIRF) microscopy and fluorescence resonance energy transfer (FRET). Within this work, I sought to use these approaches to overcome limitations based on TIRF illumination and the nature of fluorescence, which are bottlenecks for the imaging of cell membrane dynamics. The first approach increases image homogeneity and reduces imaging artifacts with a 360° oblique TIRF illumination. The second approach increases imaging contrast in high background environments by using plasmonic nanocoatings. In the third strategy, plasmonic nanocoatings enhances signals of FRET-sensors attached on GPCRs in the intact cell membrane. Further detailed discussions are in the corresponding section of publications in the results section of this thesis. In the following paragraphs, I discuss various aspects of the three approaches.

Flat-top and axial-selective membrane imaging with AxiTIRF

In order to improve TIRF-M image homogeneity and reduce TIRF imaging artifacts, I developed the AxiTIRF [125]. The AxiTIRF uses a laser ring to achieve an all-sided, and overcritical TIRF illumination. I demonstrated that a 360° "ring" illumination prevents typical TIRF artifacts. In contrast to this method, other typical "ring" TIRF methods use annular incoherent illumination [47, 135] or annular spinning laser spot illumination [126, 212, 213]. In addition, AxiTIRF generates a flat-top illuminated FOV, while the previously mentioned "ring" TIRF approaches have a Gaussian illuminated FOV. An even flat-top TIRF illumination is a significant advantage since it allows a direct comparison of fluorescence across the entire FOV, which is beneficial for cell membrane imaging.

Different publications have already explored flat-top illumination in wide-field microscopes and its benefits [141, 214, 215]. Unfortunately, these approaches are not suitable for axial-selective TIRF illumination. AxiTIRF-M is ideal for homogenous and axial-selective cell membrane imaging. The disadvantage of the AxiTIRF is the Bessel-beam center spot, since the most excitation intensity is stored there. This central spot, compared to the remaining flat-top illuminated FOV, induces more fluorescence bleaching and phototoxic effects. Nevertheless, the homogenously illuminated TIRF and the sub-diffractive center spot are both useful for cell membrane imaging and single molecule applications, as I will discuss in the further perspectives section.

Active fluorescent background suppression with fluoplasmonic (f-Pics) nanocoatings

Surface plasmon-coupled emission (SPCE) is the effect which makes f-Pics suitable for axial-selective imaging of the cell membrane, while out-of-focus fluorescent background is actively suppressed. With f-Pics, TIRF-M can image cell membranes with a sufficiently high contrast, even if four times more background is applied in comparison to TIRF-M with standard coverslips.

However, even the f-Pics background suppression effect is enormous in a TIRF setting; the disadvantages make f-Pics hardly suitable for single-molecule applications. The semitransparent coating and ohmic losses inside the metal layer reduce the photon collection efficiency, and the point spread function (PSF) broadening reduces spatial resolution [169, 170]. A quantum yield (QY) modification occurs in the vicinity of the coating that reduces the brightness of high QY dyes. This modification is beneficial for low QY fluorophores; this QY enhancement is not strong enough for low QY molecules to become brighter than high QY molecules. In my opinion, even if problems with PSF broadening and ohmic losses are solved (e.g., with approaches described in [169, 170] and [173]), f-Pics is particularly unsuitable for single molecule studies in an epifluorescence setting. The reason is that the primary mechanism of background suppression is based on the coatings being semi-transparent, and only a part of the near field fluorescence is mediated through the coating [80, 81].

Therefore, decreased signal detection efficiency must be considered if f-Pics is used for TIRF microscopy.

Enhanced signals to probe GPCR activation dynamics with *for*FRET nanocoatings

Some reasons for low FRET efficiency in GPCR studies may include donor and acceptor distances being too high, the dipole-dipole orientation being imperfect, or the environment between both molecules disrupting the energy transfer. The issue with low FRET changes is that signal collection time needs to be increased, leading to reduced observation speed and rendering it impossible to follow GPCR dynamics, especially for single molecules. As previously discussed, GPCR activation dynamics are typically in the range below 100 milliseconds. To resolve these dynamics, sufficient signal needs to be detected using a doubled sampling rate. Unfortunately, low fluorescence photon yields make it difficult to overcome these limitations using current methods, especially in the case of the single molecule.

As demonstrated, gold nanocoatings enhance the direct donor-acceptor energy transfer in a CFP-FlAsH sensor labeled on a muscarinic M1 receptor in a living cell. This enhanced FRET is based on enabling forbidden FRET (*for*FRET) of imperfect donor-to-acceptor orientation by nanocoating induced photonic depolarization. With FEM simulations, I can demonstrate that nanocoating-induced fluorescence depolarization is the reason for the FRET enhancement. In addition, the results are in agreement with experiments of the work of de Torres et al. [53] To my knowledge, this is the first time were enhanced FRET in a pharmaceutical relevant GPCR setting has been presented. With *for*FRET, the FRET efficiency enhancement is around 60%. In addition, with *for*FRET, the FRET efficiency contrast between active and inactive receptors increases up to 60%. This important result creates opportunities for FRET signal enhanced ligand screening applications. With this enhanced FRET contrast, the observation of ligand-induced activation dynamics can be beneficially improved, which are also suitable for single molecule FRET applications. I will subsequently discuss potential pharmacological applications.

A disadvantage of *for*FRET is that only FRET sensors with imperfect dipole-dipole orientations will profit from the depolarization effect. For FRET constructs with a high $\langle\kappa\rangle^2$ value, the nanocoatings will reduce the energy transfer. However, *for*FRET is not necessary for sensors with high $\langle\kappa\rangle^2$ values and high FRET efficiencies. This means that this disadvantage of *for*FRET is not relevant in practice. In addition, *for*FRET has the same disadvantages as f-Pics when the coated coverslips are implemented into an epifluorescence microscope. Strategies to improve *for*FRET coatings will be discussed subsequently.

Discussion summary

I worked on three approaches to enhance membrane imaging and spectroscopy. In particular, the *for*FRET and the AxiTIRF demonstrated notable benefits for cell membrane imaging and FRET-based spectroscopy and the discussed disadvantages and limitations are solvable. All aims of this thesis are achieved, albeit with limitations.

At this point, the limitations of the nanocoatings make them unatractive for single-molecule GPCR research. In the next section, I will discuss potential developments to improve the nanocoatings to make them suitable for single-molecule applications. I believe that once the problems are solved, all their methods have enormous potential for GPCR research. The next section identifies strategies for further improvement.

6 Future prospective

Based on the results of this work, I will discuss ideas for further developments and potential applications of the presented methods. There is enormous potential for GPCR research, especially for the flat-top illuminated AxiTIRF and the FRET booster coatings. Few limitations need to be mastered before implementation of these methods. The following section will detail suggestions for improvements, experiments, and ideas for implementation of the abovementioned methods.

Evanescent Bessel-beam illumination for single-molecule studies

The AxiTIRF generates an even and flat-top illuminated FOV, while in axial direction, the excitation field is evanescently decaying. The benefits of such illumination have been discussed above. This subsection explains how this method is suitable for single molecule studies in the future.

An interesting application for AxiTIRF is super-resolution imaging with the single molecule localization microscopy (SMLM) approach. The SMLM approach enables super-resolution microscopy by recording "blinking" events of fluorescent markers and subsequently involves computer-based localization and geometry reconstruction [216-218]. The SMLM approach is particularly useful to study cell membrane receptor organization [40-43]. Several publications present the advantages of flat-top illuminated SMLM: the approach allows for enhanced localization precision over the whole FOV [141, 214, 215] in comparison to standard illumination methods. Unfortunately, flat-top illuminated TIRF-M is not possible with those approaches. Thus, the AxiTIRF is the first method that could achieve flat-top illuminated TIRF-M for cell membrane-selective super-resolution microscopy.

The AxiTIRF also has potential for FCS, which is suitable for measuring the diffusion dynamics of the GPCRS on the cell membrane. The Bessel-spot is tunable for FCS applications, since the central spot becomes more dominant through the reduction of the laser input diameter. In addition, the Bessel-function central spot is smaller than the optical diffraction limit in the lateral direction and has an evanescent intensity decay in axial direction. Thus, this sub-diffractive evanescent excitation spot enables the opportunity for super-resolved and cell membrane-selective FCS. This highly confined observation volume has the advantage of permitting the direct observation of millisecond dynamics on spatial scales below the diffraction limit [219, 220].

The mechanism behind *for*FRET: Open questions and experimental approaches

Experiments and numerical simulations confirm FRET enhancement for direct donor-to-acceptor energy transfer next to metal nanocoatings. However, from my point of view, the mechanisms behind *for*FRET are yet not fully understood. One issue is whether FRET enhancement is predictable enough for nanocoatings to be designed in silico. Numerical calculation suggests that the electric field and the polarization of the dipoles are influenced by the metallic surface. These fluorescence modifications are different in lateral and axial direction. Because of this, the FRET enhancement seems to be inhomogeneous in all directions. Thus, the question is whether *for*FRET disturbs the "nanoruler" applicability of FRET sensors. To prove this, the well-known FRET "step" function needs to be re-evaluated near *for*FRET coatings. For such experiments, FRET measurements in lateral and axial directions need to be performed. For the lateral direction, DNA oligomers [166] are useful to control the distance and orientation of the FRET molecules. For the axial direction, polymer spacers [167, 221] and curved surfaces [87, 222] can control the separation between the FRET construct and the *for*FRET coating.

The enhanced FRET presented in this study was performed by ratiometric fluorescence measurements. Because of this, I suggest a comparison with fluorescence lifetime spectroscopy [166, 193]. Fluorescence lifetime spectroscopy provides information on emission rates, which is useful to gain new insights on the physics of *for*FRET. For example, Bidault et al. [189] demonstrate a competition between FRET enhancement and plasmonic excitation, with the result of decreasing FRET. In contrast, Vos et al. [196, 197] demonstrate a lack of correlation between FRET rates and the localized photonic densities of states (LDOS). It is not clear if this is a contradiction and if it is not, whether plasmonic effects can be turned into the direction to increase FRET. Answering this question leads to the conclusion that FRET enhancement for direct donor-to-acceptor energy transfer is solely due to depolarization effects or that there are more underlying mechanisms. However, this researcher suggests performing additional FRET measurements in different strong LDOS environments and for sensors with different $\langle\kappa\rangle^2$ values.

***for*FRET for pharmaceutical research and applications**

As discussed, enhanced FRET has potential for biological and pharmaceutical research. In addition, the implementation of biocompatible *for*FRET nanocoatings is possible for all FRET-based live-cell applications. For example, one potential application is transmembrane FRET on GPCRs, which has not been reported so far. However, it is unclear if *for*FRET can enhance the energy transfer to detect transmembrane FRET. If the answer is yes, more opportunities for labeling positions in FRET sensors become possible, since *for*FRET increases the FRET detectability even for imperfect label orientations and distances. As an idea, transmembrane FRET opens new possibilities to study GPCR hetero oligomerization. Here, one receptor type is intracellularly labeled and the other is extracellularly labeled. This labeling concept increases the FRET-based detection certainty of GPCR hetero oligomerization. In addition, the orientation of the GPCRs in heterodimers becomes resolvable by distance, depending on FRET efficiencies.

Another application involves several well-established FRET sensors only displaying very low FRET signals. Here, forFRET can solve the problem of undistinguishable FRET changes between active and inactive state of the GPCRs. As discussed, *for*FRET boosts the FRET contrast of active and inactive states in live-cell GPCR experiments [133]. This enhanced FRET contrast would allow for the increasing of acquisition speed to monitor GPCR dynamics. Specifically, constructs with nearly no FRET contrast would benefit from *for*FRET if the dipole-dipole orientation were the issue. In order to use *for*FRET in pharmaceutical ligand screening, it is necessary to test if the shape of ligand concentration response curves (e.g., see reference [24]) stays unaffected from *for*FRET while the SNR of the measurements increases. If this is the case, *for*FRET has the potential for signal enhanced FRET-based screening applications, which are especially suitable for high-throughput applications in microplate reader-based methods [223].

Alternative nanostructures for enhanced FRET and SNR improved imaging and spectroscopy

F-Pics and *for*FRET nanocoatings improve various aspects of membrane-selective imaging and spectroscopy. Unfortunately, continuously metal films are semitransparent, and thus signal losses must be considered if fluorescence is collected through the coating. This section will discuss alternative nanomaterials that are suitable for enhanced FRET and SNR-improved membrane imaging and spectroscopy.

Zero-mode wave-guides

Subwavelength nanoholes operate as zero-mode wave-guides (ZMWG) [224]. Both, excitation light and fluorescence are not able to penetrate through the ZMWGs, but their electric field can evanescently propagate inside the holes. As a result, fluorescence is detectable through the nanostructured layers if its molecule is located inside or closely above a ZMWG. Similarly to f-Pics, ZMWGs are very efficient in the axial separation of the fluorescent molecule locations; thus, ZMWGs prevent the detection of out-of-focus fluorescence. In addition, ZMWGs are very powerful for high SNR spectroscopy for fast and high-throughput DNA sequencing [225].

The group of Jerome Wenger [226, 227] used planar plasmonic antennas in nanostructured ZMWGs for high contrast cell membrane imaging and spectroscopy. As an additional feature, the observation volume is reduced compared to standard FCS, which enables the studying of faster diffusion dynamics and higher lateral discrimination, thereby empowering this technique for the study of lipid "rafts" nanodomains on the cell membrane [34]. The existence of lipid rafts and the organization of GPCRs inside them is still a highly discussed topic in research [228]. With such ZMWG nanostructures, "lipid raft" hypothesis can be tested.

However, the limitation of ZMWGs is that they are not suitable for large-scale fabrication, since this nanostructure requires precise nanofabrication. A high amount of substrate is essential for research on cells, since the substrate need to be changed for each experiment. The reuse of nanostructures might be an option, but to culture cells on fresh substrates is preferred. To solve this issue, self-organized or nanoimprinted nanoholes, nanopillars, and nanowire structures might be alternatives [209, 229-231].

Self-organized homogenous or anisotropic metal island films (MIFs)

Metal island films (MIFs) are an alternative to continuous nanocoatings. Metal island films support the excitation of localized surface plasmon resonances (LSPRs). The benefit of LSPRs is that they absorb light at specific wavelengths; thus, MIFs are highly transparent in the remaining spectral regime. In addition, MIFs have light depolarization effects [204-206] and are therefore candidates to enhance FRET, similar to *for*FRET coatings. To summarize, MIFs are good nanocoating candidates for enhanced FRET, since the fluorescence detection in an epifluorescence setup is increased compared to continuously nanocoated coverslips.

The fabrication effort of MIFs and continuous nanocoatings are equivalent. In addition, the deposition parameters and optional post-deposition annealing tune the LSPR [232]. Metal deposition on templates, like pre-structured surfaces or nanosphere monolayers, allows for large-scale fabrication of plasmonic nanostructures with multidirectional LSPRs [233, 234]. These nanostructures can be designed to be transparent for the acceptor fluorescence, while LSPRs are spectrally located at donor excitation and emission maximum.

Colloidal particles for nanostructured plasmonic films

Colloidal nanoparticles fabricate plasmonic nanostructures, similar to MIFs [235]. The difference is that no deposition system is required for colloidal particles. To fabricate such nanostructures, the colloidal nanoparticles are added directly to any substrate, and the particles are immobilized onto a surface or polymer. The geometry of colloidal particles is well-defined and allows for high reproducibility of the nanostructures. Luan et al. [236] recently presented a "plasmonic patch" based on a flexible polymer film with adsorbed colloidal plasmonic nanoparticles. The authors demonstrate how plasmonic patches enhance signals in fluorescence-based immunoassays. I suggest placing plasmonic patches into multi-well microtiter plates for optimization of *for*FRET on a high-throughput scale. In addition,

implementation of plasmonic patches into multi-well plates allows FRET measurements that are signal enhanced and parallelized. Parallelized FRET measurements are particularly useful for high-throughput determination of ligand concentration responses of GPCRs [223].

Flat-top illumination TIRF methods with plasmonic nanostructures for single molecule and high-throughput applications to study GPCR dynamics

Splitting the excitation and emission path allows for direct combination of the flat-top illumined AxiTIRF with plasmonic nanocoating. For example, a decoupled excitation and emission path is the case in prism-based (e.g., [156]) or chip-based [237] TIRF geometries. The advantages include flat-top illuminated axial selective imaging, and the signal does not propagate through the metal coating for detection. Because of this, signal losses through the coatings are reduced. Heil et al. [238] demonstrate that a reflective surface increases the fluorescence that collects into such an opposite detection path. This effect is particularly useful for enhancing the localization precision and resolution in SMLM.

As an additional benefit of this TIRF geometry, the detection path is not limited to high NA objectives. This provides the opportunity to increase the FOV for TIRF-based SMLM or FRET studies. For GPCR activation studies, a flat-field illumination over a large FOV in combination with enhanced FRET solves different photophysical problems. In detail, the illumination is homogenous over a large FOV, an evanescent excitation field prevents an out-of-focus background, *for*FRET enhances the FRET efficiency, and fluorescence signal collection is improved by the reflective surface. Since the FRET signal and fluorescence SNR are enormously increased, it becomes possible to overcome the current temporal limitations of FRET-based techniques. In summary, the recording of high-speed GPCR activation dynamics becomes possible.

Concluding remark

In this thesis, I developed methods to enhance fluorescence signals with the aim of monitoring GPCR dynamics in cell membranes. The cell membrane is a very important place where important GPCR-signaling events are induced by ligand binding. However, the complete GPCR signaling cascade does not takes place in the cell membrane, since GPCR activation also triggers intracellular mechanisms.

For the monitoring of whole ligand-induced GPCR signaling cascades, combination with other methods is essential to follow processes inside living cells. Well-established methods for correlative imaging include wide-field imaging, confocal laser scanning, and selective plane illumination microscopy (SPIM) [14, 144].

These methods are also suitable for FCS, which enables the opportunity to study dynamics of GPCRs and other proteins related to signaling. I have demonstrated that metallic nanostructures allow for enhanced fluorescence signals in the cell membrane. Inserting plasmonic nanostructures into the cell are a potential approach to enhance fluorescence signals inside the cell. However, for this approach, it is advisable to check the nanoparticle influence on molecular processes.

Nonetheless, especially fast GPCR processes in the cell membrane are still under investigation, since these processes cannot be temporally resolved. The reason for this is that low or noisy fluorescence signals require long acquisition times. Therefore, methods presented in this work, which increase the fluorescence signal and detection efficiency, have the potential to increase the acquisition speed for membrane selective imaging. It is exciting to see if the implementation of these methods provides new insights into receptor research.

7 References

1. Cuatrecasas, P., *Membrane Receptors.* Annual Review of Biochemistry, 1974. **43**: p. 169-214.
2. Dautzenberg, F.M. and R.L. Hauger, *The CRF peptide family and their receptors: yet more partners discovered.* Trends in Pharmacological Sciences, 2002. **23**(2): p. 71-77.
3. Hauser, A.S., et al., *Trends in GPCR drug discovery: new agents, targets and indications.* Nature Reviews Drug Discovery, 2017. **16**(12): p. 829-842.
4. Gregorio, G.G., et al., *Single-molecule analysis of ligand efficacy in beta(2)AR-G-protein activation.* Nature, 2017. **547**(7661): p. 68-+.
5. Latorraca, N.R., A.J. Venkatakrishnan, and R.O. Dror, *GPCR Dynamics: Structures in Motion.* Chem Rev, 2017. **117**(1): p. 139-155.
6. Lohse, M.J. and K.P. Hofmann, *Spatial and Temporal Aspects of Signaling by G-Protein-Coupled Receptors.* Molecular Pharmacology, 2015. **88**(3): p. 572-578.
7. Hilger, D., M. Masureel, and B.K. Kobilka, *Structure and dynamics of GPCR signaling complexes.* Nature Structural & Molecular Biology, 2018. **25**(1): p. 4-12.
8. Sorkin, A. and M.A. Puthenveedu, *Clathrin-Mediated Endocytosis*, in *Vesicle Trafficking in Cancer*, Y. Yarden and G. Tarcic, Editors. 2013, Springer New York: New York, NY. p. 1-31.
9. Sundborger, A.C. and J.E. Hinshaw, *Regulating dynamin dynamics during endocytosis.* F1000Prime Rep, 2014. **6**: p. 85.
10. Di Fiore, P.P. and M. von Zastrow, *Endocytosis, signaling, and beyond.* Cold Spring Harb Perspect Biol, 2014. **6**(8).
11. Wettschureck, N. and S. Offermanns, *Mammalian G proteins and their cell type specific functions.* Physiological Reviews, 2005. **85**(4): p. 1159-1204.
12. Tilley, D.G., *G Protein-Dependent and G Protein-Independent Signaling Pathways and Their Impact on Cardiac Function.* Circulation Research, 2011. **109**(2): p. 217-230.
13. Milligan, G. and E. Kostenis, *Heterotrimeric G-proteins: a short history.* British Journal of Pharmacology, 2006. **147**: p. S46-S55.
14. Xu, X., J.A. Brzostowski, and T. Jin, *Monitoring dynamic GPCR signaling events using fluorescence microscopy, FRET imaging, and single-molecule imaging.* Methods Mol Biol, 2009. **571**: p. 371-83.
15. Tian, H., A. Furstenberg, and T. Huber, *Labeling and Single-Molecule Methods To Monitor G Protein-Coupled Receptor Dynamics.* Chem Rev, 2017. **117**(1): p. 186-245.
16. Lohse, M.J., S. Nuber, and C. Hoffmann, *Fluorescence/Bioluminescence Resonance Energy Transfer Techniques to Study G-Protein-Coupled Receptor Activation and Signaling.* Pharmacological Reviews, 2012. **64**(2): p. 299-336.
17. Sergeev, M., et al., *Ligand-induced clustering of EGF receptors: a quantitative study by fluorescence image moment analysis.* Biophys Chem, 2012. **161**: p. 50-3.
18. Szidonya, L., M. Cserzo, and L. Hunyady, *Dimerization and oligomerization of G-protein-coupled receptors: debated structures with established and emerging functions.* J Endocrinol, 2008. **196**(3): p. 435-53.
19. Marx, V., *Probes: FRET sensor design and optimization.* Nat Methods, 2017. **14**(10): p. 949-953.
20. Granier, S., et al., *FRET-based measurement of GPCR conformational changes.* Methods Mol Biol, 2009. **552**: p. 253-68.
21. Hoffmann, C., et al., *A FlAsH-Based FRET Approach to Determine G Protein - Coupled Receptor Activation in Living Cells.* Nature Methods, 2005. **2**(3): p. 171-176.
22. Hoffmann, C., et al., *Fluorescent Labeling of Tetracysteine-Tagged Proteins in Intact Cells.* Nat Protoc, 2010. **5**(10): p. 1666-77.
23. Agnetta, L., et al., *A Photoswitchable Dualsteric Ligand Controlling Receptor Efficacy.* Angew Chem Int Ed Engl, 2017. **56**(25): p. 7282-7287.

24. Messerer, R., et al., *FRET Studies of Quinolone-Based Bitopic Ligands and Their Structural Analogues at the Muscarinic M-1 Receptor.* Acs Chemical Biology, 2017. **12**(3): p. 833-843.
25. Groves, J.T., R. Parthasarathy, and M.B. Forstner, *Fluorescence imaging of membrane dynamics.* Annu Rev Biomed Eng, 2008. **10**: p. 311-38.
26. Combs, C.A., *Fluorescence microscopy: a concise guide to current imaging methods.* Curr Protoc Neurosci, 2010. **Chapter 2**: p. Unit2 1.
27. Singh, A. and K.P. Gopinathan, *Confocal microscopy: A powerful technique for biological research.* Current Science, 1998. **74**(10): p. 841-851.
28. Sheppard, C.J.R., *Axial Resolution of Confocal Fluorescence Microscopy.* Journal of Microscopy-Oxford, 1989. **154**: p. 237-241.
29. Guo, H., et al., *Methods used to study the oligomeric structure of G-protein-coupled receptors.* Bioscience Reports, 2017. **37**.
30. Hein, B., K.I. Willig, and S.W. Hell, *Stimulated emission depletion (STED) nanoscopy of a fluorescent protein-labeled organelle inside a living cell.* Proceedings of the National Academy of Sciences of the United States of America, 2008. **105**(38): p. 14271-14276.
31. Blom, H. and J. Widengren, *Stimulated Emission Depletion Microscopy.* Chemical Reviews, 2017. **117**(11): p. 7377-7427.
32. Blom, H. and H. Brismar, *STED microscopy: increased resolution for medical research?* Journal of Internal Medicine, 2014. **276**(6): p. 560-578.
33. Mueller, V., et al., *FCS in STED Microscopy: Studying the Nanoscale of Lipid Membrane Dynamics.* Fluorescence Fluctuation Spectroscopy (Ffs), Pt B, 2013. **519**: p. 1-38.
34. Honigmann, A., et al., *Scanning STED-FCS reveals spatiotemporal heterogeneity of lipid interaction in the plasma membrane of living cells.* Nature Communications, 2014. **5**.
35. Kilpatrick, L.E. and S.J. Hill, *The use of fluorescence correlation spectroscopy to characterize the molecular mobility of fluorescently labelled G protein-coupled receptors.* Biochemical Society Transactions, 2016. **44**: p. 624-629.
36. Mattheyses, A.L., S.M. Simon, and J.Z. Rappoport, *Imaging with total internal reflection fluorescence microscopy for the cell biologist.* Journal of Cell Science, 2010. **123**(21): p. 3621-3628.
37. Axelrod, D., *Evanescent Excitation and Emission in Fluorescence Microscopy.* Biophysical Journal, 2013. **104**(7): p. 1401-1409.
38. Calebiro, D., et al., *Single-molecule analysis of fluorescently labeled G-protein-coupled receptors reveals complexes with distinct dynamics and organization.* Proc Natl Acad Sci U S A, 2013. **110**(2): p. 743-8.
39. Calebiro, D. and T. Sungkaworn, *Single-Molecule Imaging of GPCR Interactions.* Trends Pharmacol Sci, 2018. **39**(2): p. 109-122.
40. van de Linde, S., et al., *Investigating Cellular Structures at the Nanoscale with Organic Fluorophores.* Chemistry & Biology, 2013. **20**(1): p. 8-18.
41. Scarselli, M., et al., *Revealing G-protein-coupled receptor oligomerization at the single-molecule level through a nanoscopic lens: methods, dynamics and biological function.* Febs Journal, 2016. **283**(7): p. 1197-1217.
42. Ziegler, S., et al., *CD56 Is a Pathogen Recognition Receptor on Human Natural Killer Cells.* Scientific Reports, 2017. **7**.
43. Gasparrini, F., et al., *Nanoscale organization and dynamics of the siglec CD22 cooperate with the cytoskeleton in restraining BCR signalling.* Embo Journal, 2016. **35**(3): p. 258-280.
44. Wehbi, V.L., et al., *Noncanonical GPCR signaling arising from a PTH receptor-arrestin-G beta gamma complex.* Proceedings of the National Academy of Sciences of the United States of America, 2013. **110**(4): p. 1530-1535.
45. Stoddart, L.A., et al., *Probing the pharmacology of G protein-coupled receptors with fluorescent ligands.* Neuropharmacology, 2015. **98**: p. 48-57.
46. Brunstein, M., et al., *Eliminating unwanted far-field excitation in objective-type TIRF. Part I. identifying sources of nonevanescent excitation light.* Biophys J, 2014. **106**(5): p. 1020-32.

47. Lin, J. and A.D. Hoppe, *Uniform Total Internal Reflection Fluorescence Illumination Enables Live Cell Fluorescence Resonance Energy Transfer Microscopy.* Microscopy and Microanalysis, 2013. **19**(2): p. 350-359.
48. Nuber, S., et al., *Comparison of the activation kinetics of the M3-ACh-receptor and a constitutive active mutant receptor in living cells.* Naunyn-Schmiedebergs Archives of Pharmacology, 2011. **383**: p. 18-18.
49. Nuber, S., et al., *beta-Arrestin biosensors reveal a rapid, receptor-dependent activation/deactivation cycle.* Nature, 2016. **531**(7596): p. 661-+.
50. Cao, S.H., et al., *Surface Plasmon-Coupled Emission: What Can Directional Fluorescence Bring to the Analytical Sciences?* Annual Review of Analytical Chemistry, Vol 5, 2012. **5**: p. 317-336.
51. Borejdo, J., et al., *Application of surface plasmon coupled emission to study of muscle.* Biophysical Journal, 2006. **91**(7): p. 2626-2635.
52. Lakowicz, J.R., et al., *Directional surface plasmon-coupled emission: a new method for high sensitivity detection.* Biochemical and Biophysical Research Communications, 2003. **307**(3): p. 435-439.
53. de Torres, J., et al., *Plasmonic Nanoantennas Enable Forbidden Forster Dipole-Dipole Energy Transfer and Enhance the FRET Efficiency.* Nano Lett, 2016. **16**(10): p. 6222-6230.
54. Forster, T., **Zwischenmolekulare Energiewanderung Und Fluoreszenz.* Annalen Der Physik, 1948. **2**(1-2): p. 55-75.
55. Kuzmany, H., *Solid-state spectroscopy: an introduction*. 2009: Springer Science & Business Media.
56. Lakowicz, J., *Introduction to Fluorescence*, in *Principles of Fluorescence Spectroscopy*. 2006, Springer. p. 1-26.
57. Dirac, P.A., *The quantum theory of the emission and absorption of radiation.* Proc. R. Soc. Lond. A, 1927. **114**(767): p. 243-265.
58. Thermofisher, *Spectra-Viewer*. 2018, https://www.thermofisher.com/order/spectra-viewer.
59. Enderlein, J., *Modification of Forster Resonance Energy Transfer Efficiency at Interfaces.* International Journal of Molecular Sciences, 2012. **13**(11): p. 15227-15240.
60. Bajar, B.T., et al., *A Guide to Fluorescent Protein FRET Pairs.* Sensors, 2016. **16**(9).
61. Dale, R.E., J. Eisinger, and W.E. Blumberg, *The Orientational Freedom of Molecular Probes. The Orientation Factor in Intramolecular Energy Transfer.* Biophysical Journal, 1979. **26**(2): p. 161-193.
62. Schreiber, B., et al., *Enhanced Fluorescence Resonance Energy Transfer in G-Protein-Coupled Receptor Probes on Nanocoated Microscopy Coverslips.* ACS Photonics, 2018.
63. van der Meer, B.W., M. van der Meer Daniel, and S. Vogel Steven, *Optimizing the Orientation Factor Kappa‐Squared for More Accurate FRET Measurements*.
64. Axelrod, D., *Total Internal Reflection Fluorescence Microscopy in Cell Biology.* Traffic, 2001. **2**(11): p. 764-774.
65. Wade, L.A., *An evanescent perspective on cells*. 2011, California Institute of Technology.
66. Fang, Y., *Total internal reflection fluorescence quantification of receptor pharmacology.* Biosensors (Basel), 2015. **5**(2): p. 223-40.
67. Nguyen, H.H., et al., *Surface Plasmon Resonance: A Versatile Technique for Biosensor Applications.* Sensors, 2015. **15**(5): p. 10481-10510.
68. Bauch, M., et al., *Plasmon-Enhanced Fluorescence Biosensors: a Review.* Plasmonics, 2014. **9**(4): p. 781-799.
69. Yang, H.H.U., et al., *Optical dielectric function of silver.* Physical Review B, 2015. **91**(23).
70. Paolo, B., H. Jer-Shing, and H. Bert, *Nanoantennas for visible and infrared radiation.* Reports on Progress in Physics, 2012. **75**(2): p. 024402.
71. McPeak, K.M., et al., *Plasmonic Films Can Easily Be Better: Rules and Recipes.* ACS Photonics, 2015. **2**(3): p. 326-333.
72. Golosovsky, M., et al., *Midinfrared surface-plasmon resonance: A novel biophysical tool for studying living cells.* Journal of Applied Physics, 2009. **105**(10).

73. Johansen, K., et al., *Imaging surface plasmon resonance sensor based on multiple wavelengths: Sensitivity considerations.* Review of Scientific Instruments, 2000. **71**(9): p. 3530-3538.
74. Balili, R.B., *TRANSFER MATRIX METHOD IN NANOPHOTONICS.* International Journal of Modern Physics: Conference Series, 2012. **17**: p. 159-168.
75. Davis, T.J., *Surface plasmon modes in multi-layer thin-films.* Optics Communications, 2009. **282**(1): p. 135-140.
76. Mariani, S. and M. Minunni, *Surface plasmon resonance applications in clinical analysis.* Analytical and Bioanalytical Chemistry, 2014. **406**(9-10): p. 2303-2323.
77. Peterson, A.W., et al., *High Resolution Surface Plasmon Resonance Imaging of Focal Adhesions in Single Cells.* Biophysical Journal, 2014. **106**(2): p. 24a-25a.
78. Lecaruyer, P., M. Canva, and J. Rolland, *Metallic film optimization in a surface plasmon resonance biosensor by the extended Rouard method.* Applied Optics, 2007. **46**(12): p. 2361-2369.
79. Enderlein, J., I. Gregor, and T. Ruckstuhl, *Imaging properties of supercritical angle fluorescence optics.* Optics Express, 2011. **19**(9): p. 8011-8018.
80. Enderlein, J. and T. Ruckstuhl, *The efficiency of surface-plasmon coupled emission for sensitive fluorescence detection.* Optics Express, 2005. **13**(22): p. 8855-8865.
81. Ray, K., et al., *Distance dependence of surface plasmon-coupled emission observed using Langmuir-Blodgett films.* Applied Physics Letters, 2007. **90**(25): p. 251116.
82. Drexhage, K.H., H. Kuhn, and F.P. Schäfer, *Variation of the Fluorescence Decay Time of a Molecule in Front of a Mirror.* Berichte der Bunsengesellschaft für physikalische Chemie, 1968. **72**(2): p. 329-329.
83. Chance, R.R., et al., *Fluorescence and Energy-Transfer near Interfaces - Complete and Quantitative Description of Eu+3-Mirror Systems.* Journal of Chemical Physics, 1975. **63**(4): p. 1589-1595.
84. Chance, R.R., A. Prock, and R. Silbey, *Decay of an Emitting Dipole between 2 Parallel Mirrors.* Journal of Chemical Physics, 1975. **62**(3): p. 771-772.
85. Chizhik, A.I., et al., *Metal-Induced Energy Transfer for Live Cell Nanoscopy.* Nature Photonics, 2014. **8**(2): p. 124-127.
86. Berndt, M., et al., *Axial Nanometer Distances Measured by Fluorescence Lifetime Imaging Microscopy.* Nano Letters, 2010. **10**(4): p. 1497-1500.
87. Cade, N.I., et al., *A Cellular Screening Assay Using Analysis of Metal-Modified Fluorescence Lifetime.* Biophysical Journal, 2010. **98**(11): p. 2752-2757.
88. Elsayad, K., et al., *Spectrally Coded Optical Nanosectioning (SpecON) with Biocompatible Metal-Dielectric-Coated Substrates.* Proceedings of the National Academy of Sciences of the United States of America, 2013. **110**(50): p. 20069-20074.
89. Bourg, N., et al., *Direct optical nanoscopy with axially localized detection.* Nature Photonics, 2015. **9**(9): p. 587-+.
90. Ma, Y.Q., et al., *Measuring membrane association and protein diffusion within membranes with super critical angle fluorescence microscopy.* Biomedical Optics Express, 2016. **7**(4): p. 1561-1576.
91. Gryczynski, I., et al., *Radiative decay engineering 4. Experimental studies of surface plasmon-coupled directional emission.* Analytical Biochemistry, 2004. **324**(2): p. 170-182.
92. Lakowicz, J.R., *Radiative decay engineering 3. Surface plasmon-coupled directional emission.* Analytical Biochemistry, 2004. **324**(2): p. 153-169.
93. Huang, B., F. Yu, and R.N. Zare, *Surface plasmon resonance imaging using a high numerical aperture microscope objective.* Analytical Chemistry, 2007. **79**(7): p. 2979-2983.
94. Deschamps, J., M. Mund, and J. Ries, *3D superresolution microscopy by supercritical angle detection.* Optics Express, 2014. **22**(23): p. 29081-29091.
95. Sivankutty, S., et al., *Confocal supercritical angle microscopy for cell membrane imaging.* Optics Letters, 2014. **39**(3): p. 555-558.

96. Chance, R.R., A. Prock, and R. Silbey, *Lifetime of an Emitting Molecule near a Partially Reflecting Surface.* Journal of Chemical Physics, 1974. **60**(7): p. 2744-2748.
97. Chance, R.R., A. Prock, and R. Silbey, *Molecular Fluorescence and Energy Transfer Near Interfaces*.
98. Chizhik, A.I., et al., *Nanocavity-Based Determination of Absolute Values of Photoluminescence Quantum Yields.* Chemphyschem, 2013. **14**(3): p. 505-513.
99. Pustovit, V.N. and T.V. Shahbazyan, *Resonance energy transfer near metal nanostructures mediated by surface plasmons.* Physical Review B, 2011. **83**(8).
100. Isbaner, S., et al., *Axial Colocalization of Single Molecules with Nanometer Accuracy Using Metal-Induced Energy Transfer.* Nano Letters, 2018. **18**(4): p. 2616-2622.
101. Karedla, N., et al., *Single-Molecule Metal-Induced Energy Transfer (smMIET): Resolving Nanometer Distances at the Single-Molecule Level.* Chemphyschem, 2014. **15**(4): p. 705-711.
102. Chizhik, A.I., I. Gregor, and J. Enderlein, *Quantum Yield Measurement in a Multicolor Chromophore Solution Using a Nanocavity.* Nano Letters, 2013. **13**(3): p. 1348-1351.
103. Fang, L.P., et al., *Photon tunneling into a single-mode planar silicon waveguide.* Optics Express, 2015. **23**(24): p. 1528-1532.
104. Bharadwaj, P. and L. Novotny, *Spectral dependence of single molecule fluorescence enhancement.* Optics Express, 2007. **15**(21): p. 14266-14274.
105. Chizhik, A.M., et al., *Three-Dimensional Reconstruction of Nuclear Envelope Architecture Using Dual-Color Metal-Induced Energy Transfer Imaging.* Acs Nano, 2017. **11**(12): p. 11839-11846.
106. Shtengel, G., et al., *Interferometric Fluorescent Super-Resolution Microscopy Resolves 3D Cellular Ultrastructure.* Proceedings of the National Academy of Sciences of the United States of America, 2009. **106**(9): p. 3125-3130.
107. Chizhik, A.M., et al., *Dual-Color Metal-Induced and Forster Resonance Energy Transfer for Cell Nanoscopy.* Molecular Biology of the Cell, 2017. **28**.
108. Baronsky, T., et al., *Cell-Substrate Dynamics of the Epithelial-to-Mesenchymal Transition.* Nano Letters, 2017. **17**(5): p. 3320-3326.
109. Oskooi, A.F., et al., *MEEP: A flexible free-software package for electromagnetic simulations by the FDTD method.* Computer Physics Communications, 2010. **181**(3): p. 687-702.
110. Taflove, A. and S.C. Hagness, *Computational electrodynamics: the finite-difference time-domain method*. 2005: Artech house.
111. Draine, B.T. and P.J. Flatau, *Discrete-Dipole Approximation for Scattering Calculations.* Journal of the Optical Society of America a-Optics Image Science and Vision, 1994. **11**(4): p. 1491-1499.
112. Yurkin, M.A. and A.G. Hoekstra, *The discrete-dipole-approximation code ADDA: Capabilities and known limitations.* Journal of Quantitative Spectroscopy & Radiative Transfer, 2011. **112**(13): p. 2234-2247.
113. Chance, R., A. Prock, and R. Silbey, *Lifetime of an Emitting Molecule near a Partially Reflecting Mirror.* Abstracts of Papers of the American Chemical Society, 1974: p. 165-165.
114. Ohring, M., *Materials science of thin films*. 2001: Elsevier.
115. Mattox, D.M., *Handbook of physical vapor deposition (PVD) processing*. 2010: William Andrew.
116. Davidse, P. and L. Maissel, *RF sputtering of insulators*, in *Sessions 9–13*. 1967, Elsevier. p. 651-655.
117. Fujiwara, H., *Spectroscopic ellipsometry: principles and applications*. 2007: John Wiley & Sons.
118. Oates, T., H. Wormeester, and H. Arwin, *Characterization of plasmonic effects in thin films and metamaterials using spectroscopic ellipsometry.* Progress in Surface Science, 2011. **86**(11-12): p. 328-376.
119. Binnig, G., C.F. Quate, and C. Gerber, *Atomic Force Microscope.* Physical Review Letters, 1986. **56**(9): p. 930-933.

120. Meyer, G. and N.M. Amer, *Novel Optical Approach to Atomic Force Microscopy.* Applied Physics Letters, 1988. **53**(12): p. 1045-1047.
121. Zhong, Q., et al., *Fractured Polymer Silica Fiber Surface Studied by Tapping Mode Atomic-Force Microscopy.* Surface Science, 1993. **290**(1-2): p. L688-L692.
122. Sauerbrey, G., *Verwendung Von Schwingquarzen Zur Wagung Dunner Schichten Und Zur Mikrowagung.* Zeitschrift Fur Physik, 1959. **155**(2): p. 206-222.
123. Mayer, M., *Improved physics in SIMNRA 7.* Nuclear Instruments & Methods in Physics Research Section B-Beam Interactions with Materials and Atoms, 2014. **332**: p. 176-180.
124. Necas, D. and P. Klapetek, *Gwyddion: an open-source software for SPM data analysis.* Central European Journal of Physics, 2012. **10**(1): p. 181-188.
125. Schreiber, B., K. Elsayad, and K.G. Heinze, *Axicon-Based Bessel Beams for Flat-Field Illumination in Total Internal Reflection Fluorescence Microscopy.* Optics Letters, 2017. **42**(19): p. 3880-3883.
126. Ellefsen, K.L., J.L. Dynes, and I. Parker, *Spinning-Spot Shadowless TIRF Microscopy.* PLoS One, 2015. **10**(8): p. e0136055.
127. Fiolka, R., et al., *Even illumination in total internal reflection fluorescence microscopy using laser light.* Microsc Res Tech, 2008. **71**(1): p. 45-50.
128. Dos Santos, M.C., et al., *Topography of Cells Revealed by Variable-Angle Total Internal Reflection Fluorescence Microscopy.* Biophysical Journal, 2016. **111**(6): p. 1316-1327.
129. Wagner, M., et al., *Nanotopology of Cell Adhesion upon Variable-Angle Total Internal Reflection Fluorescence Microscopy (VA-TIRFM).* Jove-Journal of Visualized Experiments, 2012(68).
130. Wan, Y.L., et al., *Variable-angle total internal reflection fluorescence microscopy of intact cells of Arabidopsis thaliana.* Plant Methods, 2011. **7**.
131. Fish, K.N., *Total internal reflection fluorescence (TIRF) microscopy.* Curr Protoc Cytom, 2009. **Chapter 12**: p. Unit12 18.
132. Inc, T.F.S. *CellMask™ Plasma Membrane Stains*. 2014; Available from: http://www.thermofisher.com/order/catalog/product/C10046.
133. Schreiber, B., et al., *'Forbidden' States Boost Fluorescence Resonance Energy Transfer (FRET) Studies of Membrane Receptors in Live Cells.* Biophysical Journal, 2018. **114**(3): p. 165a-165a.
134. Axelrod, D., *Total Internal Reflection Fluorescence Microscopy.* Biophysical Tools for Biologists, Vol 2: In Vivo Techniques, 2008. **89**: p. 169-221.
135. Lei, M. and A. Zumbusch, *Total-internal-reflection fluorescence microscopy with W-shaped axicon mirrors.* Optics Letters, 2010. **35**(23): p. 4057-4059.
136. van't Hoff, M., V. de Sars, and M. Oheim, *A programmable light engine for quantitative single molecule TIRF and HILO imaging.* Optics Express, 2008. **16**(22): p. 18495-18504.
137. Ellefsen, K.L., J.L. Dynes, and I. Parker, *Spinning-Spot Shadowless TIRF Microscopy.* Plos One, 2015. **10**(8).
138. Mattheyses, A.L., K. Shaw, and D. Axelrod, *Effective elimination of laser interference fringing in fluorescence microscopy by spinning azimuthal incidence angle.* Microscopy Research and Technique, 2006. **69**(8): p. 642-647.
139. Fiolka, R., et al., *Even illumination in total internal reflection fluorescence microscopy using laser light.* Microscopy Research and Technique, 2008. **71**(1): p. 45-50.
140. Deschamps, J., A. Rowald, and J. Ries, *Efficient homogeneous illumination and optical sectioning for quantitative single-molecule localization microscopy.* Opt Express, 2016. **24**(24): p. 28080-28090.
141. Douglass, K.M., et al., *Super-resolution imaging of multiple cells by optimized flat-field epi-illumination.* Nature Photonics, 2016. **10**(11): p. 705-+.
142. Durnin, J., J.J. Miceli, and J.H. Eberly, *Diffraction-Free Beams.* Journal of the Optical Society of America a-Optics Image Science and Vision, 1986. **3**(13): p. P128-P128.
143. Gao, L., et al., *3D live fluorescence imaging of cellular dynamics using Bessel beam plane illumination microscopy.* Nat. Protocols, 2014. **9**(5): p. 1083-1101.

144. Chen, B.C., et al., *Lattice light-sheet microscopy: imaging molecules to embryos at high spatiotemporal resolution.* Science, 2014. **346**(6208): p. 1257998.
145. Vettenburg, T., et al., *Light-sheet microscopy using an Airy beam.* Nat Methods, 2014. **11**(5): p. 541-4.
146. Axelrod, D., *Evanescent excitation and emission in fluorescence microscopy.* Biophys J, 2013. **104**(7): p. 1401-9.
147. Leutenegger, M., et al., *Fluorescence correlation spectroscopy with a total internal reflection fluorescence STED microscope (TIRF-STED-FCS).* Opt Express, 2012. **20**(5): p. 5243-63.
148. Dickey, F.M. and J.D. Conner. *Annular ring zoom system using two positive axicons*. 2011.
149. Fish, K.N., *Total Internal Reflection Fluorescence (TIRF) Microscopy*, in *Current Protocols in Cytometry*. 2009, John Wiley & Sons, Inc.
150. Beuthan, J., et al., *The spatial variation of the refractive index in biological cells.* Phys Med Biol, 1996. **41**(3): p. 369-82.
151. Chung, E., et al., *Two-dimensional standing wave total internal reflection fluorescence microscopy: Superresolution imaging of single molecular and biological specimens.* Biophysical Journal, 2007. **93**(5): p. 1747-1757.
152. Waters, J.C., *Accuracy and precision in quantitative fluorescence microscopy.* Journal of Cell Biology, 2009. **185**(7): p. 1135-1148.
153. Enderlein, J., I. Gregor, and T. Ruckstuhl, *Imaging properties of supercritical angle fluorescence optics.* Opt Express, 2011. **19**(9): p. 8011-8.
154. Gryczynski, I., et al., *Surface Plasmon-Coupled Emission with Gold Films.* The Journal of Physical Chemistry B, 2004. **108**(33): p. 12568-12574.
155. Yokota, H., K. Saito, and T. Yanagida, *Single Molecule Imaging of Fluorescently Labeled Proteins on Metal by Surface Plasmons in Aqueous Solution.* Physical Review Letters, 1998. **80**(20): p. 4606-4609.
156. He, R.Y., et al., *Enhanced Live Cell Membrane Imaging Using Surface Plasmon-Enhanced Total Internal Reflection Fluorescence Microscopy.* Optics Express, 2006. **14**(20): p. 9307-9316.
157. He, R.Y., et al., *Imaging Live Cell Membranes via Surface Plasmon-Enhanced Fluorescence and Phase Microscopy.* Optics Express, 2010. **18**(4): p. 3649-3659.
158. Mettikolla, P., et al., *Kinetics of a single cross-bridge in familial hypertrophic cardiomyopathy heart muscle measured by reverse Kretschmann fluorescence.* J Biomed Opt, 2010. **15**(1): p. 017011.
159. Anger, P., P. Bharadwaj, and L. Novotny, *Enhancement and quenching of single-molecule fluorescence.* Phys Rev Lett, 2006. **96**(11): p. 113002.
160. Peterson, A.W., et al., *High resolution surface plasmon resonance imaging for single cells.* Bmc Cell Biology, 2014. **15**.
161. Cao, S.-H., et al., *Surface Plasmon–Coupled Emission: What Can Directional Fluorescence Bring to the Analytical Sciences?* Annual Review of Analytical Chemistry, 2012. **5**(1): p. 317-336.
162. Johnson, P.B. and R.W. Christy, *Optical constants of transition metals: Ti, V, Cr, Mn, Fe, Co, Ni, and Pd.* Physical Review B, 1974. **9**(12): p. 5056-5070.
163. Chowdhury, M.H., et al., *Systematic computational study of the effect of silver nanoparticle dimers on the coupled emission from nearby fluorophores.* Journal of Physical Chemistry C, 2008. **112**(30): p. 11236-11249.
164. Bharadwaj, P. and L. Novotny, *Spectral dependence of single molecule fluorescence enhancement.* Opt Express, 2007. **15**(21): p. 14266-74.
165. Allan, D., Caswell, T., Keim, N., van der Wel, C. , *trackpy: Trackpy v0.3.2*. 2016.
166. Ghenuche, P., et al., *Nanophotonic Enhancement of the Forster Resonance Energy-Transfer Rate with Single Nanoapertures.* Nano Letters, 2014. **14**(8): p. 4707-4714.
167. Balaa, K., et al. *Live Cell Imaging with Surface Plasmon-Mediated Fluorescence Microscopy*. in *Advanced Microscopy Techniques*. 2009. Munich: Optical Society of America.
168. Tang, W.T., et al., *Investigation of the point spread function of surface plasmon-coupled emission microscopy.* Optics Express, 2007. **15**(8): p. 4634-4646.

169. Ge, B.L., et al., *Resolution-enhanced surface plasmon-coupled emission microscopy.* Optics Express, 2015. **23**(10): p. 13159-13171.
170. Chen, Y.K., et al., *Surface-plasmon-coupled emission microscopy with a polarization converter.* Optics Letters, 2013. **38**(5): p. 736-738.
171. He, R.Y., et al., *Surface plasmon-enhanced two-photon fluorescence microscopy for live cell membrane imaging.* Optics Express, 2009. **17**(8): p. 5987-5997.
172. Brunstein, M., K. Hérault, and M. Oheim, *Eliminating Unwanted Far-Field Excitation in Objective-Type TIRF. Part II. Combined Evanescent-Wave Excitation and Supercritical-Angle Fluorescence Detection Improves Optical Sectioning.* Biophysical Journal, 2014. **106**(5): p. 1044-1056.
173. Wang, R., et al., *Diffraction-Free Bloch Surface Waves.* ACS Nano, 2017. **11**(6): p. 5383-5390.
174. Rask-Andersen, M., S. Masuram, and H.B. Schioth, *The Druggable Genome: Evaluation of Drug Targets in Clinical Trials Suggests Major Shifts in Molecular Class and Indication.* Annual Review of Pharmacology and Toxicology, Vol 54, 2014. **54**: p. 9-26.
175. Rasmussen, S.G.F., et al., *Crystal Structure of the Beta(2) Adrenergic Receptor-Gs Protein Complex.* Nature, 2011. **477**(7366): p. 549-U311.
176. Kruse, A.C., et al., *Activation and Allosteric Modulation of a Muscarinic Acetylcholine Receptor.* Nature, 2013. **504**(7478): p. 101-6.
177. Latorraca, N.R., A.J. Venkatakrishnan, and R.O. Dror, *GPCR Dynamics: Structures in Motion.* Chemical Reviews, 2017. **117**(1): p. 139-155.
178. Stumpf, A.D. and C. Hoffmann, *Optical Probes Based on G Protein-Coupled Receptors - Added Work or Added Value?* Br J Pharmacol, 2016. **173**(2): p. 255-66.
179. Hoffmann, C., et al., *Comparison of the Activation Kinetics of the M3 Acetylcholine Receptor and a Constitutively active mutant receptor in living cells.* Mol Pharmacol, 2012. **82**(2): p. 236-45.
180. Vilardaga, J.P., et al., *Measurement of the Millisecond Activation Switch of G Protein-Coupled Receptors in Living Cells.* Nature Biotechnology, 2003. **21**(7): p. 807-812.
181. Vilardaga, J.P., et al., *Molecular Basis of Inverse Agonism in a G Protein-Coupled Receptor.* Nature Chemical Biology, 2005. **1**(1): p. 25-28.
182. Vilardaga, J.P., et al., *Conformational Cross-Talk Between Alpha(2A)-Adrenergic and Mu-Opioid Receptors Controls Cell Signaling.* Faseb Journal, 2008. **22**.
183. Hlavackova, V., et al., *Sequential Inter- and Intrasubunit Rearrangements During Activation of Dimeric Metabotropic Glutamate Receptor 1.* Science Signaling, 2012. **5**(237).
184. Olejko, L. and I. Bald, *FRET Efficiency and Antenna Effect in Multi-Color DNA Origami-Based Light Harvesting Systems.* Rsc Advances, 2017. **7**(39): p. 23924-23934.
185. Krainer, G., A. Hartmann, and M. Schlierf, *farFRET: Extending the Range in Single-Molecule FRET Experiments beyond 10 nm.* Nano Letters, 2015. **15**(9): p. 5826-5829.
186. Nicoli, F., et al., *Directional Photonic Wire Mediated by Homo-Förster Resonance Energy Transfer on a DNA Origami Platform.* ACS Nano, 2017.
187. Aissaoui, N., et al., *FRET Enhancement Close to Gold Nanoparticles Positioned in DNA Origami Constructs.* Nanoscale, 2017. **9**(2): p. 673-683.
188. Hsu, L.Y., W.D. Ding, and G.C. Schatz, *Plasmon-Coupled Resonance Energy Transfer.* Journal of Physical Chemistry Letters, 2017. **8**(10): p. 2357-2367.
189. Bidault, S., et al., *Competition between Forster Resonance Energy Transfer and Donor Photodynamics in Plasmonic Dimer Nanoantennas.* Acs Photonics, 2016. **3**(5): p. 895-903.
190. Schleifenbaum, J., et al., *Stretch-Activation of Angiotensin II Type 1(a) Receptors Contributes to the Myogenic Response of Mouse Mesenteric and Renal Arteries.* Circulation Research, 2014. **115**(2): p. 263-+.
191. Konrad, A., et al., *Controlling the Dynamics of Forster Resonance Energy Transfer inside a Tunable Sub-Wavelength Fabry-Perot-Resonator.* Nanoscale, 2015. **7**(22): p. 10204-10209.
192. de Torres, J., et al., *FRET Enhancement in Aluminum Zero-Mode Waveguides.* Chemphyschem, 2015. **16**(4): p. 782-788.

193. Ghenuche, P., et al., *Matching Nanoantenna Field Confinement to FRET Distances Enhances Forster Energy Transfer Rates.* Nano Letters, 2015. **15**(9): p. 6193-6201.
194. Enderlein, J., *Modification of Förster Resonance Energy Transfer Efficiency at Interfaces.* International Journal of Molecular Sciences, 2012. **13**(11): p. 15227-15240.
195. Tumkur, T.U., et al., *Control of Forster Energy Transfer in the Vicinity of Metallic Surfaces and Hyperbolic Metamaterials.* Faraday Discussions, 2015. **178**(0): p. 395-412.
196. Wubs, M. and W.L. Vos, *Forster Resonance Energy Transfer Rate in Any Dielectric Nanophotonic Medium with Weak Dispersion.* New Journal of Physics, 2016. **18**.
197. Blum, C., et al., *Nanophotonic Control of the Forster Resonance Energy Transfer Efficiency.* Physical Review Letters, 2012. **109**(20).
198. de Torres, J., et al., *Plasmonic Nanoantennas Enable Forbidden Forster Dipole-Dipole Energy Transfer and Enhance the FRET Efficiency.* Nano Letters, 2016. **16**(10): p. 6222-6230.
199. Schrage, R., et al., *Agonists with Supraphysiological Efficacy at the Muscarinic M2 ACh Receptor.* British Journal of Pharmacology, 2013. **169**(2): p. 357-370.
200. Bourg, N., et al., *Direct Optical Nanoscopy with Axially Localized Detection.* Nature Photonics, 2015. **9**(11): p. 769-769.
201. Ganesan, S., et al., *A Dark Yellow Fluorescent Protein (YFP)-Based Resonance Energy-Accepting Chromoprotein (REACh) for Forster Resonance Energy Transfer with GFP.* Proceedings of the National Academy of Sciences of the United States of America, 2006. **103**(11): p. 4089-4094.
202. Griffin, B.A., S.R. Adams, and R.Y. Tsien, *Specific Covalent Labeling of Recombinant Protein Molecules inside Live Cells.* Science, 1998. **281**(5374): p. 269-272.
203. Thal, D.M., et al., *Crystal Structures of the M1 And M4 Muscarinic Acetylcholine Receptors.* Nature, 2016. **531**(7594): p. 335-40.
204. Lakowicz, J.R., et al., *Radiative Decay Engineering 2. Effects of Silver Island Films on Fluorescence Intensity, Lifetimes, and Resonance Energy Transfer.* Analytical Biochemistry, 2002. **301**(2): p. 261-277.
205. Aslan, K., et al., *Annealed Silver-Island Films for Applications in Metal-Enhanced Fluorescence: Interpretation in Terms of Radiating Plasmons.* Journal of Fluorescence, 2005. **15**(5): p. 643-654.
206. Khlebtsov, N.G., *Anisotropic Properties of Plasmonic Nanoparticles: Depolarized Light Scattering, Dichroism, and Birefringence.* Journal of Nanophotonics, 2010. **4**.
207. Camelio, S., et al., *Anisotropic Optical Properties of Silver Nanoparticle Arrays on Rippled Dielectric Surfaces Produced by Low-Energy Ion Erosion.* Physical Review B, 2009. **80**(15).
208. Gkogkou, D., et al., *Polarization- and Wavelength-Dependent Surface-Enhanced Raman Spectroscopy Using Optically Anisotropic Rippled Substrates for Sensing.* Acs Sensors, 2016. **1**(3): p. 318-323.
209. Jia, Q., et al., *Ultra-Dense Planar Metallic Nanowire Arrays with Extremely Large Anisotropic Optical and Magnetic Properties.* Nano Research, 2017.
210. Jost, C.A., et al., *Contribution of Fluorophores to Protein Kinase C FRET Probe Performance.* Chembiochem, 2008. **9**(9): p. 1379-84.
211. Johnson, P.B. and R.W. Christy, *Optical Constants of the Noble Metals.* Physical Review B, 1972. **6**(12): p. 4370-4379.
212. Zong, W., et al., *Shadowless-illuminated variable-angle TIRF (siva-TIRF) microscopy for the observation of spatial-temporal dynamics in live cells.* Biomed Opt Express, 2014. **5**(5): p. 1530-40.
213. Boulanger, J., et al., *Fast high-resolution 3D total internal reflection fluorescence microscopy by incidence angle scanning and azimuthal averaging.* Proceedings of the National Academy of Sciences of the United States of America, 2014. **111**(48): p. 17164-17169.
214. Deschamps, J., A. Rowald, and J. Ries, *Efficient homogeneous illumination and optical sectioning for quantitative single-molecule localization microscopy.* Optics Express, 2016. **24**(24): p. 28080-28090.

215. Rowlands, C.J., et al., *Flat-Field Super-Resolution Localization Microscopy with a Low-Cost Refractive Beam-Shaping Element.* Scientific Reports, 2018. **8**.
216. Whelan, D.R., et al., *Focus on Super-Resolution Imaging with Direct Stochastic Optical Reconstruction Microscopy (dSTORM).* Australian Journal of Chemistry, 2014. **67**(2): p. 179-183.
217. Klein, T., et al., *Live-cell dSTORM with SNAP-tag fusion proteins.* Nature Methods, 2011. **8**(1): p. 7-9.
218. Loschberger, A., et al., *The Nuclear Pore Complex as seen by Dstorm.* Biophysical Journal, 2012. **102**(3): p. 723a-723a.
219. Leutenegger, M., et al., *Fluorescence correlation spectroscopy with a total internal reflection fluorescence STED microscope (TIRF-STED-FCS).* Optics Express, 2012. **20**(5): p. 5243-5263.
220. Ivanov, D., et al., *High volume confinement in two-photon total-internal-reflection fluorescence correlation spectroscopy.* Applied Physics Letters, 2009. **94**(8).
221. Guyomard, A., G. Muller, and K. Glinel, *Buildup of multilayers based on amphiphilic polyelectrolytes.* Macromolecules, 2005. **38**(13): p. 5737-5742.
222. Schleifenbaum, F., et al., *Dynamic Control of Forster Energy Transfer in a Photonic Environment.* Physical Chemistry Chemical Physics, 2014. **16**(25): p. 12812-12817.
223. Schaaf, T.M., et al., *Spectral Unmixing Plate Reader: High-Throughput, High-Precision FRET Assays in Living Cells.* Slas Discovery, 2017. **22**(3): p. 250-261.
224. Levene, M.J., et al., *Zero-mode waveguides for single-molecule analysis at high concentrations.* Science, 2003. **299**(5607): p. 682-686.
225. Ardui, S., et al., *Single molecule real-time (SMRT) sequencing comes of age: applications and utilities for medical diagnostics.* Nucleic Acids Research, 2018. **46**(5): p. 2159-2168.
226. Regmi, R., et al., *Planar Optical Nanoantennas Resolve Cholesterol-Dependent Nanoscale Heterogeneities in the Plasma Membrane of Living Cells.* Nano Letters, 2017. **17**(10): p. 6295-6302.
227. Winkler, P.M., et al., *Transient Nanoscopic Phase Separation in Biological Lipid Membranes Resolved by Planar Plasmonic Antennas.* Acs Nano, 2017. **11**(7): p. 7241-7250.
228. Villar, V.M., et al., *Localization and signaling of GPCRs in lipid rafts.* G Protein-Coupled Receptors: Signaling, Trafficking and Regulation, 2016. **132**: p. 3-23.
229. Wada, J., et al., *Fabrication of Zero-Mode Waveguide by Ultraviolet Nanoimprint Lithography Lift-Off Process.* Japanese Journal of Applied Physics, 2011. **50**(6).
230. Liu, L., et al., *A high-performance and low cost SERS substrate of plasmonic nanopillars on plastic film fabricated by nanoimprint lithography with AAO template.* Aip Advances, 2017. **7**(6).
231. Repetto, D., et al., *SERS amplification by ultra-dense plasmonic arrays on self-organized PDMS templates.* Applied Surface Science, 2018. **446**: p. 83-91.
232. Karakouz, T., et al., *Mechanism of morphology transformation during annealing of nanostructured gold films on glass.* Physical Chemistry Chemical Physics, 2013. **15**(13): p. 4656-4665.
233. Schreiber, B., et al., *Large-scale self-organized gold nanostructures with bidirectional plasmon resonances for SERS.* RSC Advances, 2018. **8**(40): p. 22569-22576.
234. Tan, B.J.Y., et al., *Fabrication of size-tunable gold nanoparticles array with nanosphere lithography, reactive ion etching, and thermal annealing.* Journal of Physical Chemistry B, 2005. **109**(22): p. 11100-11109.
235. Hsu, S.W., et al., *Colloidal Plasmonic Nanocomposites: From Fabrication to Optical Function.* Chemical Reviews, 2018. **118**(6): p. 3100-3120.
236. Luan, J., et al., *Add-on plasmonic patch as a universal fluorescence enhancer.* Light: Science & Applications, 2018. **7**(1): p. 29.
237. Diekmann, R., et al., *Chip-based wide field-of-view nanoscopy.* Nature Photonics, 2017. **11**(5): p. 322-+.
238. Heil, H.S., et al., *Boosting The Localization Precision Of dSTORM By Biocompatible Metal-Dielectric Coated Glass Coverslips.* bioRxiv, 2017.

8 Appendix

8.1 Abbreviations

AFM	atomic force microscopy
AOTF	acousto-optical tunable filter
Au	gold
AxiTIRF-M	axicon-based total internal reflection fluorescence microscope
BAL	1,2-dimercapto-1-propanol, British Anti-Lewisite
BFP	back focal plane
BGR	background
BK7	borosilicate crown glass
BP	band pass
BSA	bovine serum albumin
CAD	computer assisted design
CFP	cyan fluorescent protein
CHO cell	Chinese hamster ovary cell
CMOS camera	complementary metal-oxide-semiconductor camera
CPS theory	Change, Prock and Silbey theory
Cr	chromium
DM	dichroic mirror
DMEM	Dulbecco's modified eagle medium
dSTORM	direct stochastic optical reconstruction microscopy
EMCCD camera	electron multiplying charge-coupled device camera
f = … mm	focus length in mm
FCS	fluorescence correlation spectroscopy
FE	field enhancement
FEM	finite element method
FlAsH	fluorescein arsenical hairpin binder
*for*FRET coating	coating what enables forbidden FRET
FOV	field of view
f-Pics coating	flouplasmonic coating
FRET	fluorescence resonance energy transfer
GPCR	G-protein coupled receptor
HEK cell	human embryonic kidney cell
HEPES	4-(2-hydroxyeg´thyl)-1-piperazineethanesulfonic acid
IL	intercellular loop
IP	image plane
laser	light amplification by stimulated emission of radiation
M1 mAChR	muscarinic acetylcholine receptor M1 subtype
MIET	metal induced energy transfer
MIF	metal island film
n	number of experiments
NA	numerical aperture
NLAFN-21	Lanthanum flint glass
P, pol.	polarizer, polarization
PBC	periodic boundary conditions
PBS	phosphate buffered saline
PFA	paraformaldehyde
PSF	point spread function

QCM	quartz crystal microbalance
QY	quantum yield
RBS	Rutherford backscattering spectrometry
RF	radio frequency
RI	refractive index
rms	root mean squared
SAF	supercritical angle fluorescence
SCCM	standard cubic centimeters per minute
SD	standard derivation
SE	spectroscopic ellipsometry
SiN	silicon nitride
SM	scanning mirror
SMLM	single molecule localization microscopy
SNR	signal-to-noise ratio
SPCE	surface plasmon coupled emission
SPR	surface plasmon resonance
STED	stimulated emission depletion
TBC	transition boundary condition
TIR	total internal reflection
TIRF-M	total internal reflection fluorescence microscopy
TM	transversal magnetic
TTL	transistor–transistor logic
UAF	undercritical angle fluorescence
USB	universal Serial Bus
VA	variable angle
VASi	variable angle spinning spot illumination
WF	wide-field

8.2 Acknowledgments

This work presented here was accomplished at the Rudolf Virchow Center for Experimental Biomedicine, University of Würzburg in the Group of Prof. Dr. Katrin G. Heinze between April 2015 and July 2018. Results summarized in this thesis have been published, as indicated in the respective section.

I thank the Elitenetzwerk Bayern for providing the fellowship that allow me to perform my PhD thesis at the University of Würzburg and I am thankful to be a part of the international doctorate program "Receptor Dynamics*:* Emerging Paradigms for Novel Drugs".

I like to thank the Graduate School of Life Science for coordination of the PhD study program and providing and organization of the transferable skill courses.

Prof. Dr. Katrin G. Heinze I like to thank for giving me the opportunity to perform my PhD thesis in her laboratory. I am thankful her for her constant support, encouragement, trust valuable scientific discussions.

I like to thank the whole Heinze group for all the support I received during my PhD time. I thank Mike Friedrich and Jürgen Pinnecker for teaching me fluorescence microscopy and show me the beauty of optical engineering. I like to thank Hannah S. Heil for fruitful discussion of the plasmon projects. I thank Kerstin Jansen, Dr. Julia Wagner, Ashwin Balakrishnan and Dr. Susobhan Choudhury for help with chemistry, assistance with the cell culture and for discussions of the biological parts of my thesis. In addition, I like to thank Oguzhan Angay, Dr. Katherina Hemmen, Thomas Müller, Jan-Hagen Krohn and Jakob Wachter for many discussions and the friendly atmosphere in the group.

I like to thank the clean room facility of the University of Würzburg, especially Dr. Martin Kamp, Prof. Dr. Sven Höfling and Monika Emmerling for initial fabrication of the nanocoated coverslips.

The group of Prof. Dr. Carsten Hoffmann I like to thank for cooperation in the FRET enhancement project, especially I thank Michael Kauk for performing the FRET experiments. I like to thank Prof. Dr. Ulrike Holzgrabe for providing the ligands for the FRET studies.

I like to thank Dr. Kareem Elsayad for the opportunity of a research stay at the Advanced Microscopy facility at the Vienna Biocenter. To discuss with you was very helpful and have made a decisive contribution to the success of my PhD. In addition, I am thankful that you gave me the possibility to build the "AxiTIRF" in your lab. In addition, I thank the whole AdvMicro crew for the beautiful time in your facility. I will definitely visit you again.

Am Ende möchte ich gerne meine Familie danken für andauernde Unterstützung und motivierenden Worte welche mich wären meiner Doktorarbeit begleitet haben.

8.3 Publications

Original articles presented in this thesis:

Schreiber B, Heil HS, Kamp M, Heinze KG; Live-cell fluorescence imaging with extreme background suppression by plasmonic nanocoatings, *Optics Express*, 2018: Accepted

Schreiber B[#], **Kauk M**[#], Heil HS, Emmerling M, Kamp M, Höfling S, Holgrabe U, Hoffmann C, Heinze KG; Enhanced fluorescence resonance energy transfer in G protein-coupled receptors probes by nano-coated microscopy coverslips, *ACS Photonics*, 2018, 5 (6): 2225–2233
[#]B.S. and M. Kauk contributed equally to this work

Schreiber B, Elsayad K, Heinze KG; Axicon-based Bessel beams for flat-field illumination in total internal reflection fluorescence microscopy, *Optics Letters**,**, 2017, 42 (19): 3880-3883;
*****Awarded with Optics Letters "Editors pick" of the Optical Society of America
****** Featured by Advances in Engineering, www.advanceseng.com

Further original articles:

Schreiber B, Gkogkou D, Dedelaite L, Kerbusch J, Hübner R, Sheremet E, Zahn DRT, Ramanavicius A, Facsko S, Rodriguez RD; Large-scale self-organized gold nanostructures with bidirectional plasmon resonances for SERS, *RSC Advances*, 2018, 8: 22569

Jia Q, Ou X, Langer M, **Schreiber B**, Grenzer J, Siles PF, Rodriguez RD, Huang K, Yuan Y, Heidarian A, Hübner R, You T, Yu W, Lenz K, Linder J, Wang X, Facsko S; Ultra-dense planar metallic nanowire arrays with extremely large anisotropic optical and magnetic properties, *Nano Research*, 2017: 1–10

Heil HS, **Schreiber B**, Emmerling M, Höfling S, Kamp M, Sauer M, Heinze KG; Boosting the localization precision of dSTORM by biocompatible metal-dielectric coated glass coverslips, *bioRxiv*, 2017

Gkogkou D, **Schreiber B**, Shaykhutdinov T, Ly HK, Kuhlmann U, Gernert U, Facsko S, Hildebrandt P, Esser N, Hinrichs K, Weidinger IM, Oates TWH; Polarization- and Wavelength-Dependent Surface-Enhanced Raman Spectroscopy Using Optically Anisotropic Rippled Substrates for Sensing, *ACS Sensors*, 2016, 1: 818-323

Gkogkou D, Shaykhutdinov T, Oates TWH, Gernert U, S**chreiber B**, Facsko S, Hildebrandt P, Weidinger IM, Esser N, Hinrichs K; Characterization of anisotropically shaped silver nanoparticle arrays via spectroscopic ellipsometry supported by numerical optical modeling, *Applied Surface Science*, 2017, 421(B): 460-464

Oertel J, Keller A, Prinz J, **Schreiber B**, Hübner R, Kerbusch J, Bald I, Fahmy K; Anisotropic metal growth on phospholipid nanodiscs via lipid bilayer expansion, *Scientific Reports*, 2016, 6:26718

Prinz J, **Schreiber B**, Olejko L, Oertel J, Rackwitz J, Keller A, Bald I; DNA Origami Substrates for Highly Sensitive Surface-Enhanced Raman Scattering, *The Journal of Physical Chemistry Letters*, 2013, 4(23):4140-4145

Participation at international conferences

Oral presentations:

23 - 24 Mar 2017; International Symposium in Montpellier organized by the international Doctoral Program “Receptor Dynamics – Emerging Paradigms for Novel Drugs” Elite Network of Bavaria, Montpellier, France; Oral Presentation: “Tweaking TIRFM for Enhanced Membrane Imaging”

11 – 16 Mar 2018; 82th Annual Meeting of the Deutsche Physikalische Gesellschaft (DPG 2018), Berlin, Germany; Oral Presentation: “Enhanced fluorescence resonance energy transfer in G protein-coupled receptor probes by nano-coated microscopy coverslips”

Poster presentations:

13 - 16 Sep 2015; 14th International Conference Methods and Applications in Fluorescence (MAF 14), Würzburg, Germany; Poster: “Optoplasmonic approaches to enhanced Fluorescence Resonance Energy Transfer (FRET) near Surfaces”

14 - 15 Oct 2015; 10th International Symposium organized by the Doctoral Researchers of the Graduate School of Life Sciences “Eureka!”, Würzburg, Germany; Poster: “Optoplasmonic approaches to enhanced Fluorescence Resonance Energy Transfer (FRET) near Surfaces”

11 - 16 Nov 2015; International Symposium organized by the international Doctoral Program “Receptor Dynamics – Emerging Paradigms for Novel Drugs” Elite Network of Bavaria, Rehovot, Israel; Poster: “Enhanced Fluorescence Resonance Energy Transfer (FRET) near metal-dielectric surfaces”

6 – 8 Apr 2016; The International Conference GLISTEN Erlangen 2016, Erlangen, Germany; Poster “Metal-dielectric coated slides for single molecule cell imaging”

26 – 30 Sep 2016; Joint Meeting of the Biophysics Groups of the University of Göttingen and University of Würzburg “Biophysics by the Sea”, Alcudia, Spain; Poster: “Modified Fluorescence Resonance Energy Transfer (FRET) near metal-dielectric surfaces”

9 – 12 Apr 2017; International Conference Focus on Microscopy (FOM 2017), Bordeaux, France; Poster: “Combined Surface Plasmon Resonance Excitation and Emission for High-Speed Live-Cell Imaging”

8.4 Dissertation based on several published manuscripts

8.4.1 Statement of individual author contributions to figures/tables/chapters

Statement of individual author contributions to figures/tables/chapters included in the manuscripts

Publication (complete reference): "Axicon-based Bessel beams for flat-field illumination in total internal reflection fluorescence microscopy", **Benjamin Schreiber**, Kareem Elsayad, Katrin G. Heinze, Optics Letters 42, 2017					
Figure	**Author Initials,** Responsibility decreasing from left to right				
1	BS	KGH	KE		
2	BS	KGH	KE		
3	BS	KGH	KE		
4	BS	KGH	KE		
5					

Explanations (if applicable):

Publication (complete reference): „Enhanced Fluorescence Resonance Energy Transfer in G-Protein-Coupled Receptor Probes on Nanocoated Microscopy Coverslips", **Benjamin Schreiber#**, Michael Kauk#, Hannah S. Heil, Monika Emmerling, Ingrid Tessmer, Martin Kamp, Sven Höfling, Ulrike Holzgrabe, Carsten Hoffmann, Katrin G. Heinze, ACS Photonics 10.1021/acsphotonics.8b00072, 2018					
Figure	**Author Initials,** Responsibility decreasing from left to right				
1	M Kauk	BS	KGH	CH	
2	M Kauk	BS	KGH	CH	
3	BS	KGH			
4	BS	KGH			
5					

Explanations (if applicable): Shared first authorship (#)

Publication (complete reference): „Low background microscopy by Fluoplasmonics", **Benjamin Schreiber**, Hannah S. Heil, Martin Kamp, Katrin G. Heinze, Optics Letters, in revision					
Figure	**Author Initials,** Responsibility decreasing from left to right				
1	BS	KGH	HSH	M Kamp	
2	BS	KGH	HSH	M Kamp	
3	BS	KGH	HSH	M Kamp	
4	BS	KGH	HSH	M Kamp	
5					

Explanations (if applicable):

I also confirm my primary supervisor's acceptance.

Benjamin Schreiber Würzburg

_____

Doctoral Researcher's Name Date Place Signature

8.4.2 Statement of individual author contributions and legal second publication rights

Statement of individual author contributions and of legal second publication rights

Publication (complete reference): "Axicon-based Bessel beams for flat-field illumination in total internal reflection fluorescence microscopy", **Benjamin Schreiber**, Kareem Elsayad, Katrin G. Heinze, Optics Letters 42, 2017					
Participated in	**Author Initials,** Responsibility decreasing from left to right				
Study Design Methods Development	BS BS	KE KE	KGH KGH		
Data Collection	BS	KE			
Data Analysis and Interpretation	BS	KE	KGH		
Manuscript Writing: Writing of Introduction Writing of Materials & Methods Writing of Discussion Writing of First Draft	 BS BS BS BS	 KGH KGH KGH KGH			

Explanations (if applicable):

Publication (complete reference): „Enhanced Fluorescence Resonance Energy Transfer in G-Protein-Coupled Receptor Probes on Nanocoated Microscopy Coverslips", **Benjamin Schreiber#**, Michael Kauk#, Hannah S. Heil, Monika Emmerling, Ingrid Tessmer, Martin Kamp, Sven Höfling, Ulrike Holzgrabe, Carsten Hoffmann, Katrin G. Heinze, ACS Photonics 10.1021/acsphotonics.8b00072, 2018					
Participated in	**Author Initials,** Responsibility decreasing from left to right				
Study Design Methods Development	BS M Kauk	M Kauk BS	KGH CH	CH KGH	UH
Data Collection	Explanation 1)				
Data Analysis and Interpretation	Explanation 2)				
Manuscript Writing: Writing of Introduction Writing of Materials & Methods Writing of Discussion Writing of First Draft	 BS Explanation 3) BS BS	 M Kauk M Kauk M Kauk	 KGH KGH KGH	 CH CH CH	

Explanations (if applicable): Shared first authorship (#)

Explanation 1) Referring to Data Collection:
Establishment of physical models: BS KGH HSH M Kamp SH IT
FRET experimentation / characterization: M Kauk CH

Explanation 2) Referring to Data Analysis and Interpretation:
Physical data analysis and interpretation: BS KGH HSH
FRET data analysis and interpretation: M Kauk CH BS

Explanation 3) Referring to Writing of Materials & Methods:
Physical material and methods: BS KGH HSH M Kamp SH ME
FRET experiments, material and methods: M Kauk CH UH

Publication (complete reference): „Low background microscopy by Fluoplasmonics“, **Benjamin Schreiber**, Hannah S. Heil, Martin Kamp, Katrin G. Heinze, Optics Letters, in revision					
Participated in	**Author Initials,** Responsibility decreasing from left to right				
Study Design Methods Development	BS BS	KGH MKamp	HSH HSH	 KGH	
Data Collection	BS				
Data Analysis and Interpretation	BS	KGH	HSH		
Manuscript Writing: Writing of Introduction Writing of Materials & Methods Writing of Discussion Writing of First Draft	 BS BS BS BS	 KGH KGH KGH KGH	 HSH		

Explanations (if applicable):

The doctoral researcher confirms that she/he has obtained permission from both the publishers and the co-authors for legal second publication.

The doctoral researcher and the primary supervisor confirm the correctness of the above mentioned assessment.

Benjamin Schreiber Würzburg

_____

Doctoral Researcher’s Name Date Place Signature

Prof. Dr. Katrin G. Heinze Würzburg

_____

Primary Supervisor’s Name Date Place Signature

8.5 Affidavit

Affidavit

I hereby confirm that my thesis entitled “Selective and enhanced fluorescence by biocompatible nanocoatings to monitor G-protein coupled receptor dynamics” is the result of my own work. I did not receive any help or support from commercial consultants. All sources and / or materials applied are listed and specified in the thesis.

Furthermore, I confirm that this thesis has not yet been submitted as a part of another examination process neither in identical nor similar form.

Würzburg, July, 2018 _____

Benjamin Schreiber

8.6 Eidesstattliche Erklärung

Eidesstattliche Erklärung

Hiermit erkläre ich an Eides statt, die Dissertation „Selektive und verstärkte Fluoreszenz durch biokompatible Nanobeschichtungen zur Untersuchung von G-protein gekoppelten Rezeptoren und ihrer Dynamik“ eigenständig, d.h. insbesondere selbständig und ohne Hilfe eines kommerziellen Promotionsberaters, angefertigt und keine anderen als die von mir angegeben Quellen und Hilfsmittel verwendet zu haben.

Ich erkläre außerdem, dass die Dissertation weder in gleicher noch ähnlicher Form bereits in einem anderen Prüfungsverfahren vorgelegen hat.

Würzburg, Juli, 2018 _____

Benjamin Schreiber